MEASUREMENTS AND MODELS OF FINE-STRUCTURE, INTERNAL GRAVITY WAVES AND WAVE BREAKING IN THE DEEP OCEAN

by

CHARLES CURTIS ERIKSEN
A.B., Harvard College
1972

SUBMITTED IN PARTIAL FULFILLMENT
OF THE REQUIREMENTS FOR THE
DEGREE OF DOCTOR OF
PHILOSOPHY

at the

MASSACHUSETTS INSTITUTE OF TECHNOLOGY

and the

WOODS HOLE OCEANOGRAPHIC INSTITUTION
September, 1976
(i.e. February 1977)

Signature of Author _____

Joint Program in Oceanography, Massachusetts Institute of Technology-Woods Hole Oceanographic Institution, and Department of Earth and Planetary Sciences, Massachusetts Institute of Technology, September, 1976.

Certified by _____
Thesis Supervisor

Accepted by _____
Chairman, Joint Oceanography Committee in Earth Sciences, Massachusetts Institute of Technology-Woods Hole Oceanographic Institution.

WITHDRAWN FROM MIT LIBRARIES
MAR 22 1977

MEASUREMENTS AND MODELS OF FINE-STRUCTURE, INTERNAL GRAVITY WAVES AND WAVE BREAKING IN THE DEEP OCEAN

by

Charles Curtis Eriksen

Submitted to the Massachusetts Institute of Technology - Woods Hole Oceanographic Institution Joint Program in Oceanography on September 10, 1976 in partial fulfillment of the requirements for the degree of Doctor of Philosophy.

Abstract

Measurements of horizontal and vertical current by propeller cluster current meters and temperature by thermistors mounted on a rigid array 8 m high and 20 m long moored in the oceanic main thermocline near Bermuda are interpreted in terms of thermocline-trapped internal wave modes in the presence of temperature and density fine-structure.

Two turning-point uniformly valid asymptotic solutions to the internal wave equation are developed to describe the wave functions. Mode decay beyond the turning point in depth or frequency produces a sharp cutoff in vertical current spectra above the local buoyancy frequency $N(z)$. An internal wave wavenumber-frequency spectral model $E(\alpha,\omega) = E(\omega/N_o)^{-2}(\alpha/\alpha_o)^{-2}$ describes vertical current spectra and potential energy to horizontal kinetic energy ratios. The red wavenumber shape suppresses peaks in both these quantities at frequencies near $N(z)$. The data are consistent with time-averaged horizontal isotropy of the wave field. A dip in the vertical current spectra at 0.5 cph not predicted by the model appears related to the bottom slope.

Temperature fine-structure is modeled as a passive vertical field advected by internal waves. Quasi-permanent fine-scale features of the stratification and vertically small-scale internal waves are indistinguishable in this study. The model of McKean (1974) is generalized to include fine-structure fields specified by their vertical wavenumber spectra as well as different Poisson-distributed layer models. Together with the trapped internal wave model, moored temperature spectra, temperature vertical difference spectra, and coherence over vertical separations are described using a fine-structure vertical wavenumber spectrum $P_T(k) = A_T k^{-5/2}$ which agrees with other spectra made using vertical profiling instruments in the range 0.1 to 1.0 cpm.

Horizontal current fine-structure is also modeled as a passive field advected vertically by long internal waves. The model describes moored horizontal current spectra (least successfully at frequencies near $N(z)$) and finite-difference vertical shear spectra.

Contours of temperature in depth versus time indicate possible mixing events. These events appear concurrently with high shear and Richardson numbers $0.25 \lesssim R \lesssim 1.0$. Over 7 m a cutoff in R_i at 0.25 is observed, indicating saturation of the internal wave spectrum. Spectra of finite-difference approximations to shear and buoyancy frequency are dominated by fine-structure contributions over nearly the whole internal wave range, suggesting that breaking is enhanced by fine-structure. Breaking appears equally likely at all frequencies in the internal wave range.

Thesis Supervisor: Carl Wunsch
Title: Professor of Physical Oceanography

Acknowledgements

I wish to express my thanks to Professor Carl Wunsch of M.I.T. for his generous and seemingly limitless guidance and support. His wise combination of advice and consent allowed me to pursue this study with even temper and peaceful mind, thoroughly mixing work and play. I am deeply grateful to him not only for the resources he placed at my disposal and his stimuli to my perception of the specific scientific problem and its solution, but for the awareness and insight I carry away from this research experience as a result of his tutelage.

I thank John Dahlen and his group at the C. S. Draper Laboratory for carrying out the MSA and IIWA field work. I am grateful to Jack Shillingford for his careful, painstaking work in coaxing the MSA to perform. His long stubborn hours of matching wits against an instrument of incredible complexity were vital to my success. I thank him for an extraordinary effort.

I thank Dr. Melbourne Briscoe of W.H.O.I. for careful critical review of this manuscript. His comments encouraged clarity in both my mind and the presentation of my work. I thank Dr. Terrence Joyce of W.H.O.I. for discussions and review of the manuscript. I am grateful to him and to Dr. Nelson Hogg and E. Schroeder (both of W.H.O.I.) for providing unpublished data for use in this study.

Barbara Grant and Charmaine King of M.I.T. provided enormous help in processing the roughly 100 million bits of information the instruments spewed forth. I am grateful to Ms. Grant for her selfless support during my contests with computing machines. She has been a blessing.

I thank Doris Haight for her beautiful, fast, and accurate typing.

This research was supported by Office of Naval Research contract N00014-67-0204-0047 and continuation contract N00014-75-C-0291.

Table of Contents

		Page No.
Abstract		2
Acknowledgements		4
List of Figures		7
Chapter 1.	Introduction	14
Chapter 2.	Field Program	
2.1	Instrumentation	24
2.2	Experiments	30
2.3	Data Handling	36
Chapter 3.	Internal Waves without Fine-Structure	
3.1	An internal wave model	53
3.2	Comparisons with data	64
3.3	Horizontal isotropy of the wave field	78
Chapter 4.	Internal Waves with Fine-Structure	
4.1	Models of temperature fine-structure	85
4.2	Comparisons with temperature data	100
4.3	Horizontal current fine-structure effects	124
Chapter 5.	Wave Breaking	134
Chapter 6.	Conclusions	149
Appendix.	Estimation of Vertical Current from Temperature Measurements	154
References		162
Biographical Note		166

List of Figures

Page No.

Figure 2.1. Schematic drawing of the MSA as it was configured for (a) the first experiment (October 1973) and (b) the second and third experiments (July 1975 and November 1975). 25

Figure 2.2. Charts of Bermuda. (a) Gross topography adapted from Wunsch (1972) showing the location of the Panulirus hydrographic stations and the Wunsch and Dahlen (1970) ("WD") moored experiment. (b) Local topography of the southeast Bermuda slope drawn from Defense Mapping Agency Hydrographic Center Chart N.O. 26341 and a local survey made from R/V Panulirus (shown in Figure). A transect through this survey is shown from which the profile in Figure 3.5 is drawn. Sites of the three MSA experiments are shown with squares; the IIWA experiment and its orientation is shown schematically by a triangle. Crosses represent Brown-W.H.O.I. CTD stations from R/V Knorr Cruise 52 (No. 48, 27 October 1975; Nos. 61-64, 1 November 1975) and R/V Eastward (No. 24, 18 October 1975) 32

Figure 2.3. Field of view of propeller clusters. These figures represent the solid angle of a hemisphere (whose equator is in the y'-z' plane - see Figures 2.4 and 2.5) for which clusters of 4(a), 5(b), and 7(c) propellers reliably resolve a current vector. Concentric circles represent 30°, 60°, and 90° angles with respect to the x'-axis (out of the y'-z' plane). Numbers 1-7 represent orientations of propellers (see also Figure 2.4); note propellers 5-7 are oriented parallel to the y'-z' plane, thus both positive and negative directions appear on the 90° circle. Sparsely horizontally hatched regions represent solid orientations for which one combination of three propellers adequately resolves the flow. Vertically hatched regions represent orientations covered by two combinations and heavily horizontally hatched regions represent orientations covered by three combinations 38

Figure 2.4. Perspective sketch of propeller axis orientations. Flows U_1-U_7 along propeller axes 1-7 make angles θ_1-θ_7 with the current vector $\vec{V}$. These flows are resolved as $U_i = a_{i1}\hat{u} + b_{i2}\hat{v} + c_{i3}\hat{w}$. Counts from combinations of three propellers can be used to compute $\vec{V} = \hat{u} + \hat{v} + \hat{w}$ 40

List of Figures (Contd.)

Page No.

Figure 2.5. Sketch of MSA geometry. Current records at each cluster are resolved into UCOR, VCOR, and W components in the X, Y, and Z directions, a cartesian frame referred to the MSA azimuth and geographical vertical. In normal operation UCOR is negative and VCOR and W are small compared with the magnitude of UCOR. 43

Figure 2.6. Typical current records from forward lower (lower four plots) and forward upper (upper four plots) clusters taken during the second experiment (in two overlapping frames). UCOR, VCOR, W, and QUALITY are plotted versus time (labeled in 1-hour increments) for each cluster. Note UCOR is normally negative (see Figure 2.5) and of larger magnitude than other components. VCOR is noisier than UCOR and W due to correction for heading change with time, but the noise is the same for both forward records. QUALITY is above 95 (upper dashed line in QUALITY plots) except at isolated times. Note that when UCOR approaches zero at about 70.40 hours, QUALITY drops more severely for the forward lower record (a 5-propeller cluster) than for the forward upper record (a 7-propeller cluster) because of the greater "field of view" of the forward upper cluster (see Figure 2.3). 45

Figure 2.7. Spectra of UCOR, VCOR, and W from a 2-day segment of records from the third experiment. At low frequencies UCOR is most energetic and W is least energetic. Averages are over 16 adjacent frequencies; an error estimate for 95% confidence is at the left. The spectra coalesce above about 20 cph and flatten; the variance from about 18 cph to 180 cph corresponds to a standard deviation of roughly 0.2 cm/sec, the estimated measurement noise. All error estimates for spectra in this study were computed following Jenkins and Watts (1969). 48

Figure 3.1. Profiles of N(z) and $N^2(z)$ selected Panulirus stations. Profiles in (a), (c), and (e) correspond to stations closest to the time of the three MSA experiments. The profiles in (b) were taken during the IIWA experiment. Profiles in (d) are typical historical stations for which the temperature at the MSA depth was comparable to that measured during the second experiment (i.e., anomalously warm: approximately 16°C at 630 m). Presence of fine-structure contributes to the roughness

List of Figures (Contd.)

		Page No.
	of the profiles. The maximum in N(z) (i.e., the center of the main thermocline) occurs at about 700-800 m. Heavy horizontal lines are drawn at the depth of the appropriate MSA experiment in each frame. IIWA instrument depths are bracketed in (b).	54
Figure 3.2.	Model and observed ratios P.E./H.K.E. The observed ratio was computed from the forward upper cluster records in a 6-day segment of the second experiment. Averages are over 18 adjacent frequencies; error estimates for 95% confidence are at the right. Model curves use $E(\beta,\omega) = E(\omega/N_o)^{-2}(\beta/\beta_o)^{-p}$ where p = 0,1,2 in (a), (b), (c).	70
Figure 3.3.	Model and observed spectra of vertical current. The observed spectrum was computed from the forward upper cluster record in a 6-day segment of the second experiment. Averages are over 18 adjacent frequencies; error estimates for 95% confidence are at the right. Model curves use $E(\beta,\omega) = 0.25(\omega/N_o)^{-2}(\beta/\beta_o)^{-p}$ cm^2/sec^2/cph where p = 0,1,2 in (a), (b), (c). Note the spectral well of about a factor of two centered at about 0.5 cph, believed to be related to the slope topography	72
Figure 3.4.	Mean-gradient model and observed spectra of (a) horizontal current and (b) temperature. The spectrum of UCOR was computed as in the previous two figures. The temperature spectrum was computed from a 3-day record in the second experiment. Averages are over 18 adjacent frequencies; error estimates for 95% confidence are at the left. Model curves use $E(\beta,\omega) = 0.25\ (\omega/N_o)^{-2}(\beta/\beta_o)^{-2}$ cm/sec/cph. The measured mean temperature gradient ($T_z = 12.35 \times 10^{-3}$ °C/m) was used in calculating the model temperature spectrum.	74
Figure 3.5.	A bathymetric profile of the Bermuda slope near the site of the second experiment (see Figure 2.2). A schematic of the MSA along with approximate characteristics of internal waves at 0.5 cph are also drawn. Note that bottom slopes and characteristic slopes are nearly the same.	76
Figure 3.6.	Polar plots of kD versus $k^{-p}(0<k<1)$ where D = 10° in (a), 5° in (b)	81

List of Figures (Contd.)

Page No.

Figure 3.7. Coherence phase at 1.0 cph between vertical current at the three possible pairs of current meters. The 18-hour records used overlap each adjacent record by 6 hours. Line segments connect computed phases; error estimates for 95% confidence are plotted with similar symbols. Nine adjacent frequencies were averaged in computing phases in this plot. 83

Figure 4.1. Model and observed temperature spectra. The observed temperature spectra shown here and temperature difference spectra and temperature coherences shown in succeeding figures were computed from a 3-day record. Averages are over 18 adjacent frequencies; error estimates for 95% confidence are at the left. Model curves of the mean-gradient contribution (dashed curves), the fine-structure contribution (dot-dashed curves) and the total temperature spectrum (solid curves) are drawn. Spectral slopes are asymptotic values for $\omega << N$ and $\omega >> N$. Sheet-layer or constant-gradient model curves are in (a) and constant-curvature model curves are in (b). A passive wavenumber spectrum of the form $P_T(k) = A_T k^{-5/2}$ is used to produce (c) 104

Figure 4.2. Model and observed temperature difference spectra over a 712.8 cm vertical separation (normalized by separation squared). Model curves of the mean-gradient contribution (dashed curves), the fine-structure contribution (dot-dashed curves) and the total temperature difference spectrum (solid curves) are drawn. The fine-structure contribution exceeds the mean-gradient contribution at all but very low frequencies, so that for most of the internal wave range fine-structure (kinematical) effects dominate temperature difference. A process-specified model(B=0) is used in (a), a wavenumber spectrum-specified model with $P_T(k) = A_T k^{-5/2}$ is used in (b). 106

Figure 4.3. Model and observed temperature difference spectra over a range of different separations. The models and model parameters are the same as in Figure 4.2 . . 108

Figure 4.4. IIWA temperature difference spectra at different separations, normalized by the separation squared. These spectra are computed from 50-day records; averages are over 75 adjacent frequencies. 110

List of Figures (Contd.)

		Page No.
Figure 4.5.	Model and observed temperature coherences over four separations Y. Box-like solid curves are model mean-gradient coherence. Dashed curves are for the same process-specified model as in Figure 4.3a. Solid curves are for the same wavenumber spectrum-specified model as in Figure 4.3b. The model parameters are the same for all separations for each model. The lower curve (dashed or solid) is the fine-structure coherence defined by equation (4.2.3). The upper curve (dashed or solid) is total coherence given by (4.2.2). At frequencies above the cutoff (where mean-gradient coherence drops to zero), the total coherence is the fine-structure coherence. Dotted horizontal lines are drawn at the level of significantly non-zero coherence with 95% confidence.	112
Figure 4.6.	Temperature half-coherence and eight-tenths coherence frequency as a function of vertical separation Y. Squares (circles) denote observations of eight-tenths (half) coherence. Solid (open) symbols are computed from IIWA (MSA) data. Solid (dashed) curves are drawn for the wavenumber spectrum-specified (process-specified) model used in previous figures. Note the process-specified model is equivalent to a k^{-2} wavenumber spectrum-specified model. The $k^{-2.5}$ spectrum-specified model fits the observations better than the k^{-2} model.	114
Figure 4.7.	Model and observed horizontal current spectra. Model curves for mean-gradient (dashed) and fine-structure (dot-dashed) contributions to the spectrum are given as well as their sum (solid), using a $k^{-5/2}$ spectrum in (a) and a $k^{-9/4}$ spectrum in (b). Error estimates for 95% confidence appear at the left	128
Figure 4.8.	Model and observed horizontal current difference spectrum for a separation Y = 6.3 m. Mean-gradient (dashed curve) and fine-structure (dot-dashed curve) contributions as well as their sum (solid curve) are drawn for the $k^{-9/4}$ spectrum model using the same parameters as in Figure 4.7b. An error estimate for 95% confidence appear at the left.	130

List of Figures (Contd.)

		Page No.
Figure 4.9.	Horizontal current half-coherence frequency as a function of vertical separation Y. The curve is from the $k^{-9/4}$ spectrum model used in the curves of Figures 4.7b and 4.8.	132
Figure 5.1.	Temperature contours, shear, N and Arctan (Ri) for 38.4-44.4 hours during the second experiment. (a) Contours of temperature in 0.02°C increments on the forward mast versus time. Tick marks are every meter in depth and every 10 minutes in time. (b) Finite-difference of horizontal current components (an estimate of shear) in sec^{-1} from the forward upper and forward lower propeller clusters. (c) N(t, 7.13 m) in rad/sec computed from thermistors at the extremities of the forward mast. (Scale is the same as in (b)). (d) Arctan (Ri) in degrees. Horizontal dashed lines are at Ri = 0.25, 1.0. (e) Sequential plot of shear estimate squared versus N^2(t, 7.13 m) from the data plotted in (b) and (c). Every third estimate (i.e., one every 2 minutes) is highlighted by a symbol. A line corresponding to Ri = 0.25 is drawn.	136
Figure 5.2.	Same as Figure 5.1 for 26.4-32.4 hours	137
Figure 5.3.	Coherence amplitude and phase of (a) N and Arctan (Ri), (b) shear and Arctan (Ri), and (c) N and shear. All are computed from a 3-day segment of the second experiment. Averages are over 18 adjacent frequencies; estimates of the level of significantly non-zero coherence with 95% confidence are drawn as dotted lines.	139
Figure 5.4.	Spectra of (a) shear over 6.3 m, (b) N (7.13 m) and (c) Arctan (Ri) using the same records as in Figure 5.3. Error estimates for 95% confidence are at the left	141
Figure 5.5.	Scatter plot of shear squared over 6.3 m versus N^2(7.13 m) of estimates made every 40 seconds during a 78-hour segment of the second experiment. Of the 7020 points, the 6881 with QUALITY higher than 95 at both the upper and lower cluster on the forward mast are plotted. The line corresponds to Ri = 0.25 .	143
Figure 5.6.	A histogram of Arctan (Ri) using the points plotted in Figure 5.5.	144

List of Figures (Contd.)

Page No.

Figure A.1. Spectra of W_T estimated using finite difference approximations to T_Z over different vertical separations δ (in cm). The spectra fail to show a cutoff at $\overline{N}$ and are more energetic than spectra of directly measured W. 156

Figure A.2. Admittance amplitude and phase for the model $W = a*W_T + n$ where W_T is estimated using finite difference approximations to T_Z over different vertical separations δ. Stable phase is indicative of significantly non-zero coherence between W and W_T. Amplitudes are less than unity for all separations available; they are closest to one for the smallest (88 cm) and the largest (713 cm) separations 158

Figure A.3. (a) Spectrum of T_t and (b) admittance of T_t with W for the model $T_t = a*W + n$. If the model were valid with constant $T_Z = 12.35 \times 10^{-3}$ °C/m, the calculated amplitude curve would fall on the horizontal line in (b). 160

Chapter 1. Introduction

In recent years observations and theoretical work have suggested that deep ocean internal waves and the details of stratification called fine-structure are highly interdependent. At first, these two topics were pursued separately. Early internal wave models used idealized profiles of buoyancy frequency N to derive wave functions. The simplest of these was the constant-N ocean; Fofonoff (1969) used such a model to derive various spectral quantities for comparison with moored measurements. In their synthesis of a wide-ranging body of observations into a universal isotropic spectral model for internal wave motions, Garrett and Munk (1972a) used an exponential profile for N(z). Their model was inadequate for wave frequencies ω near N(z), which led Desaubies (1973) to study the single turning-point problem of waves trapped between the surface and an exponential profile of N(z). But none of these models took account of the details of stratification: fluctuations on the order of about 1m to 10m in scale. Meanwhile, observations by moored instruments often failed to discern a cutoff at N(z) of the internal wave spectrum. Both horizontal current and temperature spectra often lacked sharp cutoffs at N(z), and vertical current was inferred from temperature measurements. Once electronic measurement of temperature and salinity was made possible, "continuous" profiles were able to resolve nearly ubiquitous deviations from smooth mean gradient profiles of roughly 1m to 10m size. These features were collectively called "microstructure." Cooper and Stommel (1968), Stommel and Federov (1968), and Tait and Howe (1968) provided some of the first deep ocean microstructure observations.

Gradually instrumentation became more sophisticated and Osborn and Cox (1972) were able to report fluctuations on scales of 1 cm or so. Of course, these fluctuations were called "microstructure" as well and fluctuations on scales 1m-10m were renamed "fine-structure." Some justification for the distinction is seen in the temperature gradient wavenumber spectrum of Osborn and Cox (1972) (their Figure 10) which shows a spectral well at roughly 50 cm wavelength. It was in the earlier period that the instrument used in the present study was designed so that its name, the Micro-scale Array (or MSA, as it is called) reflects the terminology used at that time. The sources of fine-structure amd microstructure were not known, and a body of speculative literature sprang up in response. Speculation continues today, but the primary factors appear to be interleaving of different water types (Osborn and Cox (1972)), the possibility of several double-diffusive processes (Turner (1973), Chapter 8), and breaking internal waves (Garrett and Munk (1972b)). It is this last possibility which is of interest here, since internal waves are ubiquitous just as is fine-structure, and their spectral level may be a saturation level (Wunsch (1975)). The quasi-permanent components of fine-structure (deviations from mean temperature and salinity gradients) which arise from interleaving, double diffusion, and wave breaking undoubtedly support internal wave motions which, in turn, distort the background quasi-permanent features, making distinction of internal waves and fine-structure difficult.

Internal waves and fine-structure can be entangled in a rather complicated way. Lazier (1973) showed measurements in which fine-structure

apparently propagated in a wave-like manner in a lake, McGorman and Mysak (1973) and Mysak and Howe (1976) demonstrated how short internal waves could be scattered by fine-structure. (Their model assumed fine-structure variation in N(z) was small compared to its mean; measurements clearly show this to be untrue in the main thermocline.) A note by Bell (1973) indicates that larger waves (longer than a few meters vertically) will propagate "essentially unaffected by fine-structure", since the correlation scale of fine-structure is quite small (only a few centimeters, according to Bell). Thus large vertical scale waves respond primarily to large-scale stratification features, an approximation which will be used throughout this work. It is further justified by our measurements, which are interpreted to show that the internal wave spectrum is red in wavenumber so that short waves have negligibly small energy compared to long waves.

The simplest effect fine-structure seems to have on moored spectra is kinematical. Since vertical motion was so difficult to measure (and still is!), oceanographers typically measured temperature instead and tried to infer vertical displacements from it. Inference of this kind depends on the validity of the simplified heat equation used and, more crucially, on being able to estimate the instantaneous vertical temperature gradient at the point of interest. Fine-structure and microstructure place adequate estimation of instantaneous temperature gradient beyond the realm of existing instrumentation. (The problem of inferring vertical current from temperature measurements is discussed in the Appendix.) Vertical and horizontal temperature coherence is also seriously hampered by fine-structure. Wunsch and Dahlen (1970) encountered this problem with their "internal wave antenna": a long

horizontal moored cable in the main thermocline near Bermuda designed to gather internal wave data. Two thermistors 1 km apart on that mooring showed negligible coherence at periods less than 8 hours. Their frustration with the apparent effects of fine-structure provided the motivation for designing the experiments which are at the core of the present work. They decided that simultaneous measurements of all three components of current along with temperature on an array were necessary to untangle the puzzle of deep ocean "microscale" fluctuations. The array needed to be rigid and instrumented to detect its own motions so that accurate measurement of water motions could be made. Most other microstructure instruments at the time were profilers (Gregg and Cox (1972)), Osborn and Cox (1972)) which, while able to traverse large sections of water column and sample different locations easily, are unable to distinguish time scales. A moored array is cumbersome and is sensitive to a limited wavenumber band, but is able to measure time mean quantities and distinguish motion on different time scales. Since Wunsch and Dahlen believed vertical temperature structure on scales of 1m to 10m to be interfering with their attempts to measure internal waves, the MSA was designed with vertical masts carrying seven thermistors roughly 1m apart. The two vertical masts were separated horizontally by 20 m with the intention of measuring horizontal temperature gradients believed typical of internal wave oscillations of "fine-structure." Chapter 2 describes the instrument, the experiments performed, and data handling procedures.

Modelling of the kinematic effects of fine-structure as a passive, random vertical field was first done by Phillips (1971). He imagined

fine-structure as a series of layers and sheets (homogeneous regions separated by infinitesimally thin high gradient regions) advected vertically by internal wave motions past a moored sensor. Moored spectra of such a step structure would exhibit an ω^{-2} frequency dependence. Garrett and Munk (1971) extended this approach by factoring the vertical field into mean-gradient and fine-structure terms, thus defining mean-gradient and fine-structure contributions to moored spectra. They calculated the fine-structure autocovariance (the Fourier transform of the fine-structure contribution to the frequency spectrum) as an integral over the spatial autocovariance of the passive field multiplied by the probability distribution of internal wave displacement differences. In order that the integral not diverge, the "fine-structure approximation" was made: that vertical displacement of the waves is large compared to the scale of the passive fine-structure. They were able to generalize their approach to include determination of fine-structure crosscovariance contributions so that both spectra and cross-spectra of fine-structure contributions could be estimated. Rather simple models of both fine-structure (sheets and layers again) and the internal wave spectrum were employed so that they failed to discern details of spectral behavior at $\omega \simeq N(z)$, including the relative levels of mean-gradient and fine-structure contributions.

McKean (1974) modified the approach of Garrett and Munk by formulating the problem in terms of the mean-square difference of fine-structure fluctuations: the structure function. This approach allowed him to perform explicitly an integral relation analogous to that of

Garrett and Munk connecting the fine-structure spatial and temporal structure function through a probability distribution of displacement difference. The advantage of this approach is that the structure function is well defined for any lag in a field with stationary increments, rather than being formally divergent as is the autocovariance (see McKean (1974)). Thus, once a probability distribution of internal wave displacement difference is chosen, the fine-structure contribution is exactly defined. McKean exploited this formulation to show results different than some of those of Garrett and Munk due to their approximations of autocovariances.

Joyce and Desaubies (1976) used McKean's formulation to interpret vertical temperature difference measurements, finding that spectra of this quantity were dominated by fine-structure contribution in the upper few octaves of the internal wave range, and beyond. They used a sheet-layer model of fine-structure with Poisson-distributed layer thicknesses. They interpreted Brown-WHOI CTD profiles in the main thermocline near their moored instruments according to the sheet-layer model and found fair agreement between fine-structure levels inferred from profiles and from moored temperature measurements using their model. Following McKean (1974), Joyce and Desaubies (1976) used a very simple model internal wave spectrum: a frequency power law extending to N and zero above N. Thus both give only asymptotic forms for various spectra and coherences valid for frequencies either much higher or much lower than N. For a given internal wave spectral slope, the sheet-layer model restricts fine-structure spectral contribution to a particular high (and low) frequency slope. Details of spectral behavior near N are left unspecified.

To date, mean-gradient internal wave and fine-structure internal wave effects (i.e., time-dependent fluctuations at a fixed position) have not been unambiguously distinguished by others. It is the task of this study to actually make that distinction. To make a semantic distinction between "internal wave" and "fine-structure" effects is misleading; they are both internal wave effects when both fine-scale vertical fluctuations and internal wave motions exist. What is conventionally called the internal wave contribution is the contribution internal waves would make to a temperature or horizontal current spectrum if the stratification were sufficiently smooth that only a mean-gradient in temperature and N(z) existed. We shall call this the mean-gradient contribution. What is called the "fine-structure contribution" arises from internal wave motions; it is that part of the spectrum produced by spatial variance in the vertical temperature or density gradient. The key to distinguishing mean-gradient and fine-structure effects is to describe the internal wave spectrum of vertical motion out to N(z) and beyond. We will show below that the shape of the internal wave cutoff is crucial in determining the shape of a measured temperature spectrum and coherence curves of vertically separated temperature measurements.

Assuming that long vertical waves propagate in ignorance of fine-scale fluctuations of N(z) (Bell (1973)), an internal wave model is developed in Chapter 3, in which waves are trapped in a model main thermocline. Vertical current is expected to be negligibly affected by fine-structure (discussed further later) thus the mean-gradient contribution arises directly from expressions for vertical displacement

spectra. The model is designed to show the details of the mean-gradient contribution of frequencies near N(z) so that only the main thermocline is modelled; the simultaneous existence of the seasonal thermocline is ignored. The wave functions turn out to be in terms of Hermite functions, thus spectral quantities can easily be evaluated explicitly numerically. Comparisons of model and measured spectral energy ratios and vertical current spectra are made in this chapter, confirming that the model of internal wave motions is consistent with the data. A short section is also included to discuss the apparent horizontal isotropy of the internal wave spectrum. With a good model of internal wave displacements near the turning point ($\omega = N(z)$), we are able to model fine-structure contributions accurately over a wide range of frequencies including N(z).

Several models of fine-structure are considered in Chapter 4, starting with the simple sheet-layer model used by Phillips (1971), Garrett and Munk (1971), McKean (1974), and Joyce and Desaubies (1976). Two generalizations of the Poisson-process model are made; layers of constant gradient and constant curvature are considered. These models can be described equivalently in terms of their vertical wavenumber spectra. Since the data do not seem well described by these models, a model using an arbitrary vertical spectrum is developed. This model seems to describe temperature spectra and coherence curves rather well at all frequencies in the large range considered. Can a similar model be developed for horizontal current fine-structure effects? A grossly simplified model along these lines seems to do well enough in describing first-difference shear, although details of other spectral quantities near N(z) are not well described.

Finally, Chapter 5 discusses the implications of fine-structure contributions for wave breaking. Does the internal wave spectrum determine the intensity of fine-structure? Garrett and Munk (1972b) proposed that wave breaking does take place, a conclusion based on their internal wave model spectrum (Garrett and Munk (1972a)). The MSA measurements can be interpreted as experimental evidence that breaking does occur. Fine-structure contributions to the spectra suggest that breaking is crucially related to the existence of fine-structure.

The proposed model uses an approach along the lines of Garrett and Munk (1972a) to develop a description of vertically long internal waves trapped in the main thermocline which displace a passive fine-structure field through the formalism of McKean (1974). The model includes internal wave turning-point behavior and generalizes the description of fine-structure. Fine-structure is modelled as a passive vertical field, but is it really passive? Lazier's (1973) measurements suggest that it may not be, that fine-structure may in part be small scale internal waves. The model is able to ignore fine-scale internal wave motions (i.e., treat fine-structure as passive) since the internal wave spectrum is strongly red in wavenumber. In other words, vertically long internal wave displacements are so much more energetic than fine-scale displacements that the former are the dominant contribution to the fine-structure structure function. Fine-structure itself may be (at least in part) internal waves, but the distinction is not important in calculating its kinematical contribution to fluctuations of temperature, horizontal current, static stability, and shear. This point will

be discussed further in Chapter 4. Conclusions about the nature and function of fine-structure in the deep ocean internal wave field appear in Chapter 6.

Chapter 2. Field Program

2.1 Instrumentation

Consistent with the design objectives discussed above, the MSA was built as an instrumented rigid frame in an H-shape consisting of a 20m long rigid horizontal spar with 8m tall vertical masts erected at each end. The frame was moored from a point just below its center of gravity; buoyancy was provided by two 1m diameter aluminum spheres which housed batteries and electronic data acquisition equipment. Each mast was filled with seven thermistors spaced roughly evenly along it. Novel propeller-cluster current meters were positioned at the ends of the masts. A compass, two accelerometers and a pressure transducer provided mooring motion information. A fin mounted on one mast was meant to orient the frame with respect to the horizontal current. After the first deployment, modifications were made in the instrument design for use in the second and third deployments. A brief description of the instrument operation will be given below to acquaint the reader with its measurement capabilities; see Shillingford (1976) and Shillingford and Dahlen (1976) for a more detailed description.

The frame itself (see Figure 2.1) consists of a horizontal spar of 8 inch diameter aluminum tube fitted to a central truss holding the two symmetrically placed hollow aluminum spheres. The masts are aluminum sailboat masts hinged at the ends of the spar so that they may lie nearly horizontally while the MSA is being assembled ashore; before the frame is lowered into the water at dockside for towing to the deployment site, the masts are erected to a vertical position. A system of stays and guy wires provides rigidity to the spar and masts and the strength necessary to withstand stresses encountered in towing and

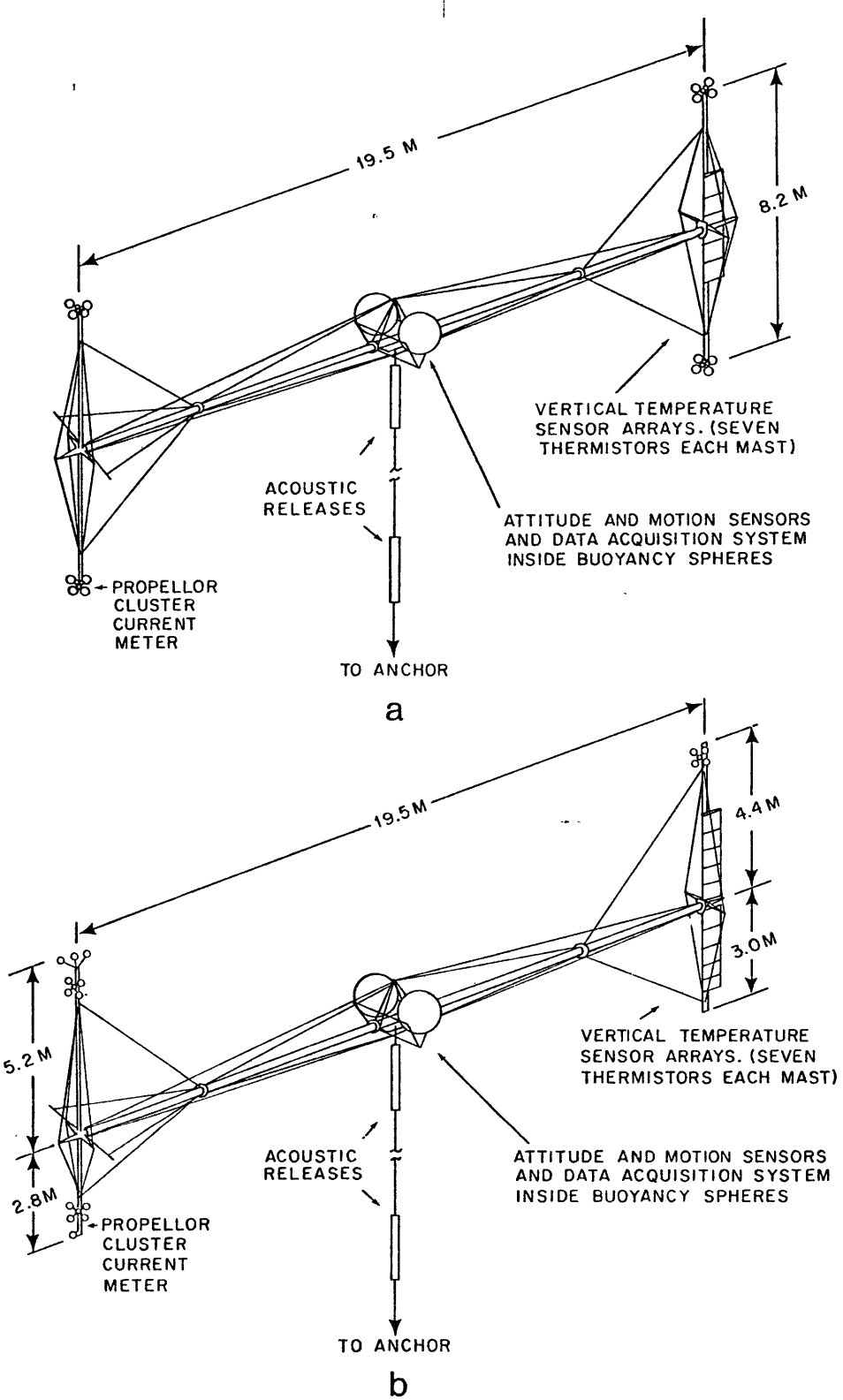


Figure 2.1. Schematic drawing of the MSA as it was configured for (a) the first experiment (October 1973) and (b) the second and third experiments (July 1975 and November 1975).

ascent and descent. The fin is attached to one mast, designated the "aft mast," to orient the MSA with respect to the horizontal current when it is moored. The MSA acts as a weather vane because of this fin; it has been estimated from tests in a tidal estuary, and calculations, that the whole frame has a response time constant of 15 minutes to a step change in horizontal current. During the first experiment the MSA did not "weather vane" satisfactorily, impairing the ability of the current meter propeller clusters to measure currents. A larger fin was used in the second and third deployments, resulting in greatly improved current data quality. The importance of weather vane performance appears in the discussion of propeller cluster data reduction.

To facilitate deployment on the second and third experiments, both the masts were raised with respect to the spar from their positions in the first experiment. To ensure better resolution of vertical velocities in times of slack horizontal current, propellers from the aft lower propeller cluster in the first experiment were redistributed; three were added to the forward upper cluster and one was added to the forward lower cluster, leaving no propellers in the aft lower position in the second and third experiments. This shift in propeller cluster coverage is the major difference between the first experiment and the succeeding ones.

Electronic data acquisition was accomplished using appropriate conversion of analog to digital signals which were then recorded on open-reel magnetic tape in IBM computer-compatible format. The data acquisition system was designed to operate at low power from a bank of mercuric oxide batteries located in one sphere (the "battery sphere").

The "electronics sphere" contained the accelerometers and compass as well as the data acquisition system. Operating life of the MSA is primarily dependent upon tape capacity. The sampling interval was set to 10 seconds for the first and third experiments and to 40 seconds for the second experiment. The typical design life using a 40 second sampling interval is 33 days, during which the system consumes about 2417 watt hours of electrical energy and records fifty-three million bits of information on magnetic tape. The output from each propeller (dual, phase shifted pulse trains) is integrated over an interval 1.312 seconds less than the sampling interval. During the last 1.312 seconds of each sampling interval all variables are sampled and recorded.

Mooring motion is detected by measurements of pitch and roll attitudes and heading of the frame and pressure. Two accelerometers located inside the electronics sphere were capable of measuring deviations from level to a resolution of ±0.51 milliradians. This angular deviation corresponds to a resolution of pitch and roll-induced displacements at the extremities of the frame of roughly ±0.5 cm and ±0.2 cm respectively. The compass resolved heading using a 128-level binary format, giving an angular resolution of ±1.41 degrees true heading. The pressure transducer output is electronically interpreted to give measurements on two scales. The coarse and fine scale ranges and resolutions are 0-990 dbar ±0.48 dbar and 450-820 dbar ±0.18 dbar respectively. In preparation for deployment the accelerometers were calibrated and checked using a two-axis rotary table, the compass was checked by swivelling the whole MSA on the dock while ascertaining heading with a theodolite sighted toward geographical landmarks, and the pressure transducers were calibrated and checked using a dead weight tester.

Temperature measurements were made using two networks of thermistors each consisting of seven externally mounted thermistors packaged within titanium cylinders and two precision resistors of fixed resistance, located inside the electronics sphere. The fourteen external thermistors were mounted in pairs of roughly corresponding positions on the two masts. They were temperature-cycled and calibrated at 7 temperatures in the 0° C to 19° C range to a tolerance of 0.01° C. Test experience indicates retention of calibration stability in situ within 0.001° C for months. The data acquisition electronics sampled the thermistor readings to give an allowable range of 7.5° C to 19.1° C with a resolution of ±0.0015° C. Each thermistor was packaged to give a time constant comparable to the system sampling rate for each experiment to reduce spectral aliasing. Experience indicates that calibrations of absolute temperature change by as much as 0.01° C when they are taken from the test bath to room temperature, then replaced in the test bath; the resolution of relative temperature does not change during such a procedure. This change in absolute calibration results in an uncertainty in absolute temperature for each thermistor. A procedure designed to correct for this calibration shift was used to refer the temperature measured by each thermistor to the others so that calculations of temperature gradients could be made reliably. Discussion of this correction is given in the section on data reduction.

Clusters of propellers were used as current meters on the MSA. Each set of three propellers in a cluster gave a determination of the current relative to the frame of the MSA. The procedure followed in determining these currents is given below in the section on data reduction. Here we shall discuss the operation of the individual propellers.

Each propeller has nearly identical characteristics and is made of syntactic foam with six blades each 7 cm long mounted on a rotor of 7 cm diameter. The propellers are impregnated with grease to enhance mass stability under pressure and each is balanced in sea water to within 50 dyne-cm static imbalance and 2 grams of neutral density.

Balancing is done to minimize loads on the graphite journal bearings which hold the rotor shaft in place thus minimizing the propeller threshold. One face of each propeller hub carries six small magnets and these travel past two electronic hall effect chips in the stator which give a step signal upon magnetic excitation. The output of each propeller is two shifted square waves which are interpreted electronically, summed over an accumulation interval, and stored on magnetic tape. During the first experiment one pulse was counted for each 1/6 propeller revolution; subsequently due to an improved scheme of pulse train interpretation, one pulse was counted for each 1/24 propeller revolution. This translates to one pulse counted for each 11.1 cm and 2.78 cm of flow along the propeller axis for the first and subsequent experiments, respectively.

The angular response of the propellers is such that

$$K\omega = \cos^{n}\theta$$

where ω is the number of output counts per meter flow along the propeller axis, θ is the angle between the current vector and the propeller axis, and n and K are parameters characterizing the shape and level of the response curve. The parameter n varies according to mounting configuration of each propeller due to shadowing by other propellers in the cluster.

The level 1/K is 9 counts per meter and 36 counts per meter for the first and subsequent experiments, respectively. This response curve is reliable for angles θ less than 55°; to assure full coverage of a large solid angle of possible current vector directions with respect to the MSA frame, propellers of differing orientation were grouped into clusters. The preferred orientation of each cluster was directly ahead along the MSA x-axis (the spar). The fin mounted on the aft mast was meant to keep each cluster pointing into the horizontal flow. The total solid angle "field of view" of a cluster of seven propellers is considerably larger than that provided by only four, which is the reason the cluster arrangements were modified for the last two experiments. The response curve and the parameters K and n were determined from extensive tow tank calibration. The stall speed of the propellers was also estimated to be 0.25 cm/sec during these tests.

2.2 Experiments

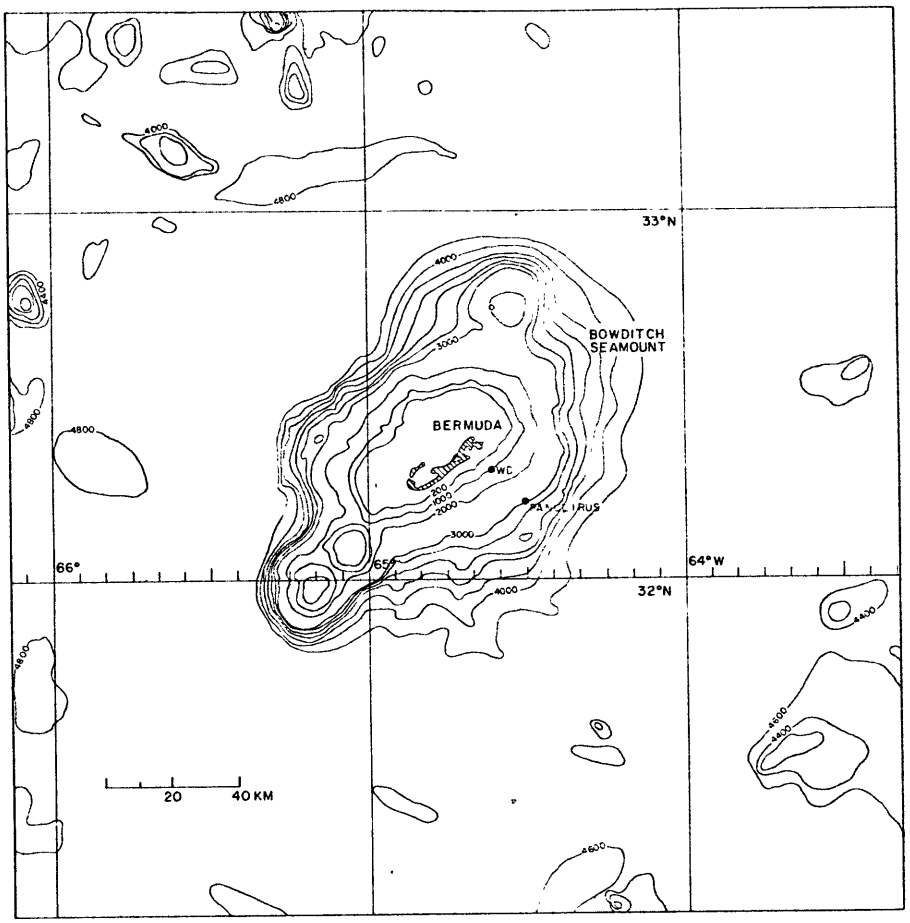
The MSA was deployed three times in nearly identical locations: moored at roughly 650 m depth in water 1000 m deep on the slope off the southeast coast of Bermuda. In all deployments it was assembled ashore alongside a dock in St. George's Harbor, then towed along the surface to the experiment sites. After towing, a mooring line was attached at sea and payed out from a winch on the R/V Panulirus II. Then an anchor was attached and cut loose from the ship. The MSA sank at roughly 1.4 m/sec until the anchor touched bottom. Recovery was accomplished by acoustic telemetry with the lower of the two acoustic releases mounted just beneath the MSA in the mooring line (an extra release was used for redundancy). After surfacing the MSA was again towed into St. George's Harbor.

The particular features of each of the three experiments are reviewed in this section.

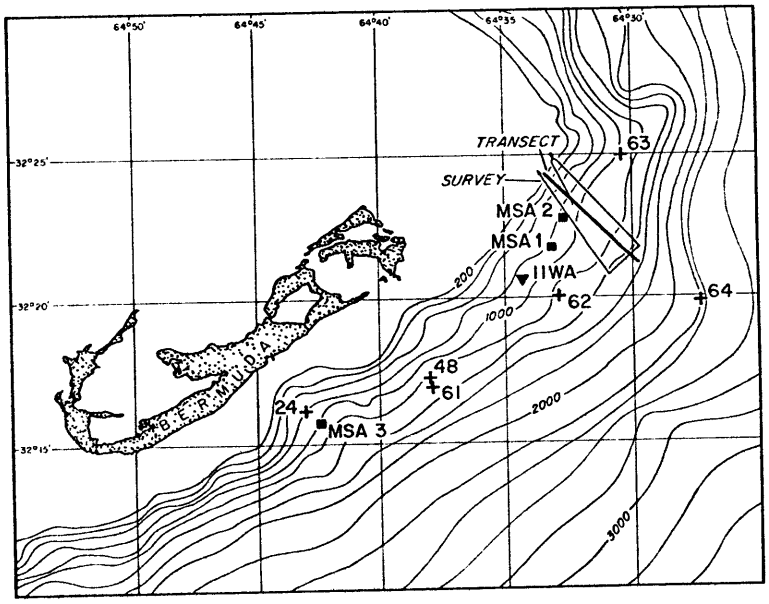
The first was made in October, 1973. Configured as in Figure 2.1a, the MSA was towed to a location 9 km east of St. David's Head (see Figure 2.2) (64°33'10" W, 32°21'45" N) in a water depth of 932 m. The instrument was placed at 679 m depth for 9 days. After 6.5 days the system stopped logging data due to failure of the tape recorder. All of the thermistors operated satisfactorily during the six days of records logged, although two were found to exhibit drift of roughly 0.01° C during the course of the experiment. Accelerometer, compass, and pressure records were of excellent quality. The roll accelerometer record shows that the roll attitude changed by almost 5 mrad over the course of the experiment, corresponding to an excursion of 2 cm at the ends of the masts. This largest excursion occurred with a time scale of roughly 30 minutes; other, smaller, excursions in roll roughly half as large occurred on the same time scale. The currents in the propellers induced by roll motions are smaller (5 cm/30 min = 0.00278 cm/sec) than can be detected by the clusters so that no correction for frame roll motion was done. Pitch motions were not negligible, however. Several pitch "events" occurred during the experiment with peak-to-peak amplitudes of as much as 20 mrad. These events were bursts of oscillatory motion characterized by a period of roughly 1-2 minutes. The velocities induced at the mast ends could be as large as 20 cm/min = 0.33 cm/sec, requiring correction to be made in the current records for this motion. The pitch events are thought to be caused by horizontal currents broadside to the spar, exciting resonant oscillation of the frame about its mooring point beneath the two

Figure 2.2. Charts of Bermuda. (a) Gross topography adapted from Wunsch (1972) showing the location of the Panulirus hydrographic stations and the Wunsch and Dahlen (1970) ("WD") moored experiment. (b) Local topography of the southeast Bermuda slope drawn from Defense Mapping Agency Hydrographic Center Chart N.O. 26341 and a local survey made from R/V Panulirus (shown in Figure). A transect through this survey is shown from which the profile in Figure 3.5 is drawn. Sites of the three MSA experiments are shown with squares; the IIWA experiment and its orientation is shown schematically by a triangle. Crosses represent Brown-W.H.O.I. CTD stations from R/V Knorr Cruise 52 (No. 48, 27 October 1975; Nos. 61-64, 1 November 1975) and R/V Eastward (No. 24, 18 October 1975).

a.


33°N
32°N
66°
65°
64°W
BOWDITCH
SEAMOUNT
BERMUDA
WC
ATLANTIS
4000
4800
3000
200
1000
2000
4600
20
40 KM

b.


64°50'
64°45'
64°40'
64°35'
64°30'
32°25'
32°20'
32°15'
TRANSECT
SURVEY
63
MSA 2
MSA 1
IIWA
62
64
48
61
24
MSA 3
BERMUDA
200
1000
2000
3000

instrument spheres by vortex shedding (J. Shillingford, personal communication). Propeller records in this experiment show considerable intermittency. Certain propellers failed at the start and others failed part way through the experiment. Since at least 3 propellers are needed to define a current vector, the intermittency creates sections of the record during which no velocity can be defined adequately. Also, the MSA did not weathervane satisfactorily as evidenced in the current records by currents veering off abeam to the frame. Cases also occurred of little horizontal flow while vertical flow was of the same magnitude as horizontal flow, causing the current vector to be well out of the "field of view" of the propeller clusters. In the resultant gappy records of current components, a 90 hour section was chosen during which all four current meters were functioning with only occasional intervals of poor quality. These lapses of poor quality generally lasted one or two hours and occurred roughly at 3 to 6 hour intervals. The determination of sections of poor quality is discussed in the section on data reduction.

The second deployment was made in July, 1975, configured as in Figure 2.1b. This mooring site was roughly two km NNE of the first experiment at a location 64°31'40" N, 32°22'45" N. The instrument was placed at 628 m depth where the total water depth was 914 m. The experiment was planned to last over a month, but the data acquisition system was found to have failed completely after 10 days. The cause was a tiny leak at a stainless steel helium leak test bulkhead fitting. Corrosion of aluminum unnoticed after previous time at sea allowed roughly a liter of seawater to leak into the electronics sphere. Fortunately none of the internal wiring was touched by the water, however the resulting high humidity inside the sphere caused the electronics to slowly malfunction

resulting in eventual failure of the whole system. Thermistor circuitry suffered most severely, leaving only the first 78 hours of temperature data usable. The compass and roll accelerometer functioned well (as before, negligible roll motion was encountered). The pitch accelerometer failed after six days so that velocity records could be only that long, even though the propellers continued to work for another two days. Circuitry measuring analog signals suffered most, but signals requiring no analog-to-digital conversion (e.g., propellers) fared comparatively well during the 9 day degradation process. The first 3.5 day segment of the temperature records is of good quality; all thermistors seem to have functioned properly and without drift. The propeller data is excellent and provides the core of the observational data to be interpreted here.

The third deployment occurred in November, 1975. Originally, the MSA was to be launched from the R/V Knorr of W.H.O.I. After heavy seas and strong winds caused the MSA to be damaged during attempted deployment, the instrument was returned to Bermuda for repair. The damage resulted from misplacement of a tending line; the line pinched a thermistor cable and crushed the body of one thermistor. The instrument was repaired and inspected, but at least one leak in the damaged thermistor cable went undetected. Since this cable was a virtual electrical ground, all the thermistors failed within minutes of launching at dockside. As in previous experiments, the MSA was towed to a position southeast of Bermuda, this time 5.3 km SE of Devonshire Bay at 64°42'30" W, 32°15'40" N. The instrument was placed at 721 m in a total depth of 1153 m. The experiment was planned for eight days and, except for the thermistors, the system functioned as planned. The propeller data is of good quality for a 50 hour period; the longest such period in this dataset.

A moored array experiment related to the MSA work was carried out from August to October, 1974 near the MSA sites. It was designed as an antenna to detect intermediate scale internal wave motion (hence its name, the intermediate internal wave array, or IIWA) consisting of three conventional intermediate moorings, each instrumented with one AMF vector averaging current meter and four temperature/pressure recorders (see Wunsch and Dahlen (1974)). The moorings were arranged nearly in an equilateral triangle nominally 200 m on a side (see Figure 2.2b). Locations of the moorings were determined by acoustic survey; ship location during the survey was determined by ranging by the NASA satellite communications antenna at St. David's Island. The temperature/pressure recorders were nominally at 670, 680, 700, and 740 m depth on the two deeper moorings and 650, 660, 680, and 720 m depth on the shallower one. The recorders sampled every 16 minutes. Fifty-day records were used to compute temperature vertical difference spectra and temperature coherences from these instruments, the only use made of these data in this study.

2.3 Data Handling

This section describes data handling past initial calibration procedures. Shillingford (1976) describes details of the initial calibration of all instruments. Besides procedures for interpretation of digital thermistor and propeller records, computation of derived quantities (buoyancy frequency, shear, and Richardson number) is discussed here.

To compensate for the unknown thermistor calibration offsets mentioned previously, a procedure was developed to estimate these offsets so that temperatures recorded by the thermistors could be related to one another. The procedure rests on the assumption that a constant mean vertical

temperature gradient exists during each experiment at the depth of the MSA. Time averages of temperature for each thermistor were calculated for various durations, ranging from 1 to 6 days; for each averaging interval all 14 temperature averages were regressed in a least-squares sense against a constant gradient. Provision was made for the near constant downward pitch of the MSA frame by a few degrees; pitch motion was negligibly small for these purposes. If the assumption of a constant gradient is a good one, the offset for each thermistor temperature average from the regression line should be invariant with averaging interval. Normally the offsets were found to be of the order 0.01° C (the value expected from laboratory tests) or smaller. In the first experiment two thermistors' offsets were found to change with the averaging interval used. These two (T3 and T13) could not be reliably used for measurements of temperature differences (approximation of instantaneous temperature gradients). When the remaining twelve thermistors were regressed together, offsets were found to agree within 0.002° C (less than the sampling least count) for different averaging intervals. In the second experiment T3 was replaced, but the new thermistor showed an unusually large offset (0.13° C) although it showed no evidence of drift. This new T3 was omitted from the least-squares regression, lest it influence the calculated gradient unduly. Its offset was then calculated from the regression gradient computed without it. Again, offsets were found to agree within 0.002° C for different averaging intervals. The absolute temperature is still unknown to 0.01° C, but a fixed relation has been established amongst thermistors to within 0.002° C so that temperature differences may be calculated reliably.

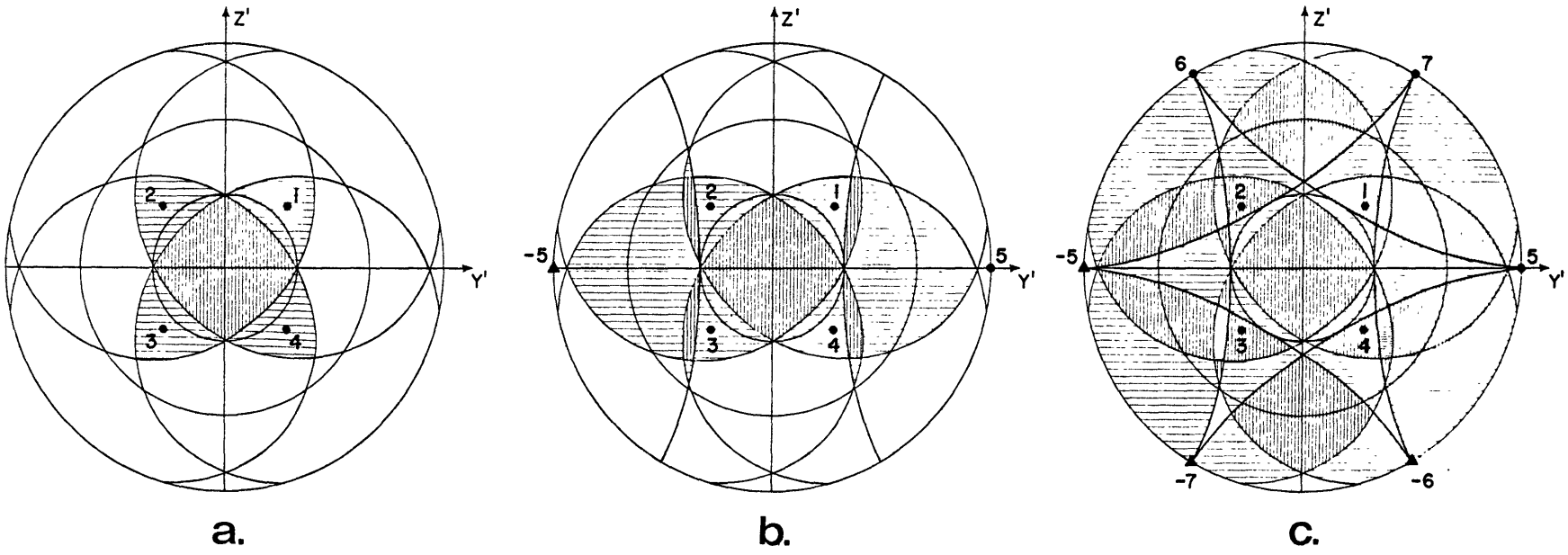


Figure 2.3. Field of view of propeller clusters. These figures represent the solid angle of a hemisphere (whose equator is in the y'-z' plane - see Figures 2.4 and 2.5) for which clusters of 4(a), 5(b), and 7(c) propellers reliably resolve a current vector. Concentric circles represent 30°, 60°, and 90° angles with respect to the x'-axis (out of the y'-z' plane). Numbers 1-7 represent orientations of propellers (see also Figure 2.4); note propellers 5-7 are oriented parallel to the y'-z' plane, thus both positive and negative directions appear on the 90° circle. Sparsely horizontally hatched regions represent solid orientations for which one combination of three propellers adequately resolves the flow. Vertically hatched regions represent orientations covered by two combinations and heavily horizontally hatched regions represent orientations covered by three combinations.

Interpretation of the propeller data is more involved. As discussed previously, the propellers in each cluster have fixed orientations relative to the MSA frame. They measure currents most accurately when the current vector is sufficiently close to parallel to the horizontal spar, flowing from the forward mast to the aft mast. The locus of angles which produce reliable measurements of current is determined by the necessity that the current vector make an angle of 55 degrees or less with at least three of the propellers in each cluster. If the current vector makes an angle sufficiently small with respect to only two or fewer propellers, the measurement is suspect. The current vector orientations with respect to each cluster which satisfy the condition of three or more propellers making acceptably small angles with current vectors define the "field of view" of the cluster. With four propellers, the cluster has a relatively limited flower-shaped field of view (Figure 2.3a). With additional propellers oriented as in the forward lower and forward upper clusters, the current meters achieve a larger field of view (Figures 2.3b, 2.3c). The forward upper cluster achieves very nearly total coverage of the forward looking hemisphere. During intervals of backwash of the clusters (flow from aft to forward) it is assumed (by default) that the clusters act bidirectionally. This assumption has not been substantiated by tow tank tests (we expect shadowing may take place), but another interpretation of flows in the positive x direction is not known. Further discussion of this matter appears after the paragraphs describing computation of current vectors and their quality.

For each combination of three propellers a unique current vector can be calculated. Referring to Figure 2.4, one may write the equation relating the current vector $\vec{V} = u\hat{x} + v\hat{y} + w\hat{z}$ with magnitude $V = |\vec{V}|$ to the

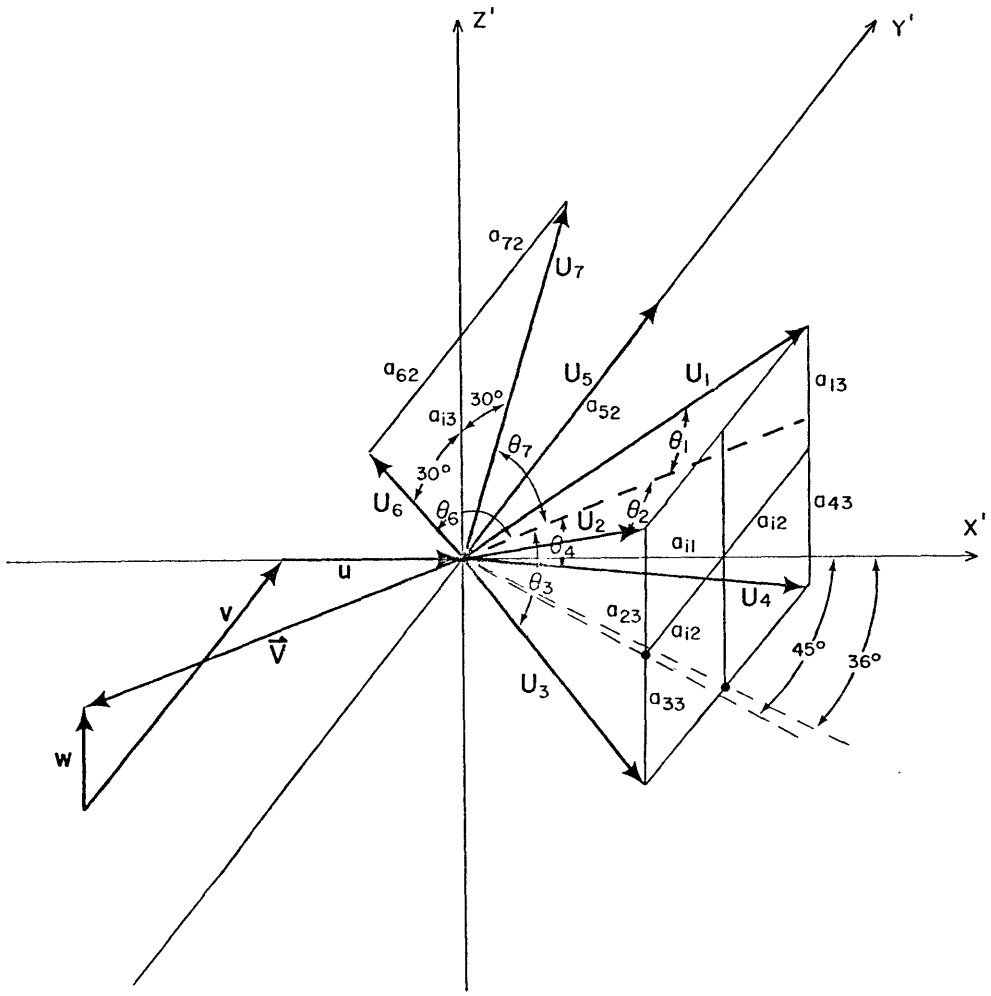


Figure 2.4. Perspective sketch of propeller axis orientations. Flows U_1-U_7 along propeller axis 1-7 make angles θ_1-θ_7 with the current vector $\vec{V}$. These flows are resolved as $U_i = a_{i1}\hat{u}' + b_{i3}\hat{v}' + c_{i3}\hat{w}'$. Counts from combinations of three propellers can be used to compute $\vec{V} = \hat{u}' + \hat{v}' + \hat{w}'$.

flow parallel to each of the propellers U_i: $U_i = V \cos \theta_i$. The angle θ_i is the angle between $-\hat{a}_i$ (the direction of flow U_i) and $\vec{V}$. Since the propellers respond as $K\omega_i = V \cos^{n_i} \theta_i$ where ω_i is the number of counts per time interval and K and n_i are as before, the equation is:

$$U_i = V^{\frac{n_i-1}{n_i}} (K\omega_i)^{\frac{1}{n_i}}$$

U_i may be expressed as the dot product of the unit vectors describing the propeller axis and the components v_j of $\vec{V}$:

$$U_i = -\sum_{j=1}^{3} a_{ij} v_j \ .$$

Substituting $V = (\sum_{j=1}^{3} v_j^2)^{1/2}$ one obtains a system of nonlinear simultaneous equations for v_j:

$$(\sum_{j=1}^{3} v_j^2)^{\frac{n_i-1}{2n_i}} |K\omega_i|^{\frac{1}{n_i}} \operatorname{sgn}(K\omega_i) = -\sum_{j=1}^{3} a_{ij} v_j \ .$$

A unique solution to this system of equations is found numerically using Newton's method after explicitly calculating a first guess to v_j obtained by assuming $n_1 = n_2 = n_3$.

For each time interval one is required to choose, from the available combinations of propellers, which combination gives the most reliable estimate of the current vector. The approach of considering some weighted average of the current vectors computed from several different combinations was considered unnecessarily complicated and possibly misleading, since the

propellers working most reliably might not be weighted sufficiently heavily. After several different schemes for choosing the best combination of propellers were tried, a criterion somewhat subjectively based on the performance characteristics of the propellers was chosen. After computing a current vector, the angles θ_i were examined to see if they fell in the range of angles for which the calibration response curves are valid. To make a quantative comparison between current vectors from different combinations, an arbitrary function was chosen which falls monotonically from a value 100 at $\theta_i = 0$ to 95 at $\theta_i = 55°$ (the cutoff angle) and falls much more steeply at greater angles to 0 at 90°. The function has continuous slope. The simple average of the function values for the three propellers with the highest quality was chosen to give the most reliable estimate of the current vector for each time interval. For clusters with four propellers (quads), this algorithm was computationally relatively efficient, as there are only four combinations of 3 propellers in this configuration. For clusters with five or seven propellers, to save computation the four combinations in the quad were considered first; if a current vector with quality greater than 95 was found, none of the propellers outside the quad were considered.

Tow tank tests in fresh water indicate the stall speed of the propellers is less than 0.25 cm/sec, which, for a 10 second sampling interval, is less than the least count the propellers can resolve. The resolution of each propeller at higher than stall speeds is ±0.16 cm/sec for 10 second sampling and ±0.036 cm/sec for 40 second sampling. This error might well be compared with the typical deviations between current vector magnitudes computed from different propeller combinations with the same high quality (quality greater than 99.97; corresponding to $30° < \theta_i < 40°$).

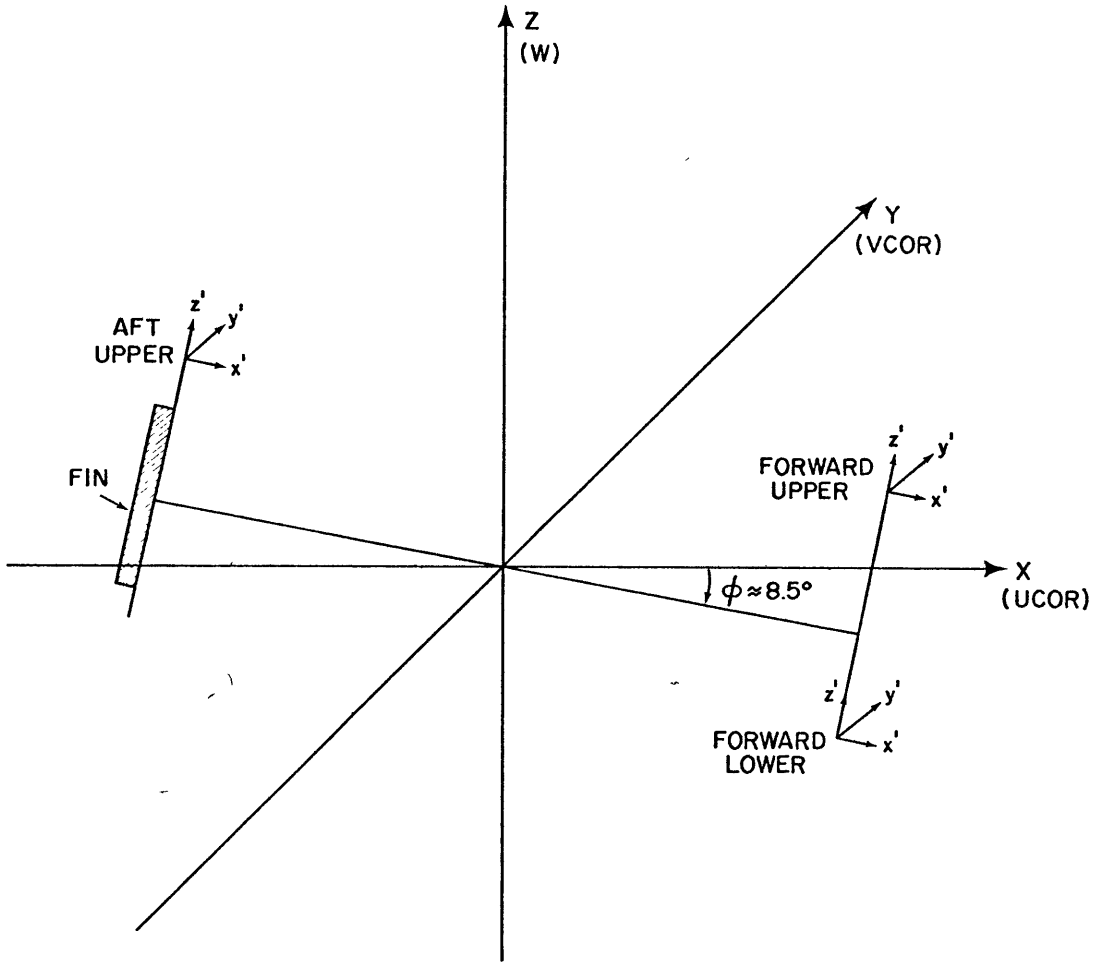


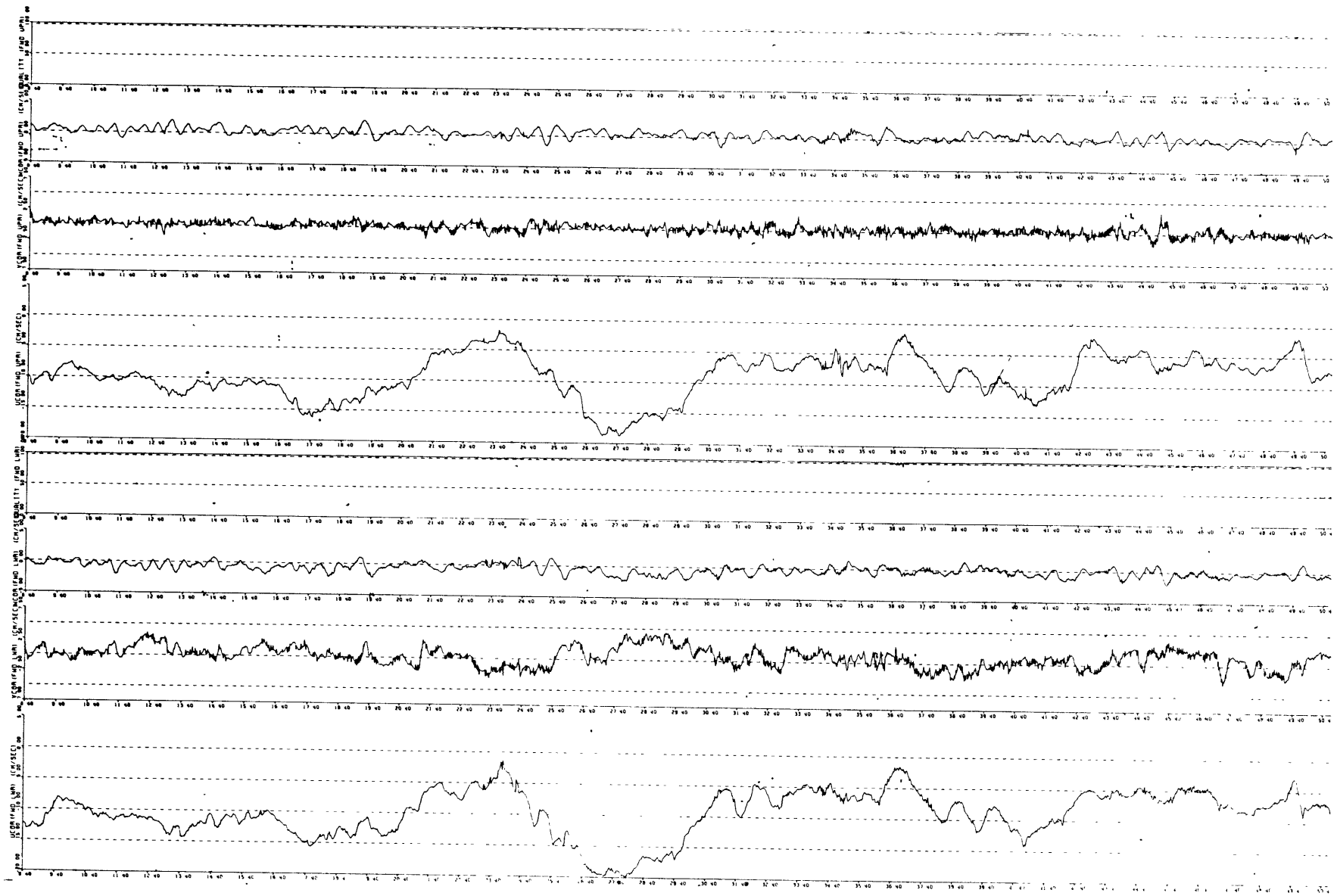
Figure 2.5. Sketch of MSA geometry. Current records at each cluster are resolved into UCOR, VCOR, and W components in the X, Y, and Z directions, a cartesian frame referred to the MSA azimuth and geographical vertical. In normal operation UCOR is negative and VCOR and W are small compared with the magnitude of UCOR.

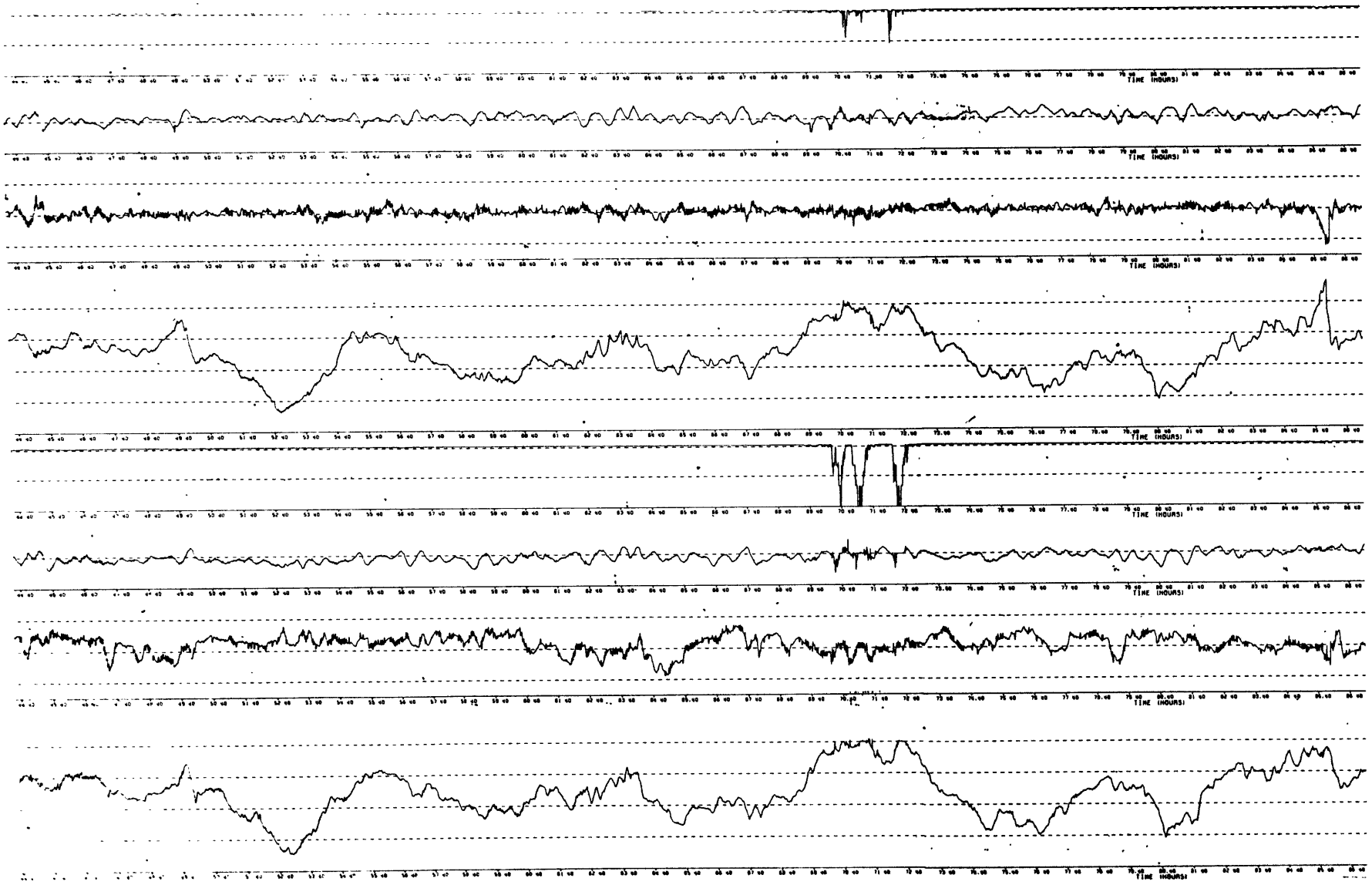
These deviations in total speed are ±0.2 cm/sec for currents of 10 cm/sec. The deviations in the current components are trigonometrically related.

After records of the current components relative to the frame of the MSA were derived, they were referred to two different coordinate systems: one with the MSA frame projected onto a horizontal plane (i.e., a cartesian system whose azimuth is fixed to the frame heading and whose vertical is the geographic vertical); the other the normal system of geographical coordinates. A summary sketch of these conventions is given in Figure 2.5. Once transformation to the first system of coordinates is made, transformation to the second is merely a matter of trigonometry. Several corrections to the currents must be made to account for frame motion (pitch and yaw). Vertical translation of the MSA frame was considered negligibly small, since pressure records in all three experiments show deviations from the mean between 0.36 and 0.72 dbar with strong semidiurnal periodicity. We expect these to be due primarily to surface tides rather than to vertical motion of the MSA (see Panicker and Schmidt (1975)). No pressure fluctuations of higher frequency are apparent in the records.

Instantaneous values of pitch and a piecewise cubic spline interpolant to pitch were used to correct for pitch orientation and motion. Mean pitch angles for the three experiments were -8.50°, -8.24°, and -9.06°, respectively, indicating the forward section of the spar sloped downwards. Correction was made for heading change by differentiation of a piecewise quartic interpolant to compass heading. This procedure introduced a spurious signal in the azimuthal component of velocity referred to the MSA frame, but at known high frequencies (the presence of

Figure 2.6. Typical current records from forward lower (lower four plots) and forward upper (upper four plots) clusters taken during the second experiment (in two overlapping frames). UCOR, VCOR, W, and QUALITY are plotted versus time (labeled in 1-hour increments) for each cluster. Note UCOR is normally negative (see Figure 2.5) and of larger magnitude than other components. VCOR is noisier than UCOR and W due to correction for heading change with time, but the noise is the same for both forward records. QUALITY is above 95 (upper dashed line in QUALITY plots) except at isolated times. Note that when UCOR approaches zero at about 70.40 hours, QUALITY drops more severely for the forward lower record (a 5-propeller cluster) than for the forward upper record (a 7-propeller cluster) because of the greater "field of view" of the forward upper cluster (see Figure 2.3).




TIME (HOURS)

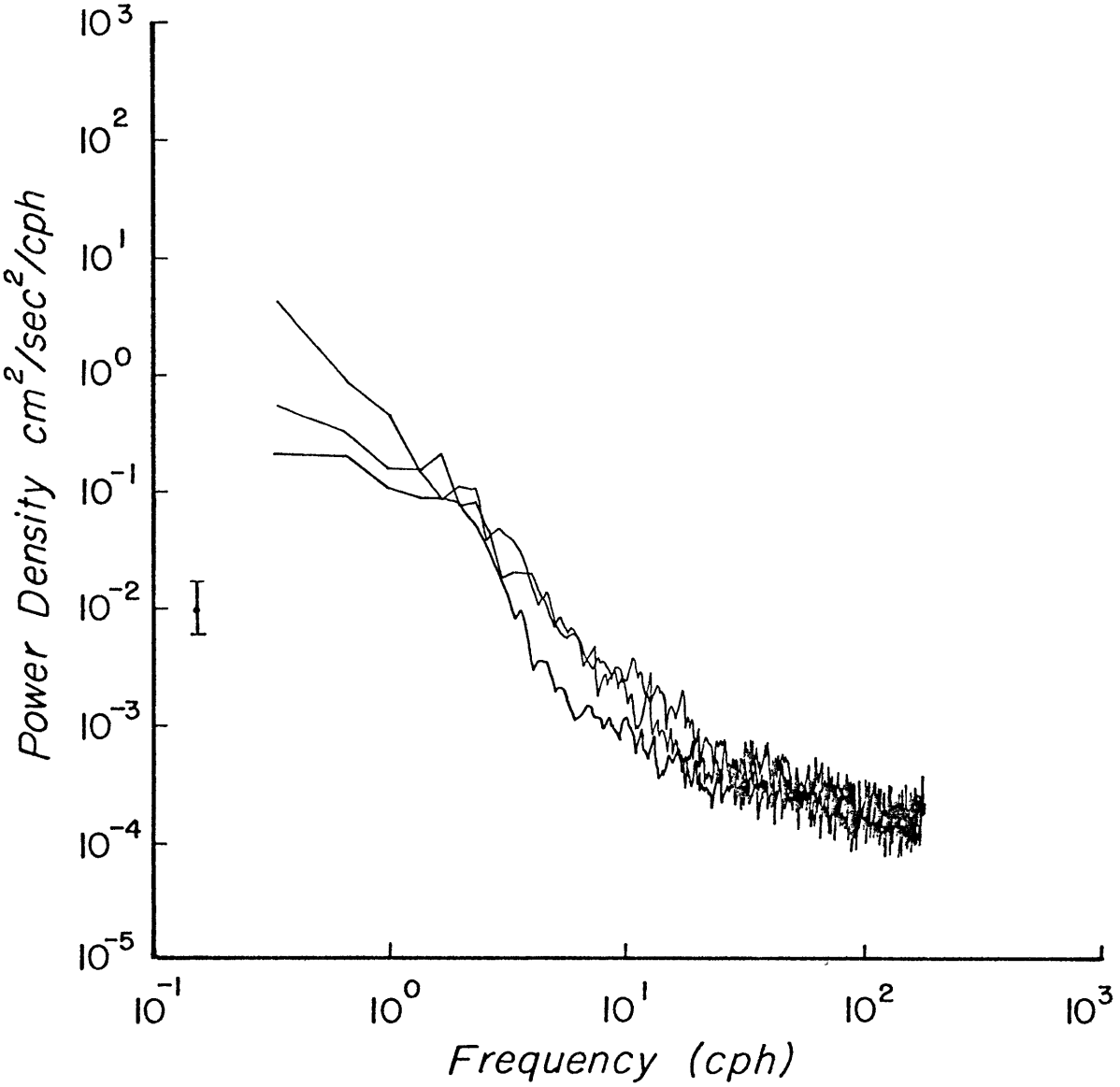


Figure 2.7. Spectra of UCOR, VCOR, and W from a 2-day segment of records from the third experiment. At low frequencies UCOR is most energetic and W is least energetic. Averages are over 16 adjacent frequencies; an error estimate for 95% confidence is at the left. The spectra coalesce above about 20 cph and flatten; the variance from about 18 cph to 180 cph corresponds to a standard deviation of roughly 0.2 cm/sec, the estimated measurement noise. All error estimates for spectra in this study were computed following Jenkins and Watts (1969).

this noise can be seen in typical current records shown below). The noise introduced was due to differentiation of a coarsely digitized signal. In the third experiment, digital smoothing of the compass signal using a running average filter was done to eliminate this noise.

Examples of current records from the second experiment appear in Figure 2.6. Note the occasional drop in quality corresponding to slack horizontal flow in both forward upper and forward lower current meter records. Spectra from the third experiment of all three components from the forward upper current meter are displayed together in Figure 2.7. Variance in these spectra at high frequencies (above about 20 cph) corresponds to an earlier estimate of ±0.2 cm/sec as a typical uncertainty in current measurement.

Several records derived from temperature and velocity records were constructed. An important class of these are time series of buoyancy frequency $N(t;\delta)$ based on pairs of temperature records of different vertical separations δ. The buoyancy frequency was estimated assuming a constant temperature-salinity (T-S) relation over the appropriate range taken from the Panulirus station records. In addition, T-S relations from several Brown-W.H.O.I. CTD (Conductivity-Temperature-Depth) stations near Bermuda in October 1975 (furnished courtesy of N. Hogg of W.H.O.I.) were used to verify the Panulirus T-S relation on smaller scales. These T-S relations were edited, however, to exclude deviations from a smooth curve. A. J. Williams reported (private communication, 1976) finding occasional salinity-compensated temperature inversions with a free-fall microstructure probe. These show deviations of up to 0.007 ‰ salinity in a 5 m thick inversion, but most inversions show deviations of no

more than a third this value. These features are relatively rare (one or two were encountered in some traverses of the main thermocline, sometimes none), thus determinations of $N(t,\delta)$ at most times will be subject to deviations from the mean T-S curve of less than about 0.001 ‰. The computation routines of N. Fofonoff of W.H.O.I. were used to calculate $N(t,\delta)$ using salinity calculated from a local linear fit to the historical monthly mean T-S curves (curves courtesy of E. Schroeder of W.H.O.I.). In addition to instantaneous values, the time averaged buoyancy frequency for a given separation $\overline{N}(\delta)$ was calculated. The notation $\overline{N}$ refers to δ = 7.1 m when δ is not otherwise specified.

The error in N^2 is estimated using a local linear approximation to the equation of state. Contributions to this error arise from uncertainty in temperature and salinity. The difference in specific volume between two positions in the vertical, separated by D is:

$$\Delta\alpha = \alpha_T \Delta T + \alpha_S \Delta S$$

where $\Delta T = dT \pm \delta_T$ and $\Delta S = \frac{dS}{dT} \Delta T \pm \delta_S$ are the temperature and salinity differences and dS/dT is the local slope of the T-S curve. The uncertainty δ_α in $\Delta\alpha$ is:

$$\delta_\alpha = \alpha_T \delta_T \pm \alpha_S \frac{dS}{dT} \pm \alpha_S \delta_S \ .$$

The uncertainty in N^2 is taken as $(-g/D)\delta_\alpha = \delta_{N^2}$:

$$\delta_{N^2} = \frac{-g}{D} \left(\left(\alpha_T \pm \alpha_S \frac{dS}{dT} \right) \delta_T \pm \alpha_S \delta_S \right)$$

Table 2.1 gives the values used for α_T, α_S, $\frac{dS}{dT}$ and δ_T and δ_S and the resulting δ_{N^2}. For D = 0.80 m (the closest thermistor spacing on the MSA) $\delta_{N^2} = \pm 6.45 \times 10^{-5} \text{sec}^{-2}$ when $\delta_S = 0.007$ ‰. For a larger spacing (7.5 m) $\delta_{N^2} = \pm 6.88 \times 10^{-6} \text{sec}^{-2}$ when $\delta_S = 0.007$ ‰. This is an estimate for rather infrequent, extreme deviations δ_S. A more realistic estimate for most of the record is $\delta_{N^2} \leq \pm 10^{-6} \text{sec}^{-2}$, which corresponds to an uncertainty of about 5% when compared to $\bar{N}$ = 3.35 mrad/sec.

Table 2.1

$$\delta_{N^2} = \frac{-g}{D}\left(\left(\alpha_T \pm \alpha_S \frac{dS}{dT}\right)\delta_T \pm \alpha_S \delta_S\right)$$

$\alpha_T = 2.165 \times 10^{-4} \text{cm}^3/\text{g}/°\text{C}$

$\alpha_S = -7.237 \times 10^{-4} \text{cm}^3/\text{g}/‰$

dS/dT = slope of T-S curve = 0.1855 ‰/°C

δ_T = uncertainty in temperature = 0.002 °C

δ_S = uncertainty in salinity (see below)

Contributions to δ_{N^2}

		D = 0.80 m	D = 7.5 m
$-\frac{g}{D}(\alpha_T + \alpha_S \frac{dS}{dT})\delta_T$		$\pm 2.0 \times 10^{-6} \text{sec}^{-2}$	$\pm 2.1 \times 10^{-7} \text{sec}^{-2}$
$-\frac{g}{D}\alpha_S \delta_S$	$\delta_S = 7. \times 10^{-3}$ ‰	$\pm 6.25 \times 10^{-5} \text{sec}^{-2}$	$\pm 6.67 \times 10^{-6} \text{sec}^{-2}$
	$\delta_S = 1. \times 10^{-3}$ ‰	$\pm 8.94 \times 10^{-6} \text{sec}^{-2}$	$\pm 9.52 \times 10^{-7} \text{sec}^{-2}$

Shear records were estimated by differencing the horizontal current records from the upper and lower current meters on the same mast. For the

shear record to be meaningful, the quality of both horizontal current records must be high. Fortunately both meters on the same mast are subject to the same noisy correction due to azimuth so that the resulting difference is not degraded by its presence. If errors in horizontal current are assumed to be no more than ±0.2 cm/sec, we find that the error in shear is roughly $\pm 0.2/\sqrt{2}\ 800\ \text{sec}^{-1} = \pm 1.75 \times 10^{-4}\ \text{sec}^{-1}$.

Various Richardson numbers for the flow were also computed. These were found by dividing the buoyancy frequency squared by the shear squared. Since both buoyancy frequency and shear were computed as finite differences over vertically separated instruments, these are only estimates to the gradient or overall Richardson number (Turner 1974). As only one vertical separation is available for estimation of shear, the most realistic estimate of the overall Richardson number is found using buoyancy frequency derived from a temperature difference taken over a comparable separation. The meaning of this estimate of Ri will be considered in more detail in Chapter 5.

Chapter 3. Internal Waves without Fine-Structure

3.1 An internal wave model

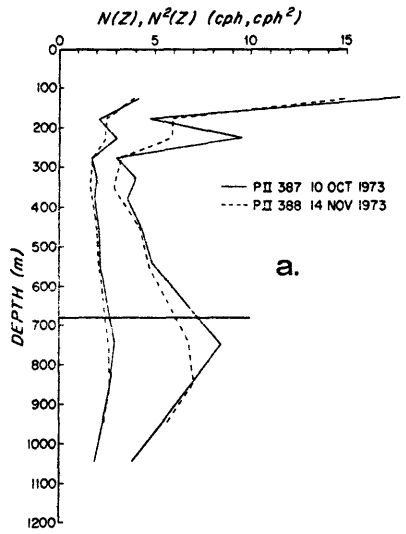
To describe the various spectra produced from the MSA data sets, a model will be developed here for internal waves based on a smooth density structure (no fine structure) which is imagined to be the profile upon which waves with scales much longer than the fine structure scale are dynamically dependent. Figure 3.1 shows the coarse profiles of buoyancy frequency squared obtained from the Panulirus station data. We see that the MSA was moored at a depth above the maximum in N^2, but below the local minimum of the 18° C water. This leads one to expect that waves at frequencies higher than 1 cph or so but below the maximum buoyancy frequency (about 3 cph) will be trapped vertically in a region bounded above and below by less strongly stratified water through which they are unable to propagate freely. Then a two-turning point solution to the internal wave equation is suggested and is derived below. The derived wave functions have vertical modes with their wavelength determined by the separation of the turning points at a given frequency. These solutions approach the familiar WKBJ solutions far from the turning frequency (see Phillips (1966), Chapter 5).

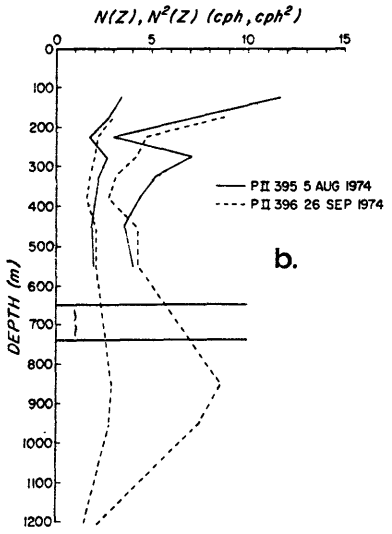
Consider the linearized Boussinesq equations for inviscid, incompressible, rotating flow:

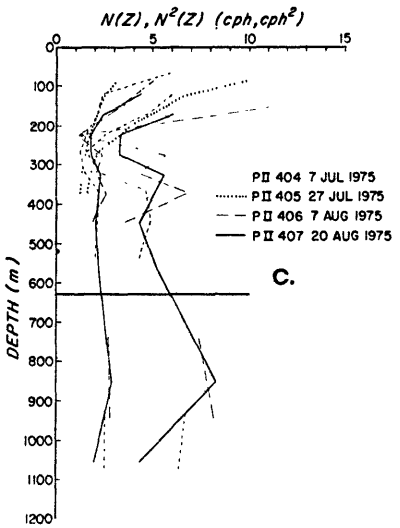
$$u_t - fv = \frac{-p_x}{\rho_o} \tag{1a}$$

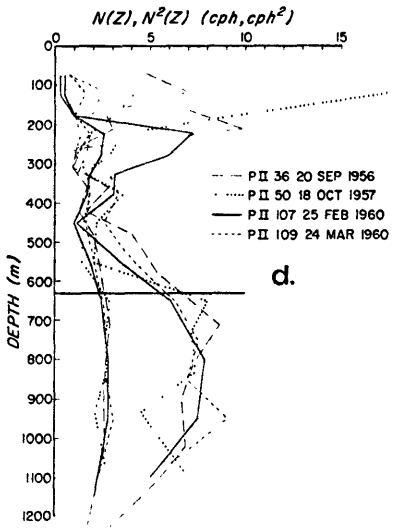
$$v_t + fu = \frac{-p_y}{\rho_o} \tag{1b}$$

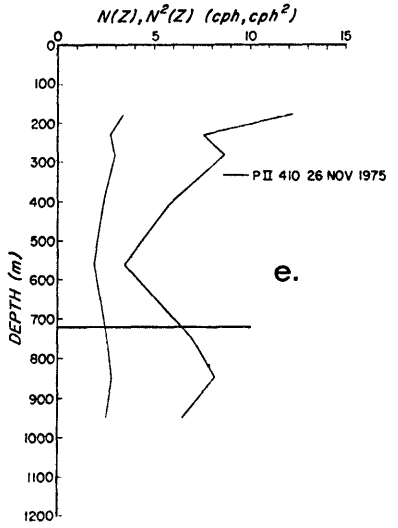
Figure 3.1. Profiles of N(z) and $N^2(z)$ from selected Panulirus stations. Profiles in (a), (c), and (e) correspond to stations closest the time of the three MSA experiments. The profiles in (b) were taken during the IIWA experiment. Profiles in (d) are typical historical stations for which the temperature at the MSA depth was comparable to that measured during the second experiment (i.e., anomalously warm: approximately 16° C at 630 m). Presence of fine-structure contributes to the roughness of the profiles. The maximum in N(z) (i.e., the center of the main thermocline) occurs at about 700-800 m. Heavy horizontal lines are drawn at the depth of the appropriate MSA experiment in each frame. The IIWA instrument depths are bracketed in (b).


N(Z), N²(Z) (cph, cph²)
0
5
10
15
100
200
300
400
500
600
700
800
900
1000
1100
1200
DEPTH (m)
PII 387 10 OCT 1973
PII 388 14 NOV 1973
a.


N(Z), N²(Z) (cph, cph²)
0
5
10
15
100
200
300
400
500
600
700
800
900
1000
1100
1200
DEPTH (m)
PII 395 5 AUG 1974
PII 396 26 SEP 1974
b.


N(Z), N²(Z) (cph, cph²)
0
5
10
15
100
200
300
400
500
600
700
800
900
1000
1100
1200
DEPTH (m)
PII 404 7 JUL 1975
PII 405 27 JUL 1975
PII 406 7 AUG 1975
PII 407 20 AUG 1975
c.


N(Z), N²(Z) (cph, cph²)
0
5
10
15
100
200
300
400
500
600
700
800
900
1000
1100
1200
DEPTH (m)
PII 36 20 SEP 1956
PII 50 18 OCT 1957
PII 107 25 FEB 1960
PII 109 24 MAR 1960
d.


N(Z), N²(Z) (cph, cph²)
0
5
10
15
100
200
300
400
500
600
700
800
900
1000
1100
1200
DEPTH (m)
PII 410 26 NOV 1975
e.

$$w_t = \frac{-p_z}{\rho_o} - g\frac{\rho'}{\rho_o} \tag{1c}$$

$$u_x + v_y + w_z = 0 \tag{1d}$$

$$\rho_t' + w\overline{\rho_z} = 0 \tag{1e}$$

where u, v, w are the velocities in the x,y,z (east, north, up) directions, p and ρ' are the perturbation pressure and density, $\overline{\rho_z}$ is the time averaged vertical density gradient, and $f = 2\Omega$ sin (latitude) is the Coriolis parameter. Defining $N^2(z) = \frac{-g}{\rho_o}\overline{\rho_z}$ as the buoyancy frequency squared, an equation for w(z) is found:

$$w_{zz} + \alpha^2 \left(\frac{N^2(z) - \omega^2}{\omega^2 - f^2}\right) w = 0 \tag{2}$$

where it is assumed all variables are of the form $e^{i(kx + \ell y - \omega t)}$ and $\alpha^2 = k^2 + \ell^2$. It is convenient to adopt the transformation used by Garrett and Munk (1972a):

$$\begin{vmatrix} u \\ v \\ w \end{vmatrix} = \mathrm{Re} \begin{vmatrix} i\,U_L(z)\cos\phi - U_T(z)\sin\phi \\ i\,U_L(z)\sin\phi + U_T(z)\cos\phi \\ W(z) \end{vmatrix} e^{i(kx + \ell y - \omega t)} \tag{3}$$

where $\phi = \mathrm{Cos}^{-1}(k/\alpha) = \mathrm{Sin}^{-1}(\ell/\alpha)$ and U_L and U_T are the longitudinal and transverse currents associated with the wave, referred to the horizontal direction of phase propagation. Note the horizontal kinetic energy $\frac{1}{2}(uu^* + vv^*) = \frac{1}{2}(U_L^2 + U_T^2)$. From (1d), $U_L = W_z/\alpha$, and further,

that $U_T = \frac{f}{\omega} U_L = \frac{f}{\omega\alpha} W_z$. Then:

$$\text{H.K.E.} = \frac{1}{2}(uu^* + vv^*) = \frac{1}{2}(1 + \frac{f^2}{\omega^2})(\frac{W_z}{\alpha})^2 \tag{4a}$$

$$\text{V.K.E.} = \frac{1}{2}(ww^*) = \frac{1}{2} W^2(z) \tag{4b}$$

$$\text{P.E.} = \frac{1}{2} \frac{N^2(z)}{\omega^2} ww^* = \frac{1}{2} \frac{N^2(z)}{\omega^2} W^2(z) \tag{4c}$$

where horizontal kinetic energy (H.K.E.), vertical kinetic energy (V.K.E.), and potential energy (P.E.) associated with the flow have been defined.

Then (2), the internal wave equation, may be written as:

$$W_{zz} + \beta^2 W = 0 \qquad \beta^2 = \alpha^2 (\frac{N^2(z) - \omega^2}{\omega^2 - f^2}) \tag{5a}$$

or as

$$W_{zz} + b^2 q(z) W = 0 \qquad b^2 = \frac{\alpha^2 \omega^2}{\omega^2 - f^2}, \quad q(z) = \frac{N^2(z)}{\omega^2} - 1 \tag{5b}$$

To obtain a uniformly valid asymptotic solution to (5b) where $q(z) > 0$ in the region between two turning points $\mu_1 < z < \mu_2$ and negative elsewhere, a generalized Langer's transformation (Nayfeh 1973) is performed, letting:

$$W(z) = \chi^{-1/4} \psi$$

$$\zeta = \zeta(s) = \int^z \sqrt{q(\tau)}\, d\tau \tag{6}$$

$$\chi = \frac{q(z)}{\zeta'^2}, \quad s = s(z)$$

We choose ζ'^2 so that it has two simple zeros at $s = \pm 1$. The upper and lower turning points μ_2 and μ_1 are represented by $s = 1$ and $s = -1$ respectively. Let

$$\zeta'^2 = 4a^2(1-s^2) \tag{7}$$

so that

$$\zeta = 2a \int_{-1}^{s} \sqrt{1-\tau^2}\, d\tau = \int_{\mu_1}^{z} \sqrt{q(\tau)}\, d\tau \tag{8a}$$

Equation (8a) gives a dispersion relation

$$2a \int_{-1}^{1} \sqrt{1-\tau^2}\, d\tau = \int_{\mu_1}^{\mu_2} \sqrt{q(\tau)}\, d\tau. \tag{8b}$$

The related equation for W(z) is:

$$\psi_{ss} + 4a^2b^2(1-s^2)\psi = 0. \tag{9a}$$

A further transformation of variables, letting $\eta = 2\sqrt{ab}\, s$, gives the parabolic cylinder equation in standard form:

$$\psi_{\eta\eta} - (\frac{\eta^2}{4} - ab)\psi = 0 \tag{9b}$$

which has solutions $\psi(\eta) = AU(-ab,\eta) + BV(-ab,\eta)$, the parabolic cylinder functions (Abramowitz and Stegun (1964)). If we assume the waves are truly trapped in the model thermocline, we neglect the top and bottom of the ocean and force the solutions to decay as they cross the turning points. Imposing this boundary condition requires (Nayfeh (1973))

$B \equiv 0$ and $ab = n + \frac{1}{2}$. Equation (8b) is then:

$$b = \frac{\pi(n + \frac{1}{2})}{\int_{\mu_1}^{\mu_2} \sqrt{q(\tau)}\, d\tau} \tag{10}$$

where n is a non-negative integer, the mode number. Then

$$\begin{aligned} \psi(s) &= AU(-n - \tfrac{1}{2},\ 2\sqrt{n + \tfrac{1}{2}}\, s) \\ &= A \exp\{-(n + \tfrac{1}{2})s^2\}\ H_n(\sqrt{2n+1}\ s)\, 2^{-n/2} \end{aligned} \tag{11}$$

where H_n are the Hermite polynomials (Abramowitz and Stegun (1964)). For an arbitrary profile of $N^2(z)$ with two turning points we now have a uniformly valid asymptotic (in depth) solution to (5):

$$\begin{aligned} W(z) &= \chi^{-1/4}\psi \\ W(z) &= \sqrt{\frac{2n+1}{b}}\, \frac{(1-s^2)^{1/4}}{q^{1/4}(z)}\, A \exp\{-(n + \tfrac{1}{2})s^2\} H_n(\sqrt{2n+1}\ s)\, 2^{-n/2} \end{aligned} \tag{12}$$

Rather than consider a general $N^2(z)$ profile, we shall choose for convenience a profile for which s is a simple function of z through the definition (8a). We choose a parabolic form for $N^2(z)$ so that the solutions are parabolic cylinder functions <u>exactly</u>; no longer are they only asymptotically correct. The justification is that this choice simplifies computation enormously without sacrificing realism. The waveguide will now be symmetric about the center of the main thermocline ($z = 0$) with turning points at $z = \pm\mu$. The waveguide narrows toward higher frequencies.

We will restrict ourselves to the solutions germane to the MSA measurements, thereby avoiding the second-order turning point at z = 0 (see Smith 1975). Well below the turning frequency at a given depth, equation (5) approaches the equation normally solved asymptotically by the WKBJ method (Phillips (1966)). At low frequencies the solutions will depend only on the local N(z) in the WKBJ manner, not on the large scale profile of N(z). Thus reasonably good results are expected for frequencies below 1 cph, even though the parabolic model thermocline is grossly incorrect in this range.

Specifically, our choice for q(z) is:

$$q(z) = \frac{N^2(z)}{\omega^2} - 1 = \left(\frac{N_o^2 - 1}{\omega^2}\right)\left(1 - \frac{z^2}{\mu^2}\right) \tag{13}$$

so that $s = z/\mu$ and (10) becomes:

$$b = \frac{2n+1}{\sqrt{\frac{N_o^2}{\omega^2} - 1}} \tag{14a}$$

which can be expressed variously using (5a) as

$$\mu\alpha\sqrt{\frac{N_o^2 - \omega^2}{\omega^2 - f^2}} = 2n + 1 \quad \text{or} \quad \mu\beta\sqrt{\frac{N_o^2 - \omega^2}{N(z)^2 - \omega^2}} = 2n+1 \tag{14b}$$

The wave functions are then, with $\eta = \sqrt{2n+1}\,\frac{z}{\mu}$;

$$W(z) = \sqrt{\mu}\, A \exp\{-\eta^2/2\} H_n(\eta) 2^{-n/2} \tag{15a}$$

$$U_L(z) = \frac{\sqrt{2n+1}}{\alpha\sqrt{\mu}} A \exp\{-\eta^2/2\} \left(nH_{n-1}(\eta) - \frac{1}{2} H_{n+1}(\eta)\right) 2^{-n/2} \tag{15b}$$

$$U_T(z) = \frac{f}{\omega} \frac{\sqrt{2n+1}}{\alpha\sqrt{\mu}} A \exp\{-\eta^2/2\} \left(nH_{n-1}(\eta) - \frac{1}{2} H_{n+1}(\eta)\right) 2^{-n/2} \tag{15c}$$

The constant A can be determined in terms of the energy density per unit volume of the wave field. As in Garrett and Munk (1972a),

$$E(\alpha,\omega;z) = \frac{1}{2}(U_T^2 + U_L^2 + W^2 + \frac{N^2(z)}{\omega^2} W^2). \tag{16}$$

Having already chosen $z = 0$ as the center of the thermocline ($N^2(0) = N_o^2$), we additionally observe that $E(\alpha,\omega;z)$ is symmetric about $z = 0$ so that for normalization we need only consider the semi-infinite domain $z > 0$. Integration past the edge of the wave guide is possible because the wave functions are uniformly valid.

$$E(\alpha,\omega) = \int_o^\infty dz\, E(\alpha,\omega;z) \tag{17a}$$

$$E(\alpha,\omega) = \int_o^\infty \frac{1}{2}(U_T^2 + U_L^2 + W^2 + \frac{N^2(z)}{\omega^2} W^2)dz \tag{17b}$$

$$E(\alpha,\omega) = \frac{\mu}{2} \frac{A^2\sqrt{\mu}\, n!}{\sqrt{2n+1}} \frac{2N_o^2 - f^2(\frac{N_o^2}{\omega^2} + 1)}{2(\omega^2 - f^2)} \tag{17c}$$

or

$$A^2 = E(\alpha,\omega)\ \frac{2}{\mu}\ \frac{\sqrt{2n+1}}{\sqrt{\pi}\ n!}\ \frac{\omega^2 - f^2}{N_o^2 - \frac{f^2}{2}\left(\frac{N_o^2}{\omega^2} + 1\right)} \tag{18a}$$

When $\omega >> f$, as is the case for the data we consider from the MSA:

$$A^2 = E(\alpha,\omega)\ \frac{2}{\mu}\ \frac{\sqrt{2n+1}}{\sqrt{\pi}\ n!}\ \left(\frac{\omega}{N_o}\right)^2 \tag{18b}$$

Finally, the expressions for the wave functions are:

$$\begin{vmatrix} U_{L_n} \\ U_{T_n} \\ W_n \end{vmatrix} = \frac{E(\alpha,\omega)\sqrt{2n+1}}{\sqrt{\pi}\ n!\ 2^{n-1}}^{\frac{1}{2}} \left(\frac{\omega}{N_o}\right) \cdot \begin{vmatrix} \left(\frac{N_o^2 - \omega^2}{\omega^2 - f^2}\right)^{\frac{1}{2}} \frac{1}{\sqrt{2n+1}}\, e^{-\eta^2/2}\,(nH_{n-1}(\eta) - \frac{1}{2}H_{n+1}(\eta)) \\ \frac{f}{\omega}\left(\frac{N_o^2 - \omega^2}{\omega^2 - f^2}\right)^{\frac{1}{2}} \frac{1}{\sqrt{2n+1}}\, e^{-\eta^2/2}\,(nH_{n-1}(\eta) - \frac{1}{2}H_{n+1}(\eta)) \\ e^{-\eta^2/2}\,H_n(\eta) \end{vmatrix} \tag{19}$$

To explicitly compute the wave functions or spectral quantities derived from them, a model form for $E(\alpha,\omega)$ is needed. A priori, there is no reason to believe that some modes will be excited and others not, in an irregular manner. Rather, one expects all modes to be excited on the average according to the spectrum $E(\alpha,\omega)$. Let us borrow from the knowledge we already have of $E(\alpha,\omega)$ from previous internal wave studies. Garrett and Munk (1972a, 1975) synthesized a model for internal wave motions well away from the inertial and buoyancy frequencies using wave

functions computed from an exponential profile for N(z). The spectrum they chose in the later paper behaves as

$$E(\alpha,\omega) = E(\alpha/\alpha_o)^{-2.5}(\omega/N_o)^{-2} \tag{20a}$$

for wavenumbers α greater than α_o and frequencies well above f. (Wave number dependence α^{-2} is indicated in more recent work by Cairns and Williams (1976)). In the two-turning point model we expect to be in a similar wavenumber range (since the thermocline waveguide is roughly 500 m wide at $\omega = N(z_o)$, where z_o is the model MSA position). We then choose a similar form, finding it quite adequate, as we shall see when comparing with observations:

$$E(\alpha,\omega) = E(\alpha/\alpha_o)^{-p}(\omega/N_o)^{-q} \tag{20b}$$

Note that $\frac{\alpha}{\alpha_o} = 2n+1$, having chosen α_o as the lowest (n=0) mode wavenumber. Equivalently $\beta/\beta_o = 2n+1$, so $E(\beta,\omega)$ may be used alternatively.

Using this spectrum one may calculate explicitly energy spectra, spectral ratios and coherences for comparison with the data generated statistics. Using the definitions (4):

$$\text{V.K.E.} = \frac{1}{2}\sum_n E(2n+1)^{-p}\left(\frac{\omega}{N_o}\right)^{-q+2}\frac{\sqrt{2n+1}}{\sqrt{\pi}\, n!\, 2^{n-1}}\, e^{-\eta^2} H_n^{\,2}(\eta)$$

$$\text{H.K.E.} = \frac{1}{2}\,1 + \frac{f^2}{\omega^2}\sum_n E(2n+1)^{-p}\left(\frac{\omega}{N_o}\right)^{-q+2}\frac{N_o^{\,2}-\omega^2}{\omega^2-f^2}\,\frac{1}{2n+1}\,\frac{e^{-\eta^2}\left(nH_{n-1}(\eta) - \frac{1}{2}H_{n+1}(\eta)\right)^2}{\sqrt{\pi}\, n!\, 2^{n-1}} \tag{21}$$

$$\text{P.E.} = \frac{N^2(z)}{\omega^2}\ \text{(V.K.E.)}$$

We shall be interested in the ratio P.E./H.K.E. and V.K.E./H.K.E. to compare with measurements made by others and with other models. If it is assumed that modes are not phase-locked (i.e., each mode is randomly phased with respect to other modes) internal wave coherences between pairs of instruments separated spatially may be computed. For vertical velocity, for instance, instruments at $z = z_1$ and $z = z_2$ have a coherence

$$\mathrm{coh}(W(z_1), W(z_2)) = \frac{\sum_n W_n(z_1)e^{i\phi_n} \sum_m W_m(z_2)e^{-i\phi_m}}{\sqrt{\sum_n W_n^2(z_1)} \sqrt{\sum_m W_m^2(z_2)}} \tag{22a}$$

The surviving terms in the numerator after averaging over phase differences are those for which $m = n$. Thus the coherence is

$$\mathrm{coh}(W(z_1), W(z_2)) = \frac{\sum_n W_n(z_1)W_n(z_2)}{\sqrt{\sum_n W_n^2(z_1)} \sqrt{\sum_n W_n^2(z_2)}} \tag{22b}$$

The coherence has zero phase in this case, since effective wave propagation is horizontal in a modal model. In the next section these model spectral quantities will be compared with those computed from the data. Appropriate asymptotic limits (in frequency) will be considered there.

3.2 Comparisons with data

In this section the thermocline mode model developed in the previous section will be shown to compare well with the appropriate measured spectra. In constructing this model, it was assumed that longer waves dominate the energy spectra; this implies that spectra of vertical current will be negligibly altered by the presence of fine structure, since

longer waves are responsive primarily to variations in the stratification of their scale or larger (see Bell (1973) and Chapter 1). Then vertical current is taken as the clearest indicator of internal wave motion. Equations (3.1.1e) and (3.1.4a) show that temperature and horizontal current are functions of vertical current multiplied by factors involving the stratification; thus we expect spectra of these quantities to be altered by the details of the buoyancy frequency profile (i.e., by fine-structure). In comparing model spectra to observed spectra, we shall rely heavily on vertical current data. The first comparison we make is between predicted and observed ratios of potential energy to horizontal kinetic energy (P.E./H.K.E.) and vertical kinetic energy to horizontal kinetic energy (V.K.E./H.K.E.). These ratios are independent of level and frequency dependence of the internal wave energy spectrum. Since horizontal current is expected to be affected by fine-structure, each of the observed ratios will be diminished slightly at frequencies near N(z) and higher. The ratios computed from the model will then consistently appear higher than the observed ratios in the frequency range where fine-structure contribution is significant. The second comparison is between observed and model spectra of vertical current.

Making these two comparisons will involve choosing several parameters. The local time-averaged buoyancy frequency $\overline{N}$ is chosen for N(z). The shape of the model parabolic profile is specified by the height of the instrument z above the thermocline center and the maximum buoyancy frequency $N(0) = N_o$. For present purposes one need only choose N_o, since the model spectra depend only on $z/\mu = ((N_o^2 - N^2(z)/(N_o^2 - \omega^2))^{1/2}$. We must specify the energy spectrum $E(\beta,\omega)$ by choosing p for the energy

ratio comparison, and, additionally, q and the level E for the vertical current comparison.

Energy ratios may be explicitly written as:

$$\text{P.E./H.K.E.} = \frac{\omega^2 - f^2}{\omega^2 + f^2} \frac{N^2(z)}{N_o^2 - \omega^2} \frac{\sum_n \frac{(2n+1)^{\frac{1}{2}-p}}{2^n\, n!} e^{-\eta^2} H_n^2(\eta)}{\sum_n \frac{e^{-\eta^2} [nH_{n-1}(\eta) - \frac{1}{2} H_{n+1}(\eta)]^2}{2^n n! (2n+1)^{\frac{1}{2}+p}}} \tag{1a}$$

$$\text{V.K.E./H.K.E.} = \frac{\omega^2 - f^2}{\omega^2 + f^2} \frac{\omega^2}{N_o^2 - \omega^2} \frac{\sum_n \frac{(2n+1)^{\frac{1}{2}-p}}{2^n\, n!} e^{-\eta^2} H_n^2(\eta)}{\sum_n \frac{e^{-\eta^2} [nH_{n-1}(\eta) - \frac{1}{2} H_{n+1}(\eta)]^2}{2^n n! (2n+1)^{\frac{1}{2}+p}}} \tag{1b}$$

These are energy ratios at a single depth; their behavior is considerably different than the ratios derived in the single turning-point model of Desaubies (1973). He used an exponential N(z) profile, finding the wave functions in terms of Airy functions. To calculate energy ratios he integrated over the last "lobe" of the Airy function (from the zero crossing nearest the turning point through it and beyond to a point where the functions reach an arbitrarily small value). Similar results are found from integration of the present model wave functions in the same fashion. These depth-integrated ratios are considerably different at frequencies near N(z) than the point expressions given in (1a,b). Fofonoff (1969) derived energy ratio expressions for a constant N, unbounded ocean, finding:

$$\text{P.E./H.K.E.} = \frac{N^2}{N^2 - \omega^2}\left(\frac{\omega^2 - f^2}{\omega^2 + f^2}\right); \quad N = \text{constant} \tag{2}$$

The (vertically averaged) ratio derived by Desaubies reduces to this result at low frequencies, where N(z) takes the place of N in Fofonoff's expression. This is the WKBJ limit; Desaubies averaged over half a wavelength vertically to calculate his result. By averaging over the whole water column using the thermocline modes, one finds the ratio is:

$$\text{P.E./H.K.E.} = \frac{N_o^2 + \omega^2}{N_o^2 - \omega^2}\left(\frac{\omega^2 - f^2}{\omega^2 + f^2}\right) \tag{3}$$

But this tells us little of what we expect to find at a given depth, even though it reduces to the expressions of Fofonoff and Desaubies at low frequencies. If a flat top and bottom in Fofonoff's constant N model are included, solutions are in terms of sines and cosines. The horizontal and vertical velocities for a given mode will be $\pi/2$ out of phase with depth. The energy ratios will be functions of depth and depend on which modes are energetic. Because Desaubies included boundary conditions in his model in order to compare his energy ratio calculations with Fofonoff's unbounded, constant N results, he chose to average vertically. He also used vertical averaging to obtain his ratio expressions near the turning point. Of course, a moored sensor is at a given depth; what is measured there is not a vertical average over half a wavelength for each mode. It responds to all modes together. Thus the ratios (1) vary considerably with depth, as would ratios for internal waves in a constant N ocean with boundary conditions imposed in

the vertical. The boundary conditions set up modes and energy ratios for modes must vary vertically. In an extreme case, if only even modes were energetic, the ratios (1) would be singular at z = 0. For any single mode, the ratios will be singular wherever vertical velocity reaches an extremum. Evidence of such singularities is not observed because more than one mode has finite energy. (Note that a traverse in depth may be mapped into a traverse in frequency in a turning point model, since the solutions are functions of z/μ.)

The maximum buoyancy frequency N_o is chosen from the Panulirus station profiles of $N(z)$ and $N^2(z)$ (Figure 3.1). This choice is a rough one since the Panulirus station is some 20 km further to sea than the MSA sites and the data were taken not contemporaneously with MSA experiments; they were gathered with bottles at widely spaced depths so as to give a coarse profile. Additionally, some Panulirus observations of salinity are of questionable accuracy, thus are omitted from calculation, further degrading the profiles. Surveys of Hogg (1972) and Wunsch (1972) indicate isotherm depths may change as much as 200 m in the main thermocline in response to large scale flows past Bermuda. The Panulirus station data show comparable variability in time, however the depth and shape of the main thermocline does not change drastically. A reasonable choice is N_o = 2.9 cph; this choice is within the hydrographic data variability and gives ratios at low frequencies ($\omega \ll N(z)$) which agree well with observed ratios (choice of N_o largely determines the ratio levels).

Only the ratio P.E./H.K.E. (1a) shall be discussed because it is familiar (Voorhis (1968)), the ratio V.K.E./H.K.E. is simply related to

it, and it is flat with frequency far from the turning point. Though V.K.E./H.K.E. can be computed without reference to the density field, its ω^2 dependence at low frequencies makes comparison of levels difficult. Only frequencies much greater than the inertial frequency are considered in this data, so this approximation is made in the model. (Rotation tagged along in the equations to this stage for generality.)

Model ratio calculations for P.E./H.K.E. are drawn in Figures 3.2a-c along with the observed ratio from the forward upper cluster in the second experiment. Each figure corresponds to a particular choice for the wavenumber spectrum and includes calculations made for the first 6, first 11, and first 21 modes n. A vertical line is drawn at the local buoyancy frequency $\bar{N}$ = 1.91 cph for the second experiment. Figure 3.2a shows P.E./H.K.E. for a flat spectrum in wavenumber (p=0). We see no evidence for the sharp peak just below $\bar{N}$ in the observed ratio. In Figure 3.2b, the energy spectrum varies inversely with vertical wavenumber (p=1) for the model ratios. The peak is not so accentuated, since high modes have less energy according to $(2n+1)^{-1}$. The level of the model ratio at low frequencies is a factor of 3 or so too high, though. In Figure 3.2c the spectrum varies as the inverse square wavenumber (p=2). Here the ratio is rather insensitive to the number of modes used. The level is lower than with p=1. We consider p=2 a reasonably good fit and we receive reinforcement in this choice from the Garrett and Munk (1975) spectrum, corresponding to p=2.5. The ratio computed for p=2.5 was nearly identical to the ratio in Figure 3.2c; the only major difference is that the small dip above $\bar{N}$ is

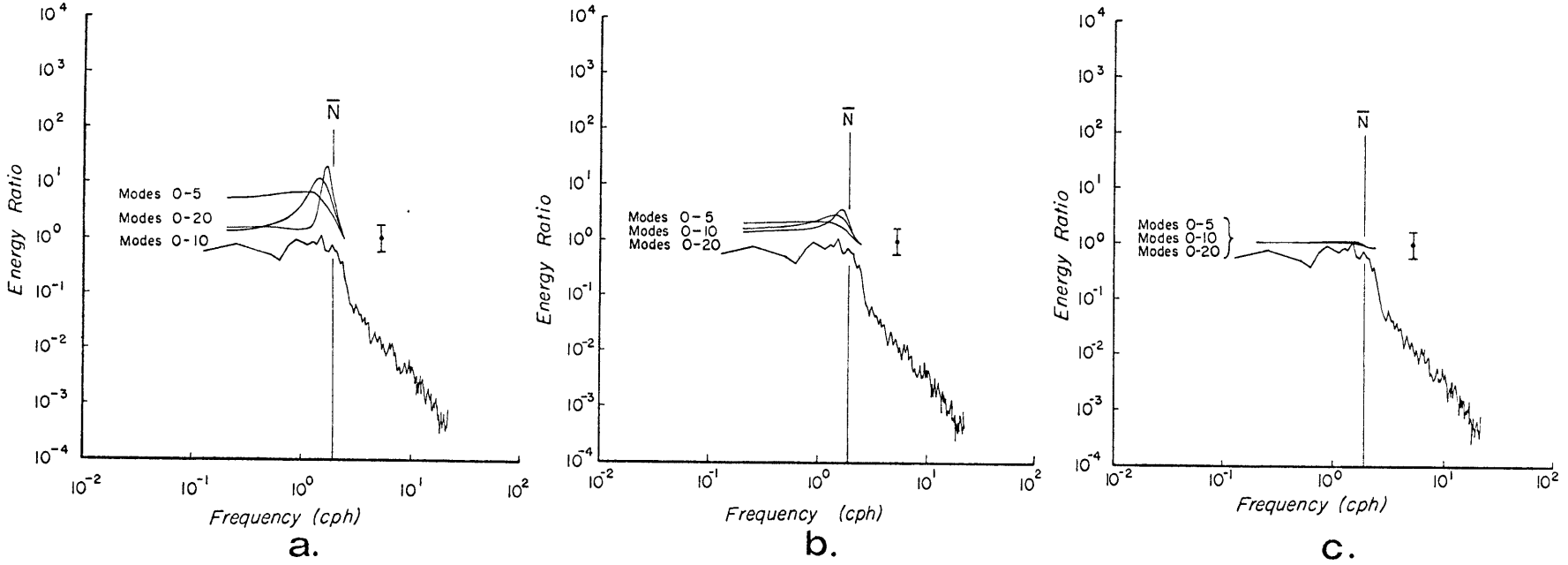


Figure 3.2. Model and observed ratios P.E./H.K.E. The observed ratio was computed from the forward upper cluster records in a 6-day segment of the second experiment. Averages are over 18 adjacent frequencies; error estimates for 95% confidence are at the right. Model curves use $E(\beta,\omega) = E(\omega/N_o)^{-2}(\beta/\beta_o)^{-p}$ where $p = 0,1,2$ in (a), (b), (c).

smaller. There is no reason to choose p=2.5 over p=2; in this comparison (and later ones) they are indistinguishable. As mentioned above, Cairns and Williams (1976) find p=2 a good fit. Also in reiteration, the presence of fine structure will cause the ratio level to be depressed in observations; a discussion of fine-structure contribution to horizontal velocity spectra is deferred until a later section. The sharp drop in the observed P.E./H.K.E. ratio just above the high frequency limit of our model (theoretically this limit is N_o, but in practice it is a bit less because of numerical considerations) corresponds to a sharp drop in the vertical velocity spectrum without an accompanying drop in the horizontal velocity spectrum. Beyond this sharp drop, P.E./H.K.E. falls off roughly as ω^{-2}. Corresponding to this steady fall, the ratio V.K.E./H.K.E. maintains a constant level of roughly one tenth. If the initial sharp drop of a decade is ascribed to fine-structure, one is led to the rough picture that non-internal wave-related horizontal kinetic energy is of the same order as vertical kinetic energy above the internal wave band. This qualitative picture is consistent with the widely discussed idea that motions above the internal wave band are (roughly) isotropically turbulent (Pochapsky (1972)).

The comparison between model and observed vertical velocity spectra can now be made with the shape of the energy spectrum $E(\beta,\omega)$ and the maximum buoyancy frequency N_o already indicated from the ratio comparisons. The frequency dependence of $E(\beta,\omega)$ is chosen by q=2, which works well and corresponds to the parameter chosen in earlier spectral fits (Garrett and Munk (1972a, 1975)). Figures 3.3a-c display model vertical velocity spectra for flat, inverse, and inverse square wavenumber spectra and the first 6, 11, and 21 modes. Different values of

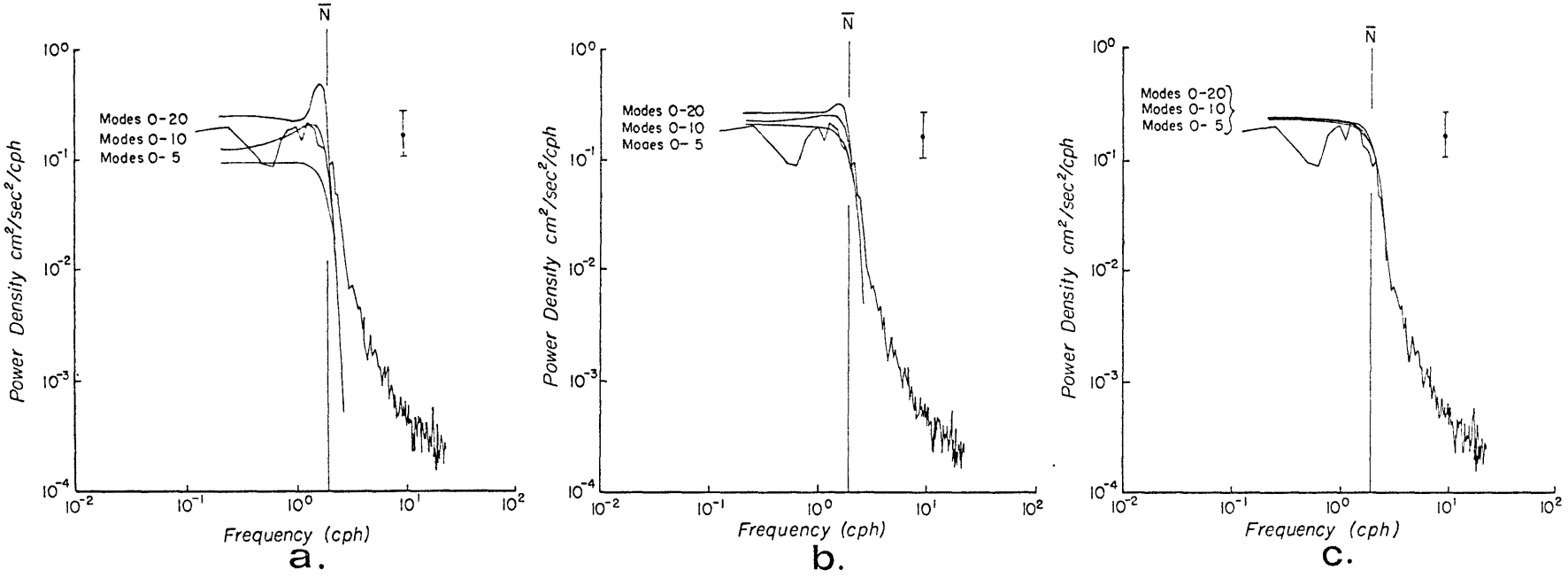


Figure 3.3. Model and observed spectra of vertical current. The observed spectrum was computed from the forward upper cluster record in a 6-day segement of the second experiment. Averages are over 18 adjacent frequencies; error estimates for 95% confidence are at the right. Model curves use $E(\beta,\omega) = 0.25(\omega/N_o)^{-2}(\beta/\beta_o)^{-p}$ cm^2/sec^2/cph where p = 0,1,2 in (a), (b), (c). Note the spectral well of about a factor of two centered at about 0.5 cph, believed to be related to the slope topography.

the level E are used according to wavenumber dependence so that the model curves approximate the observed spectra, one of which (forward upper from the second experiment) is plotted for reference. The curves for p=2 (Figure 3.3c) seem to fit adequately. Again, the shape of the spectrum when p=2 is rather insensitive to the number of modes used. Not only do the curves in Figure 3.2.2c show no evidence of a peak near $\overline{N}$ as the others do, but the shape of the drop-off above $\overline{N}$ is well imitated. Even with p=0, the dip in the observed vertical velocity spectrum at 0.5 cph is not described by the thermocline mode theory. This dip is at a frequency too low to be attributed to turning-point phenomena. Further, the waveguide described by the profiles of $N^2(z)$ in Figure 3.1 does not extend to frequencies lower than about 1 cph. An argument to describe this dip is provided below.

As mentioned above, the internal wave model proposed will not adequately describe the spectra of horizontal velocity and temperature due to the presence of fine-structure. For reference, the model spectra for these two variables are displayed in Figure 3.4a,b. These are the spectra moored sensors would detect in the absence of fine-structure; that is, with a constant gradient profile of temperature, constant buoyancy frequency, and lack of non-internal wave produced current fine-structure (to be discussed in Section 4.3). The observed spectra are also plotted. A dip at 0.5 cph of roughly an octave from an ω^{-2} spectrum appears only very roughly in both; it is probably obscured by the fine-structure contribution. In computing the model curves, the mean measured temperature gradient has been used, along with p=2, the six lowest modes, and E=0.25 $cm^2/sec^2/cph$. We shall retain these parameters in our models of fine-structure contribution to the spectra.

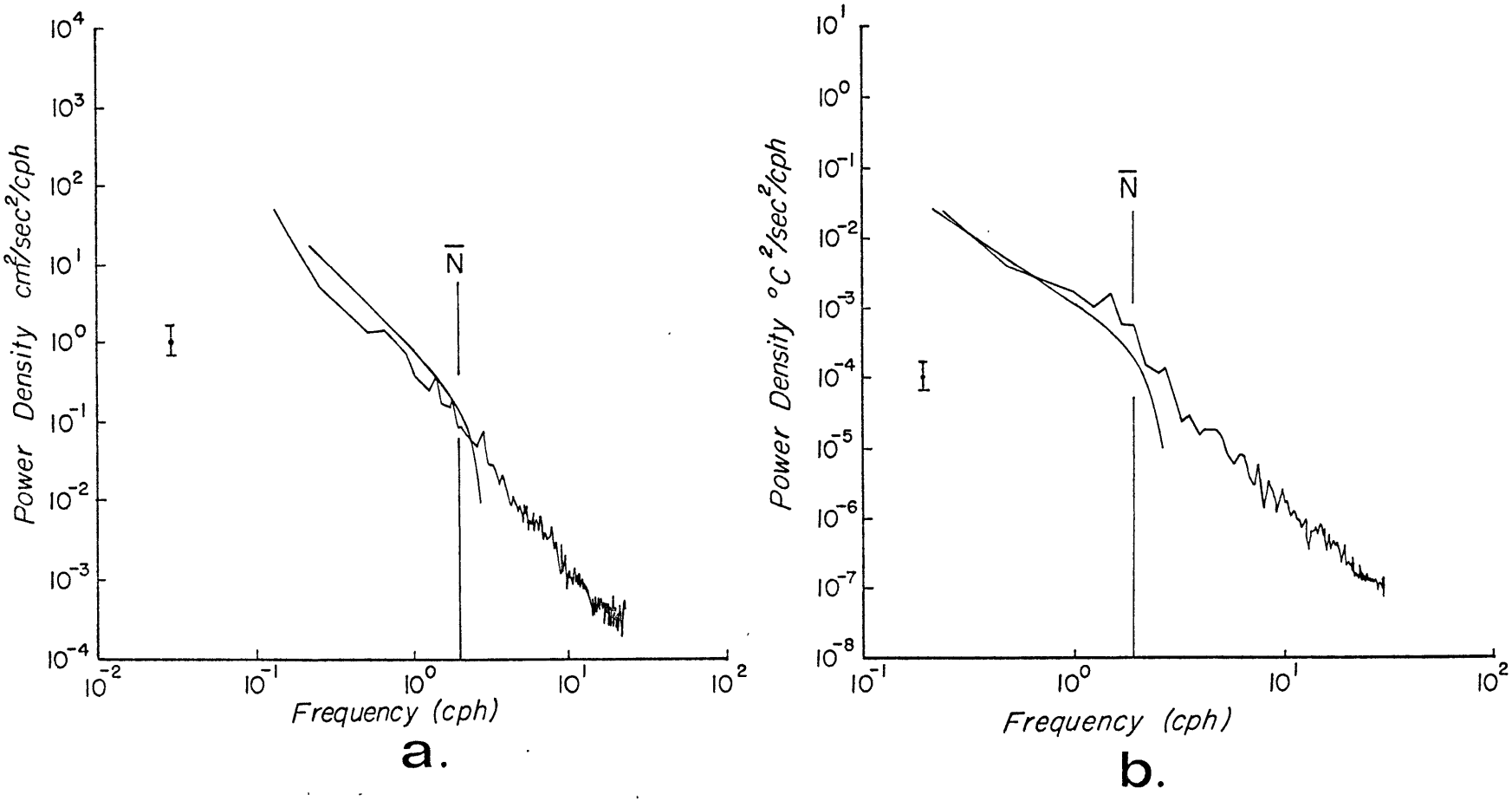


Figure 3.4. Mean-gradient model and observed spectra of (a) horizontal current and (b) temperature. The spectrum of UCOR was computed as in the previous two figures. The temperature spectrum was computed from a 3-day record in the second experiment. Averages are over 18 adjacent frequencies; error estimates for 95% confidence are at the left. Model curves use $E(\beta,\omega) = 0.25\ (\omega/N_o)^{-2}(\beta/\beta_o)^{-2}$ cm/sec/cph. The measured mean temperature gradient (T_z = 12.35 $\times 10^{-3}$ °C/m) was used in calculating the model temperature spectrum.

As noted above, a dip of roughly an octave centered at about 0.5 cph in the observed spectra from the second experiment is not explained by the thermocline mode theory. Instead, its existence seems related to the slope of Bermuda's topography. Figure 3.5 shows the bottom profile along a NW-SE transect passing within one kilometer of the second MSA experimental site. This transect is roughly perpendicular to the contours of bottom topography, thus represents the steepest bottom slopes. The position of the MSA and triangles indicating the local bottom slope at the anchor and at the depth of the instrument are drawn for reference. Recalling the stratification described in Figure 3.1, internal wave dispersion indicates that waves of frequency 0.5 cph would have propagation characteristics inclined roughly the same as the bottom slope at the mooring depth. At higher (lower) frequencies, characteristics along which energy propagates are more (less) steeply inclined. These correspond to transmissive (or "subcritical") and reflective (or "supercritical") frequencies in the terminology of Caccione and Wunsch (1974) with respect to a fixed bottom slope. They found that "critical" waves (waves whose characteristics are parallel to the bottom) in a two-dimensional laboratory experiment are heavily damped in a bottom boundary layer. Thus, it is suggested that the spectral dip observed is related to the local bottom slope. Perhaps the dip appears as the result of dissipation near the bottom; if the MSA were moored in the open ocean thermocline we would not expect to see the spectral dip. Assurance for this proposition may be found in the spectra from the third experiment. The mooring was set in a small region of basin-like topography embedded in the general island slope (see Figure 2.2). Lacking a bathymetric survey made specifically for this experiment, we are forced to rely on isolated soundings listed

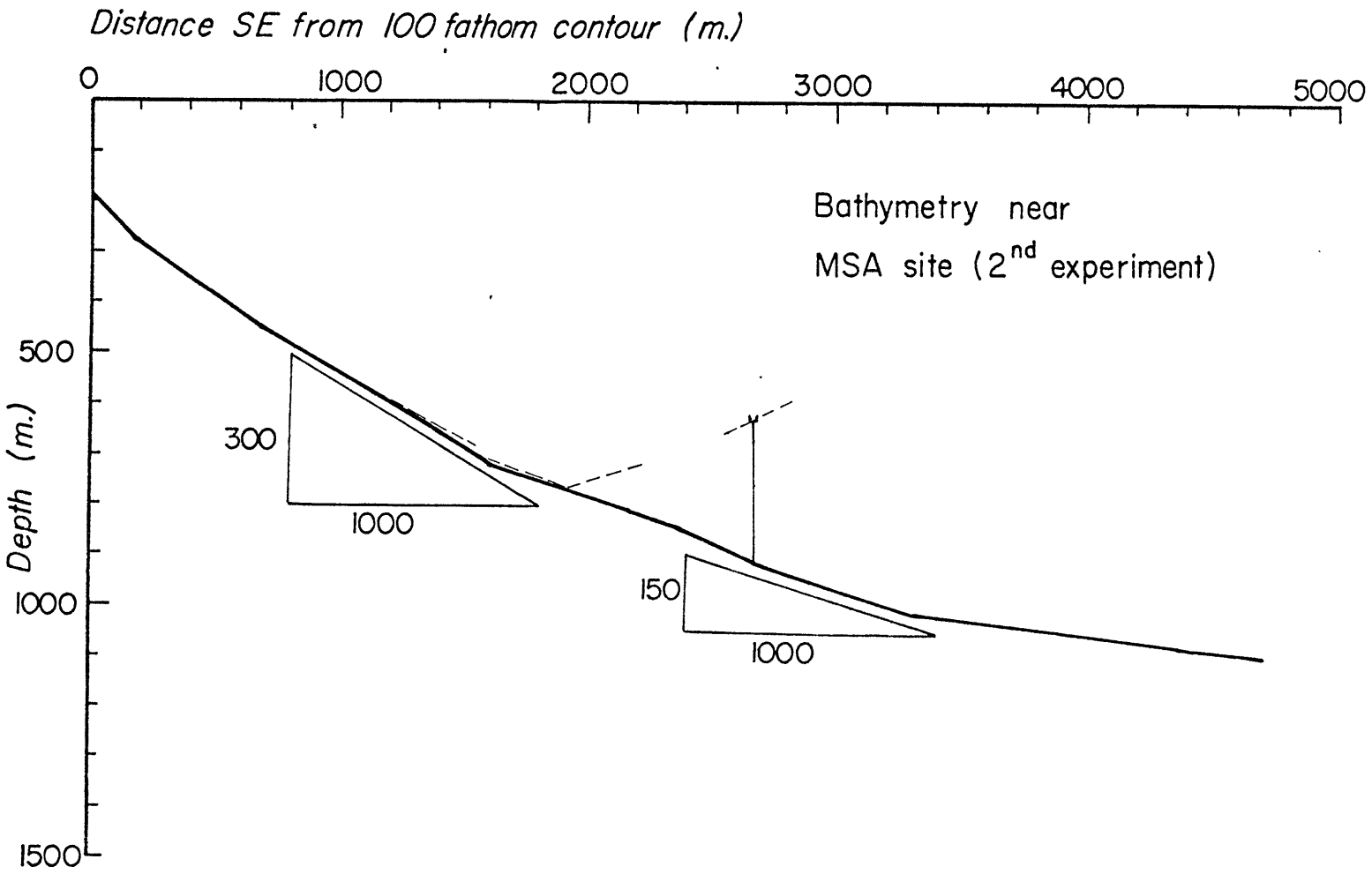


Figure 3.5. A bathymetric profile of the Bermuda slope near the site of the second experiment (see Figure 2.2). A schematic of the MSA along with approximate characteristics of internal waves at 0.5 cph are also drawn. Note that bottom slopes and characteristic slopes are nearly the same.

on the D.M.A. Hydrographic Center charts. Slopes taken from transects in this region can be steeper than those near the second experimental site by as much as a factor of two, or flatter, depending on the transect and bottom depth. In this confused picture of bottom topography, one expects to find a spectral dip which is more diffuse and extends to higher frequencies than the dip in the second experiment, which is exactly what is found in Figure 2.7, current spectra from the third experiment plotted to a different scale than in Figures 3.3a-c. Qualitatively, then, these spectral depressions are ascribed as possible interaction of internal waves with bottom topography, and the further discussion of them is avoided.

Discussion of various observed coherence measurements is deferred to a later section. The gross features of the internal wave spectrum at frequencies for which the thermocline waveguide is a valid approximation are well described by the theory proposed in the last section. A spectrum $E(\beta,\omega) = E(\beta/\beta_o)^{-2}(\omega/n_o)^{-2}$ where $E = 0.25$ cm^2/sec^2/cph seems a reasonable description of internal wave energy. Certainly a certain amount of "fine-tuning" could be pursued in the choice of parameters but that seems irrelevant to what has been established: that an appropriate physical model has been advanced to describe the observations in a limited frequency range. The important feature of this model over previous ones is that it adequately describes vertically long waves near N(z). Shorter waves have negligibly small energy, as seen in the insensitivity of the model curves to number of modes once a β^{-2} spectrum is chosen.

3.3 Horizontal isotropy of the wave field

The internal wave model developed in previous sections took advantage of our ability to separate vertical and horizontal variability so that only a one-dimensional problem was solved. Horizontal structure of the internal wave field has been referred to only through the dispersion relation; preference has been given to specification of frequency and vertical mode number. This model of horizontally propagating internal modes seems to have described many features of the data adequately, but the nature of horizontal variability has been sidestepped. In this section a brief discussion of this variability will be given. The major issue is that significant horizontal anisotropy of open ocean internal waves has not been established, yet coherence amplitudes of horizontally separated measurements are often quite high. In the conventional definition of coherence, a truly horizontally isotropic random field of waves would show low horizontal coherence and zero phase. Measurements from a deep trimooring in the Sargasso Sea (IWEX) show high horizontal coherences but no significantly non-zero phases. Briscoe (1975), in his preliminary report of this data, carefully points out that horizontal isotropy has not been unambiguously demonstrated from this data, but that the data are consistent with isotropy of a special kind. This is time-averaged isotropy. At any instant, the wave field near the sensors may be anisotropic; a wave packet in a particular direction dominates signals at horizontally removed instruments at any instant, but it propagates through the array and is followed by successive packets of different orientation throughout the experiment's duration. This situation, as will be demonstrated below, gives just the desired

high coherences with zero phase under the condition of a suitably red wavenumber spectrum.

Consider two sensors at positions x_1, x_2 encountering wave packets travelling with wavenumber k_n and phase ϕ_n at frequency ω_n:

$$f(x,t)_n = \Pi(c(t-b)) \cdot a_n e^{-i\omega_n t} e^{i(k_n x+\phi_n)} \tag{1}$$

Fourier transform the simple wave and its modulation Π separately. For simplicity, use a Gaussian shape for Π:

$$\Pi(c(t-b)) = e^{-\pi c^2 (t-b)^2} \tag{2}$$

Then the transformed packet $\hat{f}(\omega)$ is a convolution:

$$\hat{f}(x,s) = \frac{a_n}{c_n} e^{i(k_n x+\phi_n)} \int_{-\infty}^{\infty} ds' e^{-2\pi i b_n (s'-s) - \frac{\pi}{c_n^2}(s'-s)^2} \delta(s_n - s') \tag{3a}$$

$$= \frac{a_n}{c_n} e^{i(k_n x+\phi_n)} e^{-2\pi i b_n (s_n-s) - \frac{\pi}{c_N^2}(s_n-s)^2} \tag{3b}$$

where $s_n = \omega_n/2\pi$, $s = \omega/2\pi$. If many packets n are summed, an expression for the Fourier transform of the signal at each sensor is obtained:

$$\hat{f}_j(x_j,s) = \sum_n \frac{a_n}{c_n} e^{i(k_n x_j+\phi_n)} e^{-2\pi i b_n (s_n-s)} e^{-\frac{\pi}{c^2}(s_n-s)^2} \tag{4}$$

The cross power between $f_1(x_1,t)$ and $f_2(x_2,t)$ is:

$$\hat{f}_1(x_1,s)\hat{f}_2^*(x_2,s) = \sum_n \frac{a_n a_n^*}{c_n c_n} e^{ik_n D} e^{-\frac{2\pi}{c_n^2}(s_n-s)^2}$$

$$+ \sum_n \sum_{m>n} a_n a_m^* e^{i(k_n x_1 - k_m x_2 + \phi_n - \phi_m) - 2\pi i b_n (s_n - s) + 2\pi i b_m (s_m - s)}$$

$$\cdot e^{-\frac{\pi}{c_n^2}(s_n-s)^2} \cdot e^{-\frac{\pi}{c_m^2}(s_m-s)^2}$$

$$+ \text{c.c.} \qquad (5)$$

where $x_1 - x_2 = D$. In general we must assume the cross terms average to zero (waves of different packets are uncorrelated) so our estimate of coherence uses only the diagonal terms:

$$\text{coh}(f_1,f_2;s) = \frac{\hat{f}_1(x_1,s)\hat{f}_2^*(x_2,s)}{\sqrt{\hat{f}_1(x_1,s)\hat{f}_1^*(x_1,s)}\sqrt{\hat{f}_2(x_2,s)\hat{f}_2^*(x_2,s)}} \qquad (6a)$$

$$\simeq \frac{\sum_n \frac{a_n a_n^*}{c_n c_n} e^{ik_n D} e^{-\frac{2\pi}{c_n^2}(s_n-s)^2}}{\sum_n \frac{a_n a_n^*}{c_n c_n} e^{-\frac{2\pi}{c_n^2}(s_n-s)^2}} \qquad (6b)$$

Note that the form of the wave packet prescribes the smearing of component packets at frequencies s_n into the calculation of coherence at frequency s. Assuming this effect to be small, the amount of influence from neighboring frequencies s_n on s will depend on bandwidth c_n of the packets. The important result is that coherence phase is weighted by

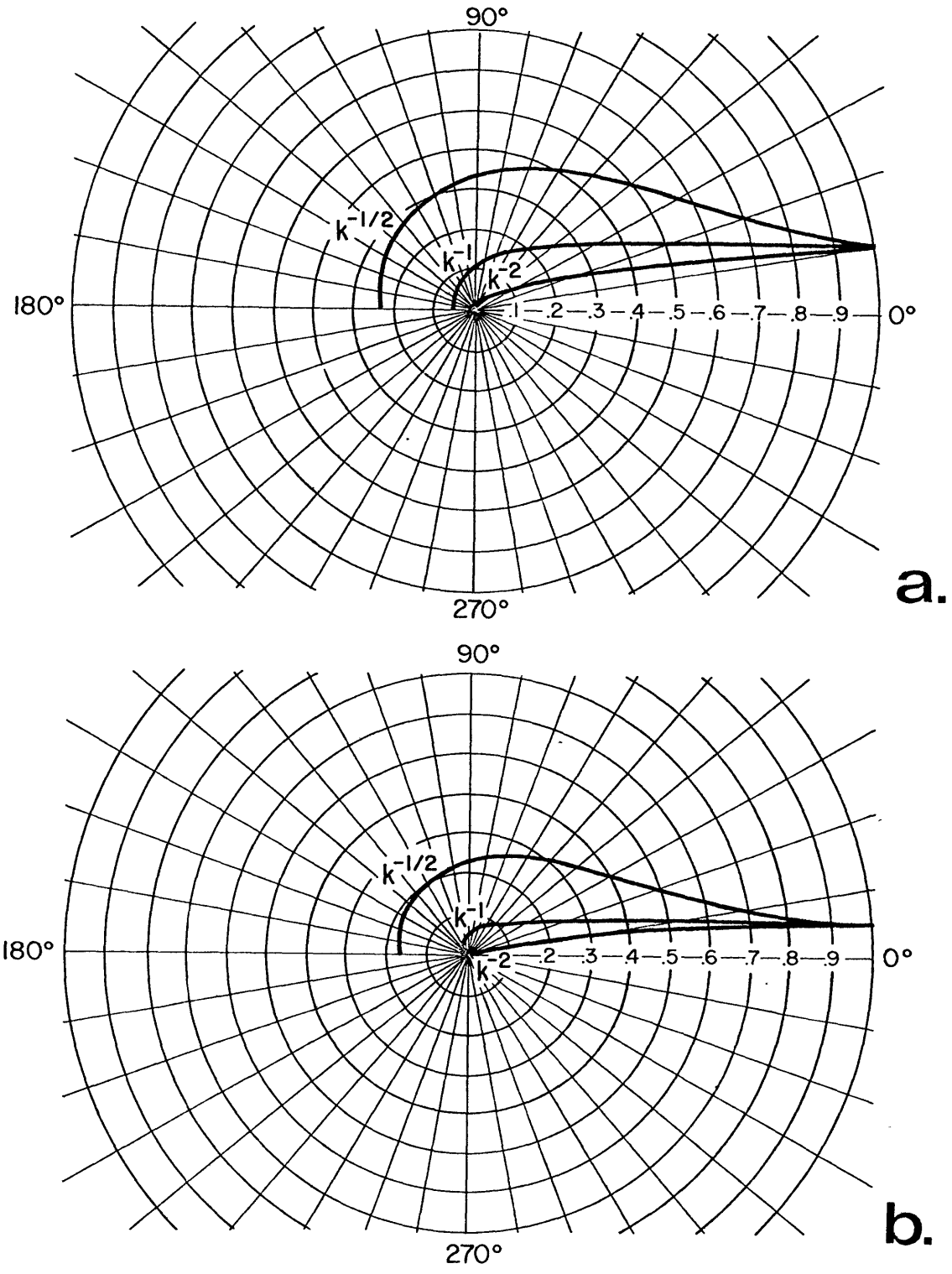


Figure 3.6. Polar plots of kD versus k^{-p} $(0 < k < 1)$ where D = 10° in (a), 5° in (b).

the most energetic packets. Imagine the numerator in (6b) to be a sum of vectors with magnitude $a_n a_n^*$ and phase $k_n D$, so that the total phase is determined by the largest vectors. Specifically, if $a_n a_n^*$ is a function of wavenumber (it is the unaveraged power spectrum), say, $a_n a_n^* \alpha\ k^{-p}$ (a red spectrum), then the smallest wavenumbers will contribute most heavily to the total phase of (6b). But small wavenumbers will also give small phases $k_n D$. Figures 3.6a,b are illustrations of this effect. If the lowest wavenumber k_o gives a phase $k_o D = \pi/36$ or $\pi/18$ (the two cases plotted) then the vectors added in the sum (6b) have tips on the curves and tails at the origin, depending on their wavenumber. Choice of p=2 (a reasonable choice, as has been discussed previously) allows contributions to the sum in the numerator of (6b) which will not have phase very different from $k_o D$.

Assuming packets are isotropically directed, waves whose wavenumber vectors are perpendicular to the line joining the two sensors (the x-axis) will have the lowest possible wavenumber in the x-direction: zero. If we imagine a modal structure for internal waves, there will be a lowest mode for each frequency, determining a lowest horizontal wavenumber through the dispersion relation. With a red wavenumber spectrum, these gravest waves will be the most energetic. The largest possible phase contribution to the sum is $k_o D$, the smallest is $-k_o D$. Many packets of these longest waves will make the total phase from (6b) tend to be less than $|k_o D|$. If D is short compared to $2\pi/k_o$, coherence magnitude will be nearly unity with phase nearly zero.

Since the MSA is an array oriented in a vertical plane, its resolution of horizontal wavenumber spectra is extremely limited. Its size is so small that long internal waves (they need only be 200 m or so long)

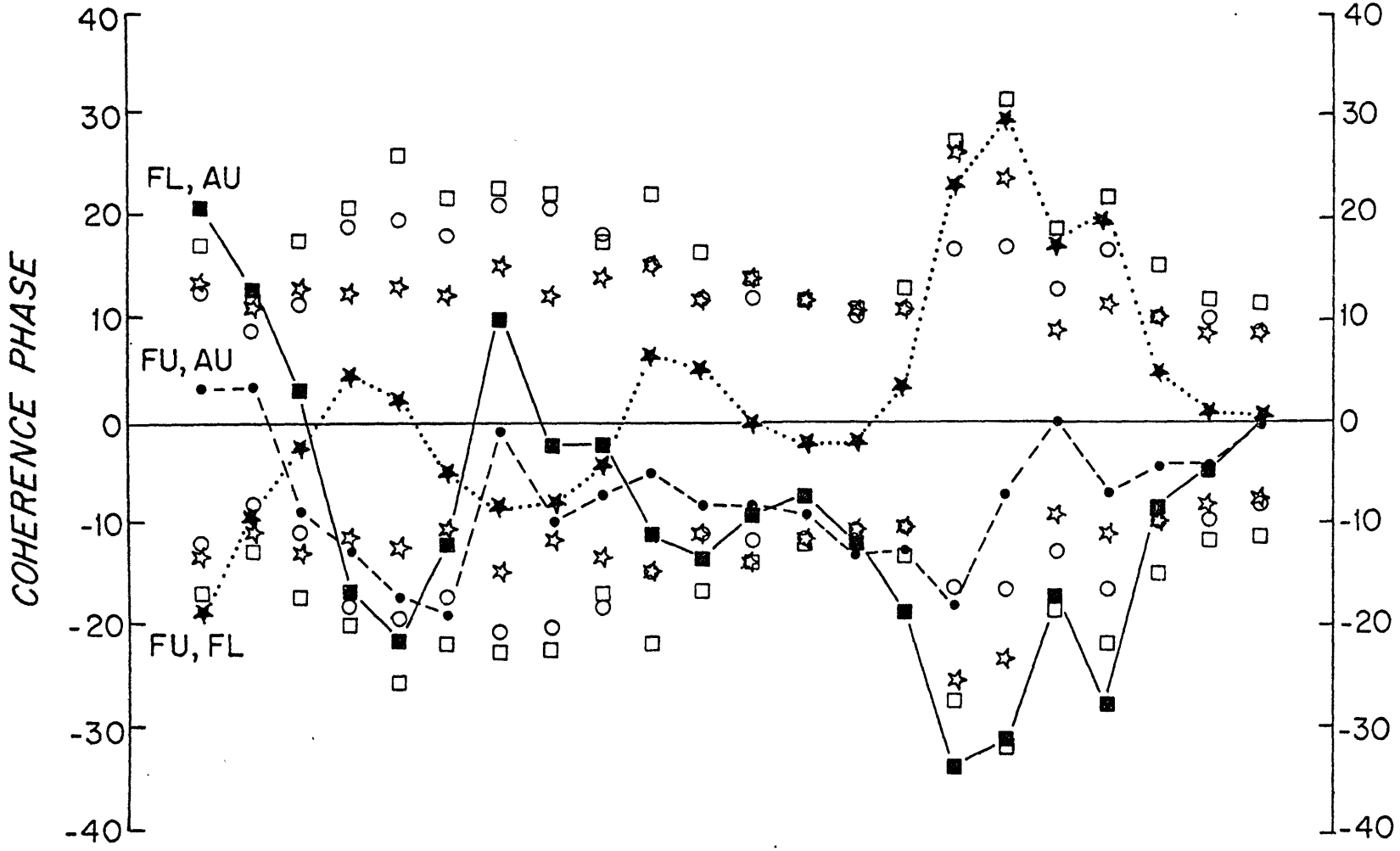


Figure 3.7. Coherence phase at 1.0 cph between vertical current at the three possible pairs of current meters. The 18-hour records used overlap each adjacent record by 6 hours. Line segments connect computed phases; error estimates for 95% confidence are plotted with similar symbols. Nine adjacent frequencies were averaged in computing phases in this plot.

will give negligibly small phase differences between fore and aft sensors. However, the high coherences between pairs of vertical velocity measurements on the MSA suggested investigation of the idea of time-averaged isotropy. Figure 3.7 shows the coherence phases at 1 cph for the three possible instrument pairs as a function of time for the second experiment. The records were broken up into 18-hour segments, each overlapping two adjoining segments by 6 hours each. Also indicated are 95% confidence limits $\Delta\phi$ for accepting the hypothesis of zero phase, computed from the formula:

$$\sin^2\Delta\phi = \frac{1-\gamma^2}{\gamma^2}\left((1-p)^{-1/N} - 1\right) \qquad (7)$$

of Goodman (1957) where γ is the true coherence, p is 0.95 and N is the number of band-averaged frequencies (nine). The computed phases exceed these limits no more frequently than the 95% confidence interval would indicate (only every third estimate is independent). Thus neither significant vertical nor horizontal phase differences have been detected. The situation is worse with the IIWA data since coherence amplitudes are lower, making confidence limits from (7) much broader. We are left to conclude that the field is consistent with time-averaged horizontal isotropy and that the model presented in this section is a plausible one for horizontal coherences of propagating internal waves.

Chapter 4. Internal Waves with Fine-Structure

4.1 Models of temperature fine-structure

We will develop a number of fine-structure models and demonstrate their implications for moored temperature measurements. Each of these models uses the conceptual framework of Garrett and Munk (1971) and the formal approach of McKean (1974). This framework is a quantitative description of the simplest conception of fine-structure alteration of the spectrum of temperature-inferred displacement from the true spectrum of vertical displacement. We imagine a vertical profile of temperature advected up and down past a moored sensor, concerning ourselves only with the purely kinematic effects of the passive profile on temperature measurements. "Passive" means that no dynamical effects are considered; irregularities in the temperature profile are effectively unchanged by (larger scale) internal wave motions and internal wave motions themselves are unresponsive to the irregularities. This is equivalent to assuming that rather long, energetic waves supported by the large scale density gradient provide most of the displacement variance. Internal waves of much shorter wavelength are considered unimportant because they have negligibly small energy by comparison. This is the assumption made in the thermocline mode model considered earlier, where only the first few modes were needed to describe the behavior of the directly-measured vertical current spectra and the spectral energy ratios (these are altered by the presence of fine-structure, of course). Garrett (1973) showed that wave strain could affect the fine structure vertical wavenumber spectrum, but that the wavenumber behavior of this additive correction was the same as that of the

basic fine-structure contribution itself. Thus effects of wave strain can be implicitly included in the fine-structure vertical wavenumber spectrum. Calculations of the relative size of the wave strain contribution from the internal wave model of Chapter 3 will be discussed at the end of the next section. By assuming known statistics of both internal wave displacements and fine-structure fluctuations of the temperature profile, the spectrum of temperature measured by a moored sensor can be calculated explicitly. The cross-spectrum of temperature measured at two vertically separated sensors can also be calculated, from which coherences and temperature difference spectra can be found.

Specifically (as McKean (1974)), we model the fine-structure of the advected medium $T_m(z)$ (the undisturbed profile) by its structure function $D_m(y) \equiv \langle (T_m(z) - T_m(z+y))^2 \rangle$. We shall consider a variety of models for which we imagine $T_m(z)$ to be constructed from a series of layers with temperature or one of its vertical derivatives held constant within each layer. These models shall be called "process-specified models." The thickness of each layer is modeled as a Poisson process; the structure function approach is appropriate since the mean-square difference (structure function) is well defined for a Poisson process. McKean (1974) pointed out this decided advantage over formulation in terms of the related autocovariance $R_m(y) = \langle T_m(z) T_m(z+y) \rangle$ which is formally divergent in such a case. Both $D_m(y)$ and $R_m(y)$ are intimately related to the vertical wavenumber spectrum $P_m(k)$ of $T_m(z)$. The identities relating the spectrum, the autocovariance, and the structure function for the lag t and circular frequency ω are:

$$D(t) = 2(R(0) - R(t)) \tag{1a}$$

$$D(t) = 2\int_{-\infty}^{\infty} \frac{d\omega}{2\pi}(1 - \cos\omega t)P(\omega) \tag{1b}$$

$$P(\omega) = \frac{1}{2\omega^2}\int_{-\infty}^{\infty} dt\ \cos\omega t\ \frac{d^2}{dt^2} D(t) \tag{1c}$$

Then either the structure function or the spectrum of $T_m(z)$ may be specified to achieve an equivalent result. We shall make such a specification for one of the fine-structure models even though we find specification of a process which gives a particular spectrum or structure function to be more satisfying. This model shall be referred to as a "wavenumber spectrum-specified model."

Formal description of the fine-structure contribution to moored frequency spectra is accomplished through an integral over the internal wave displacement probability distribution function $Q(\psi/\sqrt{2D_\zeta(\tau)})$ multiplied by the structure function of the advected medium $D_m(\psi)$ (McKean (1974)):

$$D_{fs}(\tau) = \int_{-\infty}^{\infty} d\psi D_m(\psi) Q(\psi/\sqrt{2D_\zeta(\tau)}) \tag{2}$$

where $\psi(\tau) = \zeta_1(t) - \zeta_2(t+\tau)$ is the displacement difference of the internal waves of lag τ, $D_{fs}(\tau)$ is the structure function of the fine-structure contribution, and $D_\zeta(\tau)$ is the structure function of the internal wave displacements. Note that Q is a parametric function of $D_\zeta(\tau)$ alone; for lack of a better choice, this simple form is used (see Briscoe (1976)). Q is chosen as a centrally peaked distribution

(which one is not crucial, as McKean points out); we will use the Gaussian and Laplace distributions.

To calculate cross spectra of temperatures measured at a vertical separation Y, the above development can be generalized. Now $\zeta_1(t,z)$ is the displacement at position z and $\zeta_2(t,z+Y)$ is measured at position z+Y. The structure function of displacements at locations separated by Y is $D_\zeta(\tau,Y) = \langle(\zeta_1(t,z) - \zeta_2(t+\tau,z+Y)^2\rangle$. The integral relation (2) becomes:

$$D_{fs}(\tau,Y) = \int_{-\infty}^{\infty} d\psi \; D_m(\psi) Q(\psi/\sqrt{2D_\zeta(\tau,Y)}) \tag{3}$$

where $\psi = \zeta_1(t,z) - \zeta_2(t+\tau,z+Y) + Y$. The relationships (1a-c) become:

$$D(t,Y) = 2(R(0,Y) - R(t,Y)) \tag{4a}$$

$$D(t,Y) = 2\int_{-\infty}^{\infty} \frac{d\omega}{2\pi} (1 - \cos \omega t) P_{12}(\omega) \tag{4b}$$

$$P_{12}(\omega) = \frac{1}{2\omega^2} \int_{-\infty}^{\infty} dt \cos(\omega t) \frac{d^2}{dt^2} D(t,Y) \tag{4c}$$

where $P_{12}(\omega)$ is the cross spectrum between measurements at z and z+Y. These reduce to (1a-c) for Y = 0. These are expressions used by McKean (1974). Different forms for $D_m(y)$ shall be developed for use in (3); with a simple Q, $D_{fs}(\tau,T)$ can be calculated explicitly as a function of $D_\zeta(\tau,Y)$. For $D_\zeta(\tau,Y)$ we will use the internal wave model developed in Chapter 3. Fourier transforms relating $D_\zeta(\tau,Y)$, $D_{fs}(\tau,Y)$ and $P_{\zeta_{12}}(\omega)$, $P_{fs_{12}}(\omega)$ are done numerically on a digital computer. We

will see that using explicit expressions for the internal wave spectra provides a significant improvement on McKean's work.

We consider two kinds of models for passive fine structure. The first describes fine structure as a series of Poisson-distributed layers each with homogeneous properties (i.e., specification of a process). The second simply specifies the form of the vertical wave-number spectrum of the medium.

The process-specified models we develop are extensions of the work of McKean (1974). McKean used a series of sheets and layers (layers of constant temperature separated by infinitesimal sheets) as in Phillips (1971); the layer thickness is distributed as a Poisson process:

$$P(N,s) = e^{-s} \frac{S^N}{N!}$$

is the probability of finding N layers in the distance y, where $s = y/\bar{h}$; $\bar{h}$ is the mean interval between the sheets (the mean layer thickness). The temperature difference over a distance y in this model is $T(y+z) - T(z) = \sum_{i=1}^{N} \theta_i$ where θ_i is the temperature jump from one layer to the next. This model can be extended by requiring instead that $\frac{d}{dz} T_m(z)$ be held constant in each layer and $T_m(z)$ be continuous from layer to layer. Then $T(y+z) - T(z) = \sum_{i=1}^{N} \theta_i + \theta'_{N+1}\Delta$, where θ'_{N+1} is the temperature gradient in the (N+1)st layer and $\Delta = y - \sum_{i=1}^{N} h_i$. A further extension is to consider an even smoother profile, one with $\frac{d^2}{dz^2} T_m(z)$ held constant in each layer and both $T_m(z)$ and $dT_m(z)/dt$ are continuous. Then $T(z+y) - T(z) = \sum_{i=1}^{N} \theta_i + \theta'_{N+1}\Delta + \theta''_{N+1} \frac{\Delta^2}{2}$, where θ'_{N+1} is now interpreted as $\frac{d}{dz} T_m(\sum_{i=1}^{N} h_i)$ and θ''_{N+1} is

the curvature of $T_m(z)$ in the (N+1)st layer. We will consider only the constant-curvature model, for the constant-gradient and sheet-layer models are readily derived from it.

Let us calculate the expected value of the temperature difference between two sensors separated vertically by y.

$$\overline{\langle T(z+y) - T(z) \rangle} = \left\langle \sum_{i=1}^{N} \theta_i + \theta'_{N+1}\Delta + \theta''_{N+1}\frac{\Delta^2}{2} \right\rangle, \quad (\bar{x} \equiv \frac{1}{N}\sum_{i=1}^{N} x_i)$$

The bars denote averaging over the layers, the brackets indicate an expected value with respect to the Poisson statistics of the layer thicknesses. If it is assumed that temperature jumps θ_i and layer thicknesses h_i are uncorrelated both with themselves and each other (a good approximation for hydrographic data interpreted according to the sheet-layer model; see Joyce and Desaubies (1976)), then:

$$\overline{T(z+y) - T(z)} = N\bar{\theta} + \overline{\theta'}(y - N\bar{h}) + \frac{\overline{\theta''}}{2}(y^2 - 2yN\bar{h} + N^2\overline{h^2}) \qquad (5)$$

The expected values of N, and N^2 with respect to the Poisson distribution are s, and s^2+s, respectively. Then the expected value of (5) is:

$$\overline{\langle T(z+y) - T(z) \rangle} = s(\bar{\theta} + \frac{\overline{\theta''}}{2}\overline{h^2}) \ . \qquad (6)$$

This mean temperature difference is the amount temperature would change due to an internal wave displacement y in a medium with temperature gradient $\frac{dT_m(z)}{dz} = (\bar{\theta} + \frac{\overline{\theta''}}{2}h^2)/\bar{h}$ for all z (i.e., no fine-structure).

Next we construct the mean square difference: the structure function $D_T(y) = \overline{\langle (T(y+z) - T(z))^2 \rangle}$. The squared difference is:

$$(T(y+z) - T(z))^2 = \left(\sum_{i=1}^{N} \theta_i\right)^2 + \theta'^2_{N+1} \Delta^2 + \frac{\theta''^2_{N+1}}{4} \Delta^4$$

$$+ 2 \sum_{i=1}^{N} \theta_i \theta'_{N+1} \Delta + \sum_{i=1}^{N} \theta_i \theta''_{N+1} \Delta^2$$

$$+ \theta'_{N+1} \theta''_{N+1} \Delta^3 .$$

Averaging with respect to the layers gives:

$$\overline{(T(y+z) - T(z))^2} = \overline{N\theta^2} + N(N-1)\bar{\theta}^2 + \overline{\theta'^2}\,\overline{\Delta^2} + \frac{\overline{\theta''^2}}{4}\overline{\Delta^4}$$

$$+ 2\bar{\theta}\,\overline{\theta'}\,\overline{N\Delta} + N\,\bar{\theta}\,\overline{\theta''}\,\overline{\Delta^2} + \overline{\theta'}\,\overline{\theta''}\,\overline{\Delta^3} \qquad (7)$$

Expressions for $\overline{\Delta^2}$, $\overline{\Delta^3}$, and $\overline{\Delta^4}$ are cumbersome, but easily derived. Note that $\langle N^3 \rangle = s^3 + 3s^2 + s$ and $\langle N^4 \rangle = s^4 + 6s^3 + 7s^2 + s$ for Poisson statistics. A bit of algebraic manipulation gives an expression for $D_T(y)$:

$$D_T(y) = s\{\overline{\theta^2} + \overline{\theta'^2}\,\overline{h^2} - 2\bar{\theta}\,\overline{\theta'}\,\overline{h} + \bar{\theta}\,\overline{\theta''}\,\overline{h^2} - \overline{\theta'}\,\overline{\theta''}\,\overline{h^3} + \frac{\overline{\theta''^2}}{4}\overline{h^4}\}$$

$$+ s^2\{\bar{\theta}^2 + \bar{\theta}\,\overline{\theta''}\,\overline{h^2} + \frac{\overline{\theta''^2}}{4}\overline{h^2}^2\} + s^2\{\overline{3\theta''^2} - \overline{\theta''^2})\,(\overline{h^2}/2)^2\} \qquad (8)$$

The middle term is easily recognized as $(\overline{\langle T(y+z) - T(z) \rangle})^2$, the contribution from the mean gradient. The fine structure contribution $D_{fs}(\tau, Y)$

comes from the first and third terms of $D_T(y)$. In terms of our model (3), we find

$$D_m(y) = \{\overline{\theta^2} + \overline{\theta'^2}\,\overline{h^2} - 2\overline{\theta}\,\overline{\theta'}\,\overline{h} + \overline{\theta}\,\overline{\theta''}\,\overline{h^2} - \overline{\theta'}\,\overline{\theta''}\,\overline{h^3} + \frac{\overline{\theta''^2}}{4}\,\overline{h^4}\}(y/\overline{h})$$

$$+ \{(3\overline{\theta''^2} - \overline{\theta''}^2)(\overline{h^2}/2)^2\}(y/\overline{h})^2 \qquad (9)$$

$$= Ay + By^2.$$

For the purposes of calculating $D_{fs}(\tau,Y)$ from $D_m(y)$ (i.e., integrating over ψ in (3)), the terms in brackets may be considered as positive definite constants.

If we choose the internal wave displacement distribution simply, we can carry out the integral (3). We choose a Gaussian:

$$Q(\tau,Y;\psi) = \frac{\exp(-\psi^2/2D_\zeta(\tau,Y))}{\sqrt{2\pi D_\zeta(\tau,Y)}} \qquad (10)$$

So that our expression for $D_{fs}(\tau,Y)$ from (3) is:

$$D_{fs}(\tau,Y) = A\int_{-\infty}^{\infty}|\psi+Y|Q(\tau,Y;\psi)d\psi + B\int_{-\infty}^{\infty}(\psi+Y)^2Q(\tau,Y;\psi)d\psi \qquad (11)$$

where we have interpreted y in terms of the internal wave displacement difference ψ plus the vertical sensor separation $y \to \zeta_1 - \zeta_2 + Y$. Doing the integration:

$$D_{fs}(\tau,Y) = A\,Y\,\mathrm{erf}\,\frac{Y}{\sqrt{2D_\zeta(\tau,Y)}} + \sqrt{\frac{2D_\zeta(\tau,Y)}{\pi}}\exp\left(\frac{-Y^2}{2D_\zeta(\tau,Y)}\right)$$

$$+B[D_\zeta(\tau,Y) + Y^2] \qquad (12a)$$

When Y = 0, this reduces to

$$D_{fs}(\tau,0) = A\sqrt{\frac{2D_\zeta(\tau,0)}{\pi}} + B\, D_\zeta(\tau,0) \quad . \tag{12b}$$

For the sheet-layer model $A = \overline{\theta^2}$ and B = 0, so that the contribution to fine structure is proportional to the square root of the internal wave displacements for $Y \to 0$ and is constant for $Y/\sqrt{2D_\zeta(\tau,Y)} \gg 1$. The situation is the same for the constant gradient model, but A is somewhat smaller, reflecting the relative smoothness of the constant-gradient model over the sheet-layer model. In the constant curvature Model A and B are both non-zero; here, part of the fine-structure contribution has a form identical to the internal wave contribution. This is a dismaying prospect. It means that a temperature spectrum will be augmented at all frequencies by some fraction of the internal wave displacement spectrum in addition to the mean-gradient contribution. Note these three models use different interpretations of θ_i, θ_i', θ_i'', and h_i. Joyce and Desaubies (1976) computed θ_i and h_i for the sheet-layer model from hydrographic stations made in the Sargasso Sea during IWEX; computation of θ_i' or θ_i'' from data for the two smoother models is probably beyond the reach of the instrumentation used, a Brown-W.H.O.I. CTD (Joyce, private communication).

McKean derived the asymptotic behavior (for high and low frequency) of the fine-structure spectrum $F(\omega)$ and the coherence $C_{fs}(\omega) = F_{12}(\omega)/\sqrt{F_{11}(\omega)F_{22}(\omega)}$ for the sheet-layer model. Behavior is the same for the constant-gradient model and the first term in (12) of the constant-curvature model. The fine structure cross spectrum is real

(i.e., its quadrature spectrum is zero) in these models, since $D_{fs}(\tau,Y)$ is an even function of τ. The temperature difference spectrum can also be computed from the autocovariance of the difference over a vertical separation Y.

$$R_{\Delta T}(\tau,Y) = \langle (T(t,z+Y) - T(t,z))(T(t+\tau,z+Y) - T(t+\tau,z)) \rangle$$

$$R_{\Delta T}(\tau,Y) = R_{11}(\tau,0) + R_{22}(\tau,0) - R_{12}(\tau,Y) - R_{21}(\tau,Y). \tag{13}$$

Fourier transforming, we obtain the cospectrum from the last two terms:

$$F_{\Delta T}(\omega) = F_{11}(\omega) + F_{22}(\omega) - 2F_{12}(\omega) \ . \tag{14}$$

If the displacements at the two locations are perfectly coherent, the fine-structure temperature difference spectrum is in terms of the coherence $C_{fs}(\omega)$:

$$F_{\Delta T}(\omega) = 2F(\omega)(1 - C_{fs}(\omega)). \tag{15}$$

To obtain the asymptotic behavior of $F(\omega)$ and $C_{fs}(\omega)$, we take the internal wave spectrum to be $P(\omega) = A\omega^{-2}$; $f < \omega < N$ (the traditional crude approximation). McKean finds

$$F(\omega) \simeq \begin{cases} \frac{1}{2}\frac{\overline{\theta^2}}{h} A^{1/2}\omega^{-3/2} & \omega << N \\ \frac{\sqrt{2}}{\pi}\frac{\overline{\theta^2}}{h} A^{1/2}N^{1/2}\omega^{-2} & \omega >> N \end{cases} \tag{16}$$

He further computes expressions for $C_{fs}(\omega)$. We use his expressions to find $F_{\Delta T}(\omega)$ (as did Joyce and Desaubies (1976)):

$$F_{\Delta T}(\omega) \simeq \begin{cases} \frac{1}{2}\frac{\overline{\theta^2}}{\overline{h}} Y^2 A^{-3/2} \omega^{-1/2} & \omega << N \\ \frac{\sqrt{2}}{\pi}\frac{\overline{\theta^2}}{\overline{h}} A^{1/2} N^{1/2} \omega^{-2} \left(1-2\int_o^\infty u^{-3} e^{-u} \cos u\lambda \, du\right) & \omega >> N \end{cases} \tag{17}$$

$$\text{where } \lambda = \omega Y \Big/ \sqrt{\frac{2AN}{\pi}} \ .$$

We will recognize the asymptotic behavior of these quantities when they are numerically computed and plotted in the next section. As McKean (1974) pointed out, the high frequency limit is the limit for which internal wave fluctuations seem very slow so that vertical current is effectively constant for small lags. In the low frequency limit, the cutoff at N appears at such a high frequency that it can effectively be ignored.

We find in the next section that the behavior of the layer model fine structure spectra at high frequencies is inadequate. The observed spectra behave more as $\omega^{-5/2}$ than ω^{-2}, so we consider a model which gives such high frequency behavior. Measurements in the Sargasso Sea indicate that vertical wavenumber spectra behave roughly as k^{-2} or $k^{-2.5}$. Our process-specified models correspond to k^{-2} and k^{-3} (see (18) below) so we shall consider a model with an undisturbed profile whose spectrum is specified as $P_T(k) = A_T k^{-2.5}$. Since

$$\frac{t^{q-1}}{\Gamma(q)\sin(\frac{\pi}{2}(q-1))} = 2\int_{-\infty}^{\infty}\frac{d\omega}{2\pi}(1-\cos\omega t)|\omega|^{-q};\quad 1<q<3 \tag{18}$$

(McKean (1974), or use the substitution $\sin^2(\frac{\omega f}{2}) = 1-\cos\omega t$ and formula 333-19c of Gröbner and Hofreiter (1966)), the structure function for the medium is (with $q = 5/2$):

$$D_m(y) = \frac{A_T y^{q-1}}{\Gamma(q)\sin(\frac{\pi}{2}(q-1))} = \frac{A_T y^{3/2}}{\Gamma(5/2)\sin(\frac{3\pi}{4})} \tag{19}$$

Then, as before, we interpret y to be the sum of the sensor separation and the internal wave difference in (3). We obtain:

$$D_{fs}(\tau,Y) = \frac{A_T}{\Gamma(5/2)\sin(\frac{3\pi}{4})}\int_{-\infty}^{\infty}d\psi|\psi+Y|^{3/2}Q(\tau,Y;\psi) \tag{20}$$

To facilitate integration, we choose $Q(\tau,Y;\psi)$ to be the Laplace (double exponential) distribution (Abramowitz and Stegun (1964)):

$$Q(\tau,Y;\psi) = \frac{\exp(-|\psi|/\sqrt{2D_\zeta(\tau,Y)})}{2\sqrt{2D_\zeta(\tau,Y)}} \tag{21}$$

Then (20) becomes, using $A_T' = A_T(\Gamma(5/2)\sin(\frac{3\pi}{4}))^{-1}$;

$$D_{fs}(\tau,Y) = \frac{A_T'}{2\sqrt{2D_\zeta(\tau,Y)}}\int_{-\infty}^{\infty}d\psi|\psi+Y|^{3/2}\,d^{-|\psi|\sqrt{2D_\zeta(\tau,Y)}} \tag{22}$$

The integration yields an expression in terms of incomplete Gamma functions $\gamma(5/2,x)$ (use Gradshteyn and Ryzhik (1965) formula 3.382-1, 3.382-2, and 3.382-4; the functions $\gamma(5/2,x)$ are discussed in Abramowitz and Stegun (1964)).

$$D_{fs}(\tau,Y) = A_T'(\sqrt{2D_\zeta(\tau,Y)})^{3/2}[\Gamma(5/2)\sinh x + \frac{e^{-x}}{2}\gamma(5/2,-x) - \frac{e^{x}}{2}\gamma(5/2,x)] \tag{23}$$

where $x = Y/\sqrt{2D_\zeta(\tau,Y)}$.

In the limit of small separations ($x \to 0$) we find

$$D_{fs}(\tau,Y) = A_T'\Gamma(5/2)(\sqrt{2D_\zeta(\tau,Y)})^{3/2} \tag{24}$$

For small lags $D_\zeta(\tau,Y) \to 0$ ($x \to \infty$) so that we find

$$D_{fs}(\tau,Y) = A_T'Y^{3/2}. \tag{25}$$

As before, we wish to calculate the asymptotic behavior of $F(\omega)$ and $F_{\Delta T}(\omega)$. We need to calculate the behavior of $D_\zeta(\tau,Y)$ for small and large lags (corresponding to the internal wave spectrum dependence at high and low frequencies). To find the former, we approximate the cosine by its power series; to lowest order we find

$$D_\zeta(\tau,T) \simeq \int_{-N}^{N} (\omega\tau)^2 A|\omega|^{-q}\frac{d\omega}{2\pi} \tag{26}$$

If $q = 2$ (our crude internal wave spectrum approximation) we obtain:

$$D_\zeta(\tau,Y) = \tau^2\frac{AN}{\pi} \qquad (\frac{\omega}{N} >> 1) . \tag{27}$$

In the low frequency limit we are able to use (18) (i.e., ω is much less than the cutoff of the spectrum N):

$$D_\zeta(\tau,Y) = A\tau \qquad (\frac{\omega}{N} << 1). \tag{28}$$

Having obtained expressions for the internal wave structure function at high and low frequencies, we can proceed to calculate $D_{fs}(\tau,Y)$ in these limits. At high frequencies $D_{fs}(\tau,Y)$ behaves as (24) for $Y = 0$ and as (25) for $Y \neq 0$. For $Y = 0$, we find:

$$D_{fs}(\tau,0) = A_T'\Gamma(5/2)\,(\frac{2AN}{\pi})^{3/2}\tau^{3/2} \quad . \tag{29}$$

Using (18) we calculate the fine structure spectrum:

$$F(\omega) = A_T'^2\Gamma^2(5/2)\,(\frac{2AN}{\pi})^{3/2}\sin(\frac{3\pi}{4})\omega^{-5/2} \quad . \tag{30}$$

Since the Fourier transform of (25) is a delta function at $\omega = 0$, we find $F_{\Delta T}(\omega) = F_1(\omega) + F_2(\omega)$, so:

$$F_{\Delta T}(\omega) = A_T'^2\Gamma^2(5/2)\,(A_1^{3/2} + A_2^{3/2})\,(\frac{2N}{\pi})^{3/2}\,\sin\frac{3\pi}{4}\,\omega^{-5/2}. \tag{31}$$

At low frequencies we take the limit of large lags, or $x \to 0$ in (23). Abramowitz and Stegun (1964) give expressions for $\gamma(5/2,x)$ and $\gamma(5/2,-x)$ as series. If we expand $\sinh(x)$ as well, we find the lowest order terms in the expression in brackets in (23) come from $\sinh(x) = 1 + \frac{x^2}{2}$ + h.o.t. So for large lags the structure function is:

$$D_{fs}(\tau,Y) \simeq A_T'\Gamma(5/2)\,(\sqrt{2D_\zeta(\tau,Y)})^{3/2} \quad (1 + \frac{x^2}{2}) \tag{32}$$

Our expressions for $D_{fs}(\tau,Y)$, substituting (28), are:

$$D_{fs}(\tau,0) = A_T'\Gamma(5/2)2^{3/4}A^{3/4}\tau^{3/4} \qquad (33a)$$

$$(\omega/N << 1)$$

$$D_{fs}(\tau,Y) = A_T'\Gamma(5/2)2^{3/4}A_{12}^{3/4}(\tau^{3/4} + \frac{Y^2}{4A_{12}}\tau^{-1/4}) \qquad (33b)$$

We transform (33a) using (18) to find

$$F(\omega) = A_T'\Gamma(5/2)2^{3/4}A^{3/4}\sin\frac{3\pi}{8}\Gamma(7/4)\omega^{-7/4} \qquad \frac{\omega}{N} << 1 \qquad (34)$$

If we assume perfect displacement coherence, we have $A = A_{12}$, so the temperature difference structure function is:

$$\begin{aligned} D_{fs}\Delta T(\tau,Y) &= D_{fs11}(\tau,0) + D_{fs22}(\tau,0) - 2D_{fs12}(\tau,Y) \\ &= -A_T'\Gamma(5/2)2^{3/4}A^{-1/4}\frac{Y^2}{2}\tau^{-1/4} \end{aligned} \qquad (35)$$

We use (4c) to transform this expression:

$$\begin{aligned} F_{\Delta T}(\omega) &= \frac{1}{2\omega^2}\int_{-\infty}^{\infty} dt\ \cos\omega t(-A_T'\Gamma(5/2)2^{-1/4}A^{-1/4}Y^2\frac{5}{16}\tau^{-9/4}) \\ &= \omega^{-3/4}(-A_T'\Gamma(5/2)2^{3/4}\frac{5}{32}A^{-1/4}Y^2\lim_{u\to o}\int_u^{\infty} x^{-9/4}\cos x\,dx) \end{aligned} \qquad (36)$$

We use Gradshteyn and Ryzhik (1965), formula 3.761-7 to find:

$$\lim_{u\to o}\int_u^\infty x^{-9/4}\cos x\,dx = \cos\frac{5\pi}{8}\,\frac{16}{5}\,\Gamma(3/4)\,. \qquad (37)$$

This leaves us with:

$$F_{\Delta T}(\omega) = A_T'\Gamma(5/2)\,2^{-1/4}A^{-1/4}\gamma^2\cos(\tfrac{3\pi}{8})\,\Gamma(\tfrac{3}{4})\,\omega^{-3/4} \qquad \omega/N << 1 \qquad (38)$$

We are now ready to procede to comparisons of these fine-structure models for temperature with observations, which will be done in the next section. The models developed in this section generalize the sheet-layer models used by others (Phillips (1971), Garrett and Munk (1971), McKean (1974), and Joyce and Desaubies (1976)). The sheet-layer model is a process-specified model; its generalization is a model with layers of constant gradient or constant curvature. Our expressions show that the sheet-layer and constant-gradient models are equivalent to a vertical wavenumber spectrum-specified model with spectral slope k^{-2}. The constant curvature model is equivalent to a k^{-3} spectrum-specified model. These were developed in the hope that a process-specified model could describe a passive fine-structure field. As we shall see next, the particular process-specified models presented are inconsistent with measured frequency spectra, which is why a spectrum-specified model was also developed. The next section will show this model provides a self-consistent description of fine-structure as a passive vertical field.

4.2 Comparisons with temperature data

Now that we have developed a model that seems to describe the salient features of the internal wave field, we are ready to use it in conjunction with the expressions for passive fine-structure effects

derived in the previous section to describe moored temperature spectra. To make the comparisons between models and observations, three spectral quantities are useful. The most basic is the moored temperature spectrum. The other two are generalizations of this; they are the coherence and the temperature difference spectrum (the finite first difference of temperatures measured at two vertically separate positions), which involve estimates of cross spectra over some vertical separation. It will become evident that when one of the model spectral quantities imitates the observations well, the other two also do. This is to be expected, since no additional model assumptions are made in calculating the higher order spectral quantities beyond the simple model temperature spectrum. However, calculation of all three quantities is useful because each is sensitive to a different combination of model parameters (e.g., internal wave spectrum shape and number of modes). The process-specified models will be considered first; recognizing their inadequacies, we will go on to consider the wavenumber spectrum-specified model.

So far, we have considered internal wave (mean-gradient) and fine-structure coherences and difference spectra separately. The observed spectra will reflect contributions from both model sources. Our partition of moored signals into a mean gradient contribution and a fine-structure contirbution is somewhat arbitrary and artificial; here we shall combine them for comparison with observations. The total temperature difference spectrum $P_{\Delta T}(\omega)$ is derived analogously to (4.1.13) and (4.1.14), but contains terms from both mean-gradient and fine-structure. It is:

$$P_{\Delta T}(\omega) = P_{11}(\omega) + P_{22}(\omega) - 2P_{12}(\omega) + F_{11}(\omega) + F_{22}(\omega) - 2F_{12}(\omega) \tag{1}$$

Similarly, the temperature coherence is:

$$C(\omega) = \frac{P_{12}(\omega) + F_{12}(\omega)}{(P_{11}(\omega) + F_{11}(\omega))^{1/2}(P_{22}(\omega) + F_{22}(\omega))^{1/2}} \tag{2}$$

As noted earlier, the fine-structure cross spectrum $F_{12}(\omega)$ is real, just as is $P_{12}(\omega)$ (see 3.1.22b), so the coherence phase will be 0 or π. Earlier investigators have lacked knowledge of internal wave auto- and cross-spectra so that simplified versions of (1) and (2) were necessary. In order to allow changes in the internal wave coherence to be included in their models, Garrett and Munk (1971), McKean (1974), and Joyce and Desaubies (1976) all assumed $F_{11}(\omega)/P_{11}(\omega) = F_{22}(\omega)/P_{22}(\omega)$. With this assumption, (2) becomes:

$$C(\omega) = \frac{P_{12}(\omega) + F_{12}(\omega)}{P_{11}(\omega) + F_{11}(\omega)} \tag{3a}$$

$$= \frac{\frac{P_{12}(\omega)}{P_{11}(\omega)} + \frac{F_{11}(\omega)}{P_{11}(\omega)}\frac{F_{12}(\omega)}{F_{11}(\omega)}}{1 + \frac{F_{11}(\omega)}{P_{11}(\omega)}} \tag{3b}$$

$$= \frac{C_{\zeta}(\omega) + C_{fs}(\omega)\gamma(\omega)}{1 + \gamma(\omega)} \tag{3c}$$

where $C_\zeta(\omega)$ and $C_{fs}(\omega)$ are the internal wave and fine-structure coherences and $\gamma(\omega) = F_{ii}(\omega)/P_{ii}(\omega)$ is called the fine-structure ratio. This expression will necessarily underestimate (overestimate) the observed coherence if $P_{11}(\omega)$ is actually greater (less) than $P_{22}(\omega)$, more seriously for larger separations than for smaller ones. Our internal wave model predicts substantial changes in internal wave displacement power density with depth, especially across the turning point at a given frequency. We are forced to use the more general (but correct) expressions (1) and (2) because of this strong variation.

In addition to the internal wave parameters chosen earlier, the constants A, B, and A_T' in equations (4.1.9) and (4.1.23) must be specified. These constants represent the intensity of the layering. The size of these constants relative to the internal wave spectral level E determines at what frequency the fine-structure ratio $\gamma(\omega)$ will pass through unity, producing a sort of "break point" in spectral slopes. The depths of both sensors relative to the center of the thermocline $z = 0$ must also be specified in order to compute cross spectra of displacement and the accompanying fine-structure cross spectra. Equivalently, we specify the position z of the lower sensor and the sensor separation Y. Given the buoyancy frequency at the lower sensor, the parabolic profile of $N^2(z)$ then determines $N(z+Y)$, the buoyancy frequency at the upper sensor. We consult the Panulirus profiles (Figure 3.1) for guidance in choosing the position z. Since these profiles are crude and temporally variable (also spatially variable, as indicated in measurements of Hogg (1972) and Wunsch (1972)), some arbitrariness is involved in choosing z.

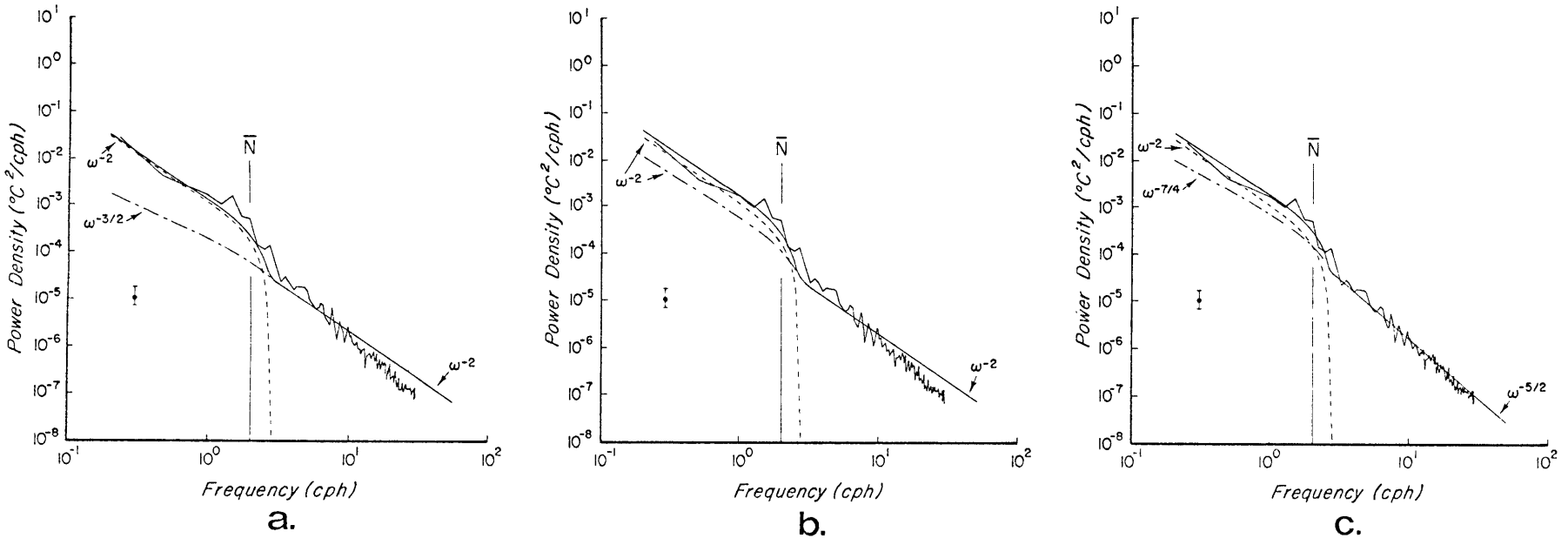


Figure 4.1. Model and observed temperature spectra. The observed temperature spectra shown here and temperature difference spectra and temperature coherences shown in succeeding figures were computed from a 3-day record. Averages are over 18 adjacent frequencies; error estimates for 95% confidence are at the left. Model curves of the mean-gradient contribution (dashed curves), the fine-structure contribution (dot-dashed curves) and the total temperature spectrum (solid curves) are drawn. Spectral slopes are asymptotic values for $\omega << N$ and $\omega >> N$. Sheet-layer or constant-gradient model curves are in (a) and constant-curvature model curves are in (b). A passive wavenumber spectrum of the form $P_T(k) = A_T k^{-5/2}$ is used to produce (c).

Process-specified models

Our simplest process-specified models are the sheet-layer and constant-gradient models. As discussed previously, the constant A is non-zero and B $\equiv$ 0 for these models, indicating that fine-structure contribution to temperature spectra is found from the square root of the internal wave displacement structure function (see equations 4.1.12a,b)). Hydrographic surveys near Bermuda made by T. Sanford and N. Hogg of W.H.O.I. a few weeks prior to the third MSA experiment (October-November 1975) provide us with the basis for an estimate of A. T. Joyce, also of W.H.O.I., generously interpreted these data in terms of a sheet-layer model, a computation he made for similar data from the Sargasso Sea (see Joyce and Desaubies (1976)). In the depth range 500-600 m, these Brown-W.H.O.I. CTD hydrographic casts indicate $\overline{\theta^2} \simeq 1.3 \times 10^{-4}$ °C^2 and $\bar{h} \simeq 125$ cm. However, $\overline{\theta^2}$ varies by roughly a factor of two in the 5 stations closest to the MSA deployment sites (see Figure 2.2) so that $A = \overline{\theta^2}/\bar{h}$ is as low as 5.08×10^{-7} °C^2/cm at station KN52-64 or as high as 1.10×10^{-6} °C^2 cm at KN52-48. Note higher values for A are computed from casts in shallower water (i.e., fine-structure is more intense nearer the island, as mentioned in the introduction). But the level we infer from moored temperature spectra using this model is roughly a factor of 2 higher than the highest $\overline{\theta^2}/\bar{h}$ inferred from hydrographic measurements. Figure 4.1a shows the sheet-layer model temperature spectrum using $A = 2 \times 10^{-6}$ °C^2/cm as the sum of a mean-gradient contribution (using $\overline{T_z} = 12.3 \times 10^{-3}$ °C/m, the time average temperature gradient over 7.13 m during the second experiment) and a fine-structure contribution. The mean-gradient contribution (dashed line) shows the

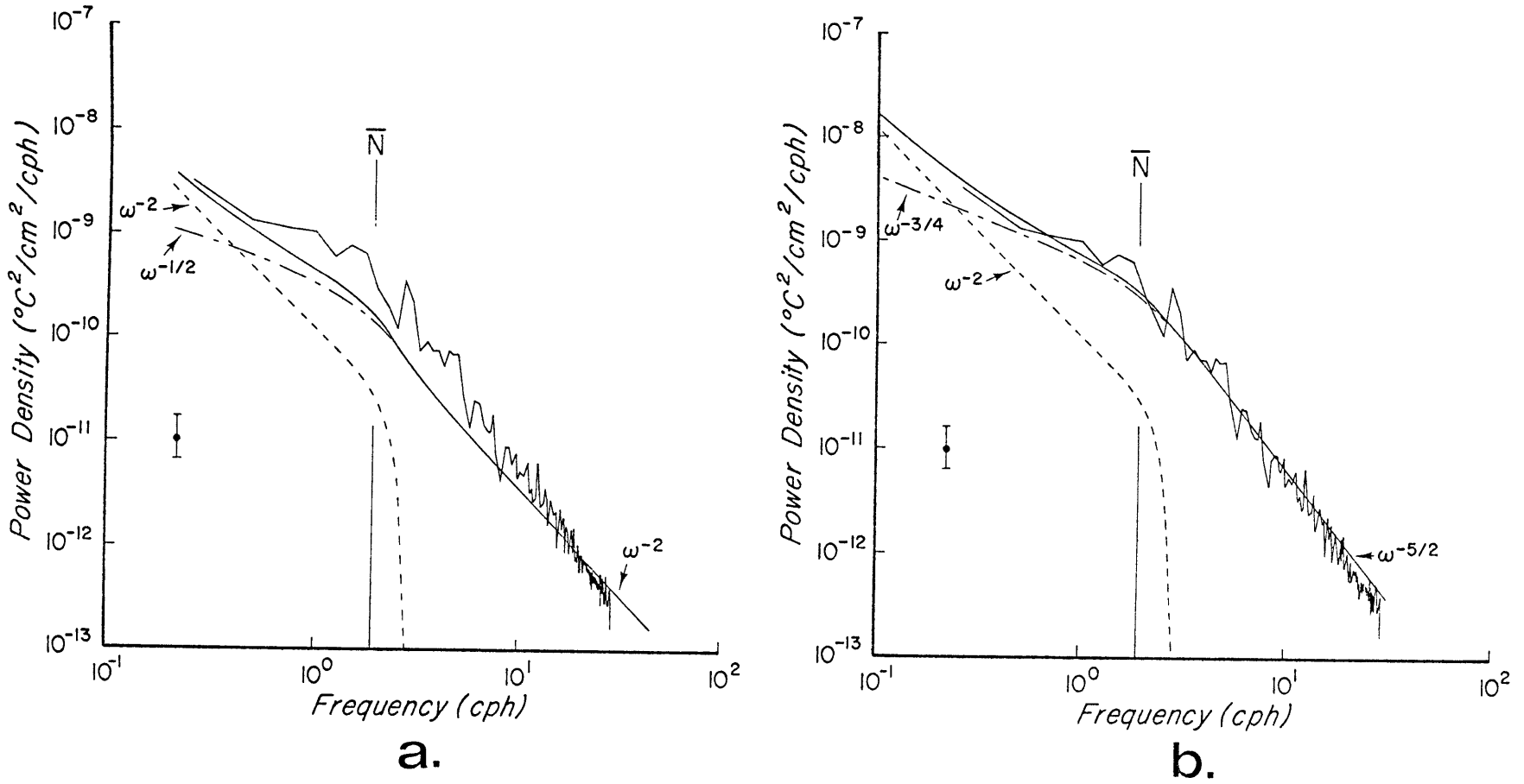


Figure 4.2. Model and observed temperature difference spectra over a 712.8 cm vertical separation (normalized by separation squared). Model curves of the mean-gradient contribution (dashed curves), the fine-structure contribution (dot-dashed curves) and the total temperature difference spectrum (solid curves) are drawn. The fine-structure contribution exceeds the mean-gradient contribution at all but very low frequencies, so that for most of the internal wave range fine-structure (kinematical) effects dominate temperature difference. A process-specified model (B=0) is used in (a), a wavenumber spectrum specified model with $P_T(k) = A_T k^{-5/2}$ is used in (b).

smooth, sharp internal wave cutoff just above $\bar{N}$ and the familiar ω^{-2} portion at lower frequencies (the curve drawn in Figure 3.4b uses the same parameters). The fine-structure contribution (dot-dashed line) displays the $\omega^{-3/2}$ and ω^{-2} slopes derived in equation (4.1.16) joined by a connecting region near $\bar{N}$. The measured spectrum shows a steeper slope at high frequencies than predicted by either the sheet-layer or constant-gradient models. Also, the model curve does not follow the measured spectral level below $\bar{N}$; the model level is too low. We may adjust this level without altering our previous choice of internal wave spectral level E by using the constant-curvature model. Having no a priori knowledge of θ" from hydrographic measurements, choice of B (equation (4.1.9)) is governed by "goodness of fit" to the moored spectra. The fine-structure contribution using $B = 5 \times 10^{-9}$ $°C^2cm^2$ (Figure 4.1b) is proportional to the mean gradient contribution at low frequencies but behaves as the sheet-layer or constant-gradient models at high frequencies. Although the low-frequency level fits better with this model than with the simpler versions, the observed behavior at high frequencies is still not reproduced. This is the principal shortcoming of the process-specified models.

Before leaving these models, however, let us explore their predictions of temperature difference spectra and coherence. Using the sheet-layer or constant-gradient model with $A = 1 \times 10^{-6}$ $°C^2/cm$ (note the reduction of A by a factor of two, necessary to fit the temperature difference spectra) and $B = 0$, the temperature difference spectra are computed for various separations available on the MSA. We use $z = 100$ m. Figure 4.2a shows the temperature difference spectrum

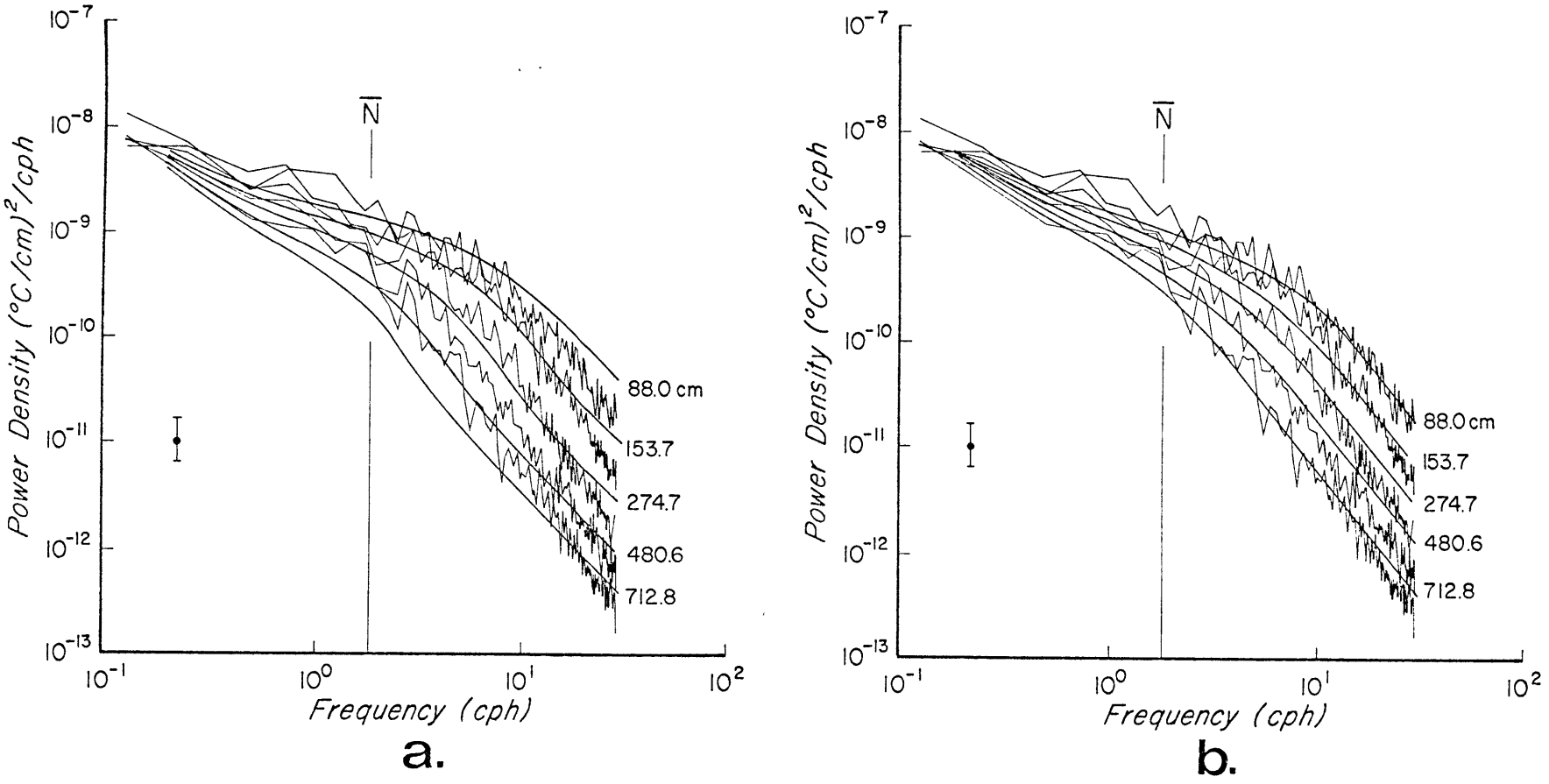


Figure 4.3. Model and observed temperature difference spectra over a range of different separations. The models and model parameters are the same as in Figure 4.2.

divided by the separation (2.13 m) squared. We follow the convention of normalizing the temperature difference signal by the vertical separation, remembering that the finite difference is an approximation to the vertical derivative. The mean-gradient temperature difference spectrum (dashed line) arising from the first three terms in (1) behaves as the mean-gradient spectrum itself and has considerable influence at low frequencies. The fine-structure contribution (dot-dashed line) displays the asymptotic behavior predicted by (4.1.17) at both high and low frequencies. Near $\bar{N}$, as with the simple spectra, the high and low frequency curves connect in a complicated fashion. As with the model temperature spectrum, the process-specified model temperature difference spectrum fails at high frequencies by decreasing too gradually. At low frequencies, however, Figure 4.2a indicates that the mean-gradient contribution dominates. The crossover frequency between fine-structure and mean-gradient domination can be altered by changing the model buoyancy frequency profile (e.g., changing z given N(z) and N_o). For a given profile, of course, the crossover frequency is a function of A. Further evidence of mean-gradient domination of temperature difference spectra at low frequencies can be gleaned from the IIWA measurements. The six separations available on one of the IIWA moorings were used to calculate the spectra in Figure 4.4. In the range roughly between 0.1 cph and 0.4 cph they drop as ω^{-2}; unfortunately a 16-minute sampling interval made resolution of high frequency ($\omega >> \bar{N}$) behavior impossible in these records, but they do show steeper slopes at roughly 1 cph. The ω^{-2} slopes at lower frequencies indicate the dominance of mean-gradient contribution to the temperature difference

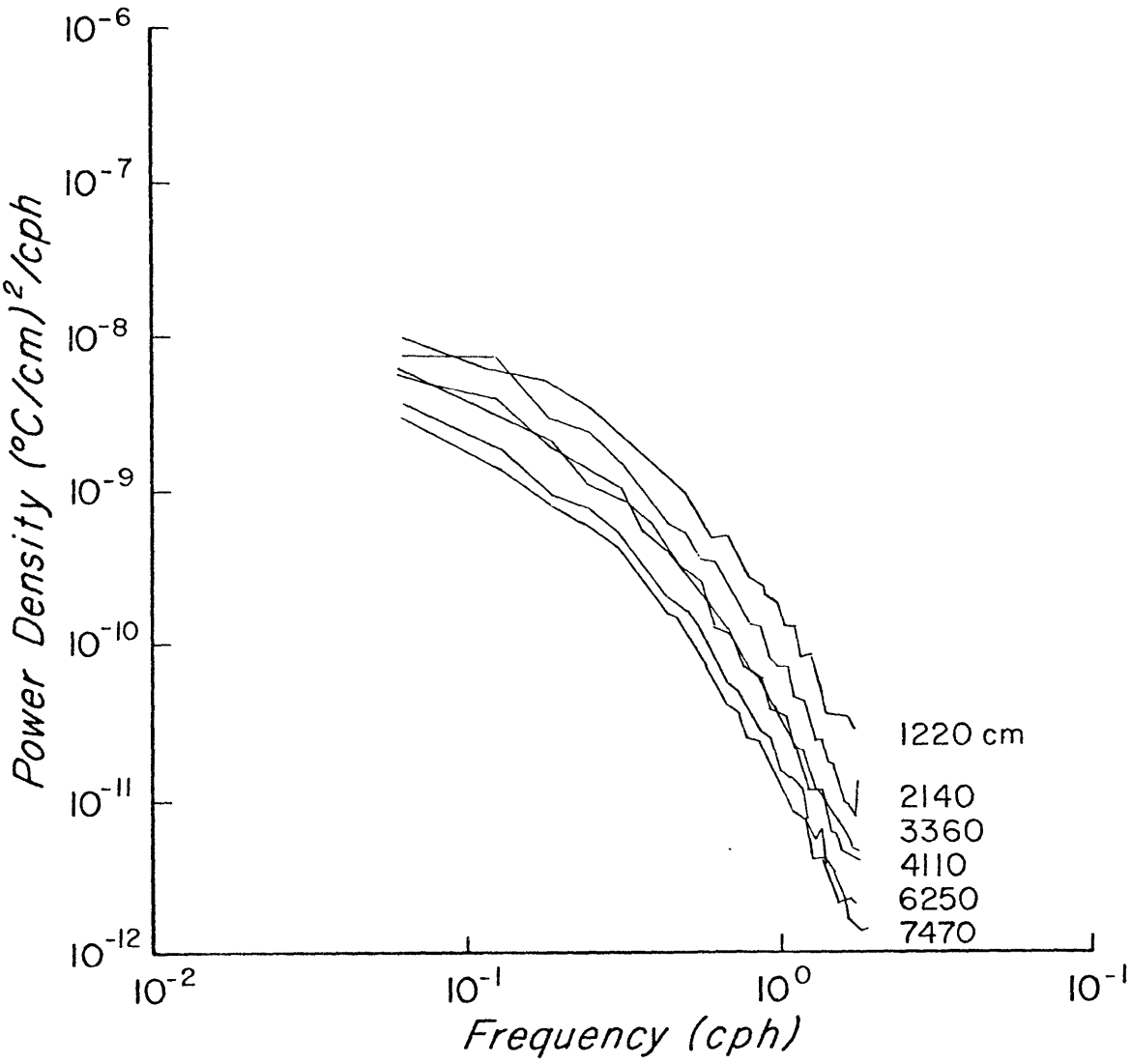


Figure 4.4. IIWA temperature difference spectra at different separations, normalized by the separation squared. These spectra are computed from 50-day records; averages are over 75 adjacent frequencies.

spectra in this range. Both model and observed temperature difference spectra for various separations on the MSA are displayed in Figure 4.3a. Curves for all separations show the basic defect of the process-specified models; they fall off too gradually at high frequencies.

Finally, we mention the vertical coherence predictions of the process-specified models. Coherence measurement (solid irregular curve), mean-gradient coherence (box-like solid curve), process-specified model fine structure coherence (lower dashed curve) and process-specified model total coherence (upper dashed curve) are shown for four separations (one from the IIWA, three from the MSA) in Figures 4.5a-d. The additional solid curves are calculations from the wavenumber spectrum-specified model to be discussed next. The qualitative features of the model are: total coherence drops monotonically with increasing frequency below the cutoff; near the cutoff total coherence drops sharply to the value of the fine-structure coherence; at higher frequencies the total coherence is just the fine structure coherence. The cutoff (at the frequency range for which total coherence drops precipitously just below the edge of the box-like internal wave coherence curve) occurs where the fine-structure ratio $\gamma(\omega)$ passes through unity for both sensors 1 and 2 (at different frequencies). Model total coherence consistently over-estimates observed coherence at large separations (Figure 4.5a), under-estimates observed coherence at small separations (Figure 4.5d), and seems to do relatively well at intermediate separations (Figures 4.5b,c). In this usage, intermediate separations are those for which the half- or eight-tenths coherence frequencies (the frequency at which coherence drops to 0.5 or 0.8) change little with separation. Another way

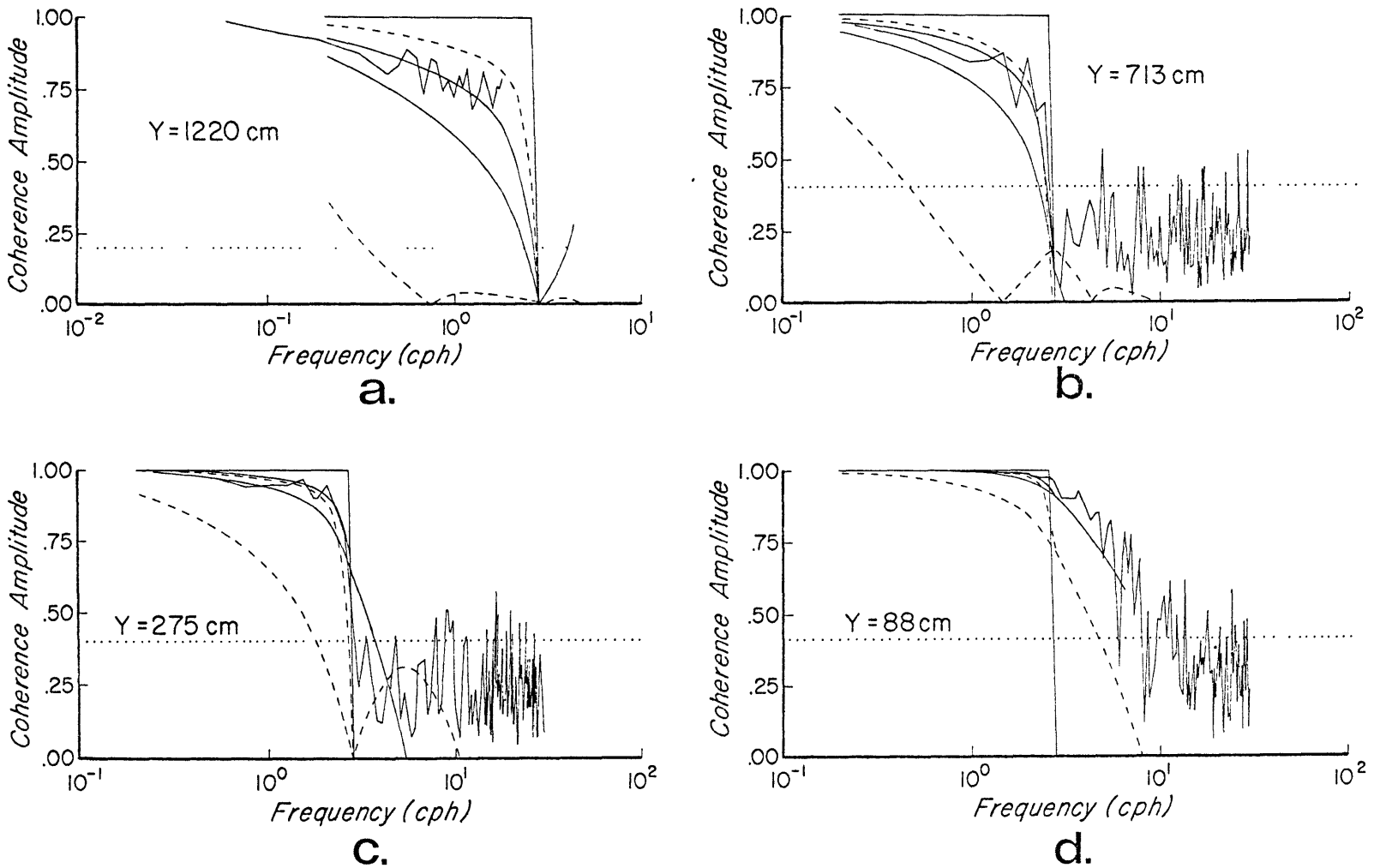


Figure 4.5. Model and observed temperature coherences over four separations Y. Box-like solid curves are model mean-gradient coherence. Dashed curves are for the same process-specified model as in Figure 4.3a. Solid curves are for the same wavenumber spectrum-specified model as in Figure 4.3b. The model parameters are the same for all separations for each model. The lower curve (dashed or solid) is the fine-structure coherence defined by equation (4.2.3). The upper curve (dashed or solid) is total coherence given by (4.2.2). At frequencies above the cutoff (where mean-gradient coherence drops to zero), the total coherence is the fine-structure coherence. Dotted horizontal lines are drawn at the level of significantly non-zero coherence with 95% confidence.

of stating this rough definition, meant only for convenience in describing the coherence curves, is to say that coherence length changes very rapidly at intermediate separations. We plot both half- and eight-tenths coherence frequencies (circles and squares, respectively) in Figure 4.6. Solid symbols represent IIWA data, open ones represent MSA data. Dashed curves show the process-specified model predictions. At large separations coherence depends a bit on the number of modes and the position z for this model, hence the trifurcation of the eight-tenths coherence curve. This weak dependence corresponds to variation in shape of the "elbow" in the coherence curve near $\overline{N}$ (1.91 cph). At separations greater than about 30 m observed temperature half- and eight-tenths coherence frequencies are roughly inversely proportional to separation (similar to Webster's (1972) reports of current coherences). At separations smaller than about 1.5 m they behave similarly. Transition regions connect these extreme regions to the intermediate separation region (roughly 1.5 m to 7.0 m). Although the process-specified models indicate the observed inverse relationship at small separations, they incorrectly predict the transition separation to be a factor of 2 or 3 lower than the observed transition separation (1.5 m). At larger separations the models overestimate coherence (see Figures 4.6 and 4.5a), whereas they underestimate it at small separations. As expected then, they imitate the observed coherences reasonably well at intermediate separations, since coherence drops so rapidly at the cutoff for these separations (see Figure 4.5b). A more physical (and quantitative) interpretation of the classification of separations Y into large, intermediate, and small is that for a given coherence level, large,

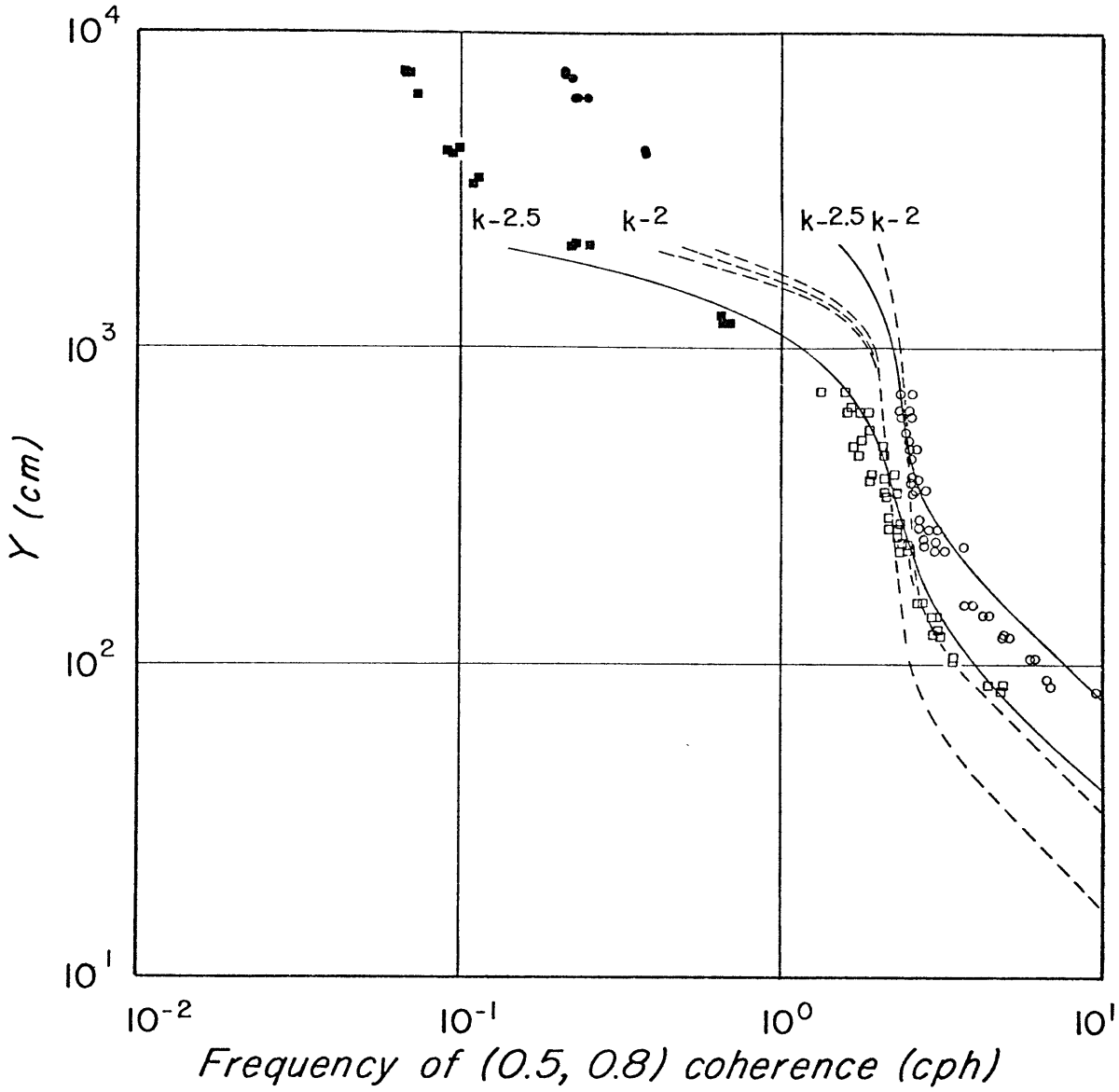


Figure 4.6. Temperature half-coherence and eight-tenths coherence frequency as a function of vertical separation Y. Squares (circles) denote observations of eight-tenths (half) coherence. Solid (open) symbols are computed from IIWA (MSA) data. Solid (dashed) curves are drawn for the wavenumber spectrum-specified (process-specified) model used in previous figures. Note the process-specified model is equivalent to a k^{-2} wavenumber spectrum-specified model. The $k^{-2.5}$ spectrum-specified model fits the observations better than the k^{-2} model.

intermediate, and small separations are those for which fine-structure coherence is much smaller, comparable, and much greater than the given level near the cutoff. Thus any fine-structure model with a cutoff (i.e., $\gamma(\omega) \simeq 1$ in some frequency range) will have an intermediate range of separations for which coherence predictions will not be far wrong. The process-specified models should not be regarded as particularly meritorious, since their coherence predictions seem reasonable only where many other models would also seem reasonable.

Wavenumber spectrum-specified models

Notice the other model curves plotted on figures adjoining those just discussed. These figures are juxtaposed for comparison; the observed spectral quantities are the same in each case, but the models differ. The remaining set of model curves was produced with a wavenumber spectrum-specified model with $P(k) = A_T k^{-5/2}$. The exponent -5/2 was chosen with more than the justification that it seems to work; vertical wavenumber spectra measured in the main thermocline of the Sargasso Sea (Hayes, Joyce, and Millard 1975) and near Bermuda (N. Hogg, private communication) are roughly of the form $A_T k^{-5/2}$ from 0.1 cpm to 1.0 cpm. Hogg also reports steeper spectral slopes for many hydrographic observations at different depths and locations. Moored measurements made in these locations and depths would show steeper high frequency behavior; the model derived in the last section can readily be changed to reflect such a different specified wavenumber spectrum. Since no direct measurements of P(k) were made during the MSA experiments, we can only postulate that the commonly occurring wavenumber slope -5/2 would have been measured had hydrographic casts been made.

This postulate is supported by the excellent agreement (to be demonstrated below) between vertical wavenumber spectra measured by others and MSA frequency spectra interpreted through the model.

The wavenumber spectrum-specified model temperature spectrum is plotted in Figure 4.1c using the same plotting convention as in Figures 4.1a and 4.1b showing the mean-gradient contribution (dashed curve), the fine-structure contribution (dot-dashed curve), and their sum (solid curve). The level A_T' in equation (4.1.23) is easily related to the spectral level A_T. In this figure and succeeding ones depicting temperature difference spectrum and coherence, the level $A_T' = 10^{-7}\ °C^2/cm^{3/2}$. Estimates of A_T' from Hayes, Joyce, and Millard (1975) for the depth range 600-800 dbar in the Sargasso Sea and from Hogg's Eastward station 24 (see Figure 2.2) for the range 700-800 dbar are $A_T' = 0.67 \times 10^{-7}\ °C^2/cm^{3/2}$ and $1.55 \times 10^{-7}\ °C^2 cm^{3/2}$, respectively. These estimates, chosen roughly by fitting a spectrum $P(k) = A_T k^{-5/2}$ at k = 1 cpm, nicely bracket the value chosen in Figure 4.1c. With this model the observed spectral behavior is well imitated in the full range of frequencies considered. Since the fine-structure contribution falls off more gradually at low frequencies than for the simple process-specified models, the model spectrum closely follows the observed spectrum without need of the constant curvature model to raise the level in this range (as was done to produce Figure 4.1b). At high frequencies the success of the model prediction is self evident in Figure 4.1c. Finally, the transition region between mean-gradient and fine-structure dominated portions of the spectrum is rather well predicted by the model. The objection which arose over the process-specified models has been answered: the shape of the temperature

spectrum is followed closely by the model throughout the frequency range of interest while the parameter A_T' characterizing the fine-structure level is consistent with hydrographic measurements.

As mentioned in the introduction to this section, if the model fits the temperature spectra reasonably, one expects that predictions for temperature difference spectra will also fit the observations. The curves in Figure 4.2b show that this expectation is fulfilled. The position estimate z = 100 m is retained in order that the mean-gradient contribution become dominant at lower frequencies, even though the rough profiles of $N^2(z)$ (Figure 3.1) indicate a choice of z = 150 m would be more reasonable. This is our most serious compromise, but cannot be considered a grave one considering the parabolic approximation to the $N^2(z)$ profiles. The model curves in Figure 4.3b show model fits for a variety of separations. The envelope of curves generally fits better than the one arising from the process-specified models (Figure 4.3a) especially since the former fall as $\omega^{-5/2}$ at high frequencies, closely matching the observed spectral slopes. Deviations of the observed spectra from the model predictions are nowhere greater than the error bars associated with the spectra.

Finally, vertical coherence of temperature is predicted by the model. Figures 4.5a through 5d display model fine structure coherence (solid lower curve) and model total coherence (solid upper curve) in addition to the curves already discussed. The model reproduces the gross features of the observed coherences. A summary of coherence-length predictions appears in Figure 4.6. In contrast with the process-specified models, wavenumber spectrum-specified model curves (solid curves) follow the transitions in coherence length behavior at

roughly 10.0 m and 1.5 m separations. At small separations (high frequencies), coherence length is inversely proportional to frequency as before, but the level of the curve seems to match the observations, indicating that modelling of fine-structure coherence is correct in this range. The model curve follows the transition between large and intermediate separations reasonably well for eight-tenths coherence. There are no data for half-coherence in this range due to sampling rate of the IIWA instruments, but we can imagine that the solid and open circles connect in similar fashion to the eight tenths coherence data. The model curve for half-coherence seems to have an appropriate trend in this transition region. Thus for small, intermediate, and the transition to large separations, the -5/2 wavenumber spectrum model predicts coherence satisfactorily.

It has now been demonstrated that a particular wavenumber spectrum-specified model seems to describe moored spectra and cross spectra of temperature adequately. The model is designed to explain observations near and above the local buoyancy frequency, since it is based on an internal wave model which approximates the $N^2(z)$ profile well only for frequencies 1.0 cph and higher. Below roughly 1.0 cph modes cannot be trapped in the main thermocline, since N(z) increases from about 1.0 cph at 300 to 400 m as the surface is approached. Modes at lower frequencies are bounded above by the ocean surface and below by the stratification (or, at even lower frequencies, the ocean bottom). No attempt has been made to model the transition between these single turning-point modes at low frequencies (discussed by Desaubies (1973)) and our thermocline (two turning-point) modes. Temperature coherence at low frequencies is affected by mean-gradient (internal wave)

coherence as well as fine-structure coherence, so we need to model internal waves in both regimes. In this scenario we suddenly change from thermocline modes to single turning point modes at about 1.0 cph. Where wave functions are roughly in phase spatially for different (low, energetic) modes trapped in the thermocline near N(z), as we travel away from the turning point at a constant depth by decreasing frequency, the different modes become out of phase spatially, thus reducing coherence. Yet low modes have not yet reached their first zero crossing as 1 cph is approached. At frequencies below 1 cph modes are trapped over a much greater depth so that a given thermocline mode will have the same vertical scale as a higher single turning point mode. Again, we expect low modes to dominate vertical coherence behavior, but the relative phases of the single turning point modes will in general be very different than for thermocline modes at nearly the same frequency ($\gtrsim$ 1 cph). In other words, coherence behavior with frequency is expected to be governed by different physical situations above and below about 1 cph. Measured temperature coherence at large separations ($\gtrsim$ 20 m), reminiscent of Webster's (1972) horizontal current vertical coherence length observations, is not explained by our model based on thermocline mode internal waves. Note that besides possible explanation in different internal wave coherence behavior, fine-structure coherence increases monotonically with decreasing frequency (see Figures 4.5a-d) so that the fine structure effects may also contribute. The fine-structure ratio $\gamma(\omega)$ behaves only as $\omega^{1/4}$ in the -5/2 wavenumber spectrum-specified model ($\omega^{1/2}$ in the process-specified models) so that

fine-structure coherence can affect total coherence at frequencies a decade or more below N(z) (see Equation 3c).

As mentioned earlier, there is nothing special about a -5/2 wavenumber spectrum of the undisturbed medium; it simply seems to fit the moored data well from the MSA experiments, as evidenced by spectral slopes and levels, giving internal consistency to the model. Were the MSA placed further from the island, deeper or shallower, or at a different time, a different P(k) might be appropriate. Hayes, Joyce, and Millard (1975) demonstrate variability of P(k) with depth and Hogg's measurements near Bermuda (1976, personal communication) indicate variability with water depth and time (on the time scale of mesoscale eddy motions). A steeper profile than -5/2 would produce steeper frequency behavior above $\bar{N}$, a flatter fine-structure ratio $\gamma(\omega)$ in the internal wave range, and a less "step-like" coherence length variation with frequency (compare the dashed (k^{-2}) and solid ($k^{-5/2}$) curves in Figure 4.6). Finally we note that Joyce and Desaubies (1976) remarked that temperature difference spectra could be used to evaluate the fine structure level. Our results show that both the slope of the moored temperature spectrum at high frequencies and its level may together be used to estimate the vertical wavenumber spectrum of temperature at wavelengths comparable to internal wave displacement scales (roughly 1 to 10 m in the present case). Thus we avoid assuming a fine-structure formation process in determining the fine-structure level from moored measurements.

As mentioned at the beginning of this chapter, the fine-structure wavenumber spectrum is altered by internal wave strain. Garrett (1973) showed that an undisturbed profile with spectrum $P_T(k) = A_T k^{-p}$ would

be augmented by an amount $\frac{1}{2}(2-p)(1-p)\overline{(d\zeta/dz)^2}A_T k^{-p}$ in the presence of waves where $\overline{(d\zeta/dz)^2}$ is the mean square wave strain. As he pointed out, a k^{-2} spectrum (to which a sheet-layer model corresponds) would be unchanged by straining. However, a $k^{-5/2}$ spectrum would be augmented by a fractional amount $0.375\ \overline{(d\zeta/dz)^2}$. The internal wave model of Chapter 3 allows evaluation of this fractional change. Differentiating (3.1.19c) with respect to z and integrating with respect to time gives an expression for strain of a wave of mode n:

$$d\zeta_n/dz = i\ \frac{E(\alpha,\omega)\sqrt{2n+1}}{\sqrt{\pi}\ n!\ 2^{n-1}}^{1/2}\ \frac{\sqrt{2n+1}}{N_o^2\mu^2}\ e^{-\eta^2/2}(nH_{n-1}(\eta) - \frac{H_{n+1}}{2}(\eta)) \qquad (4)$$

The strain spectrum $P_{\zeta_z}(\omega)$ is then:

$$P_{\zeta_z}(\omega) = \sum_n \frac{E(\alpha,\omega)(2n+1)^{3/2}}{\sqrt{\pi}\ n!\ 2^{n-1}N_o^2 z^2}\ \frac{N_o^2 - N_{(z)}^2}{N_o^2 - \omega^2}\ e^{-\eta^2}(nH_{n-1}(\eta) - \frac{H_{n+1}}{2}(\eta))^2 \qquad (5)$$

With $E(\alpha,\omega) = E(\alpha/\alpha_o)^{-2}\ (\omega/N_o)^{-2}$ as in the other calculations in this section, (5) may be integrated over frequency to obtain mean square strain.

Evaluation of $\overline{(d\zeta/dz)^2}$ was done numerically for the range 0.2 cph to 2.7 cph (i.e., over all but low frequencies in the internal wave range). The result varies as the inverse square of the thermocline half-width (μ at the turning point) and depends on the number of modes present. The mean square strain over this range is 0.76×10^{-3}, 3.20×10^{-3}, and 6.42×10^{-3} for the first 6, 11, and 21 modes. This largest figure corresponds to a fractional increase in the level of $P_T(k)$ by less than a quarter of one percent. Mode number 20

corresponds to waves roughly 15 m long at $\omega \simeq N(z)$ for $z = 150$ m. Shorter waves than this will be affected by quasi-permanent features of fine-structure. Our thermocline-trapped mode model fails to predict these interactions, but the modification of a purely passive fine-structure profile by less than 0.25% by waves of 15 m wavelength or longer suggests that wave strain by shorter waves may still be small (a few percent or less). The frequency spectra $P_{\zeta_z}(\omega)$ are red, however, so these figures underestimate mean square strain. Regardless, as Garrett also concluded, strain is likely to make only a small contribution to vertical wavenumber spectra.

We have modelled fine-structure as a passive vertical field in this chapter and have found this approach seems to describe moored temperature measurements. The passive field is described by its vertical wavenumber spectrum. But is fine-structure really passive? The model employed in this study assumes the vertical structure of a tracer (temperature in this case) is known; temporal variation is taken account only in the probability distribution of internal wave displacement differences. If the fine-structure varies on time scales comparable to internal wave periods (for instance if the fine-structure is partially the signature of vertically short internal waves), then the kinematic picture is one of a time-varying vertical field advected by random internal wave displacements. The model used here interprets this sort of situation by separating all temporal and spatial variation. Because the displacement spectrum is strongly red, high wavenumber temporal variation is unresolved in the MSA data sets; fine-structure may be a static vertical field or internal waves or (more probably) a combination of both. The model employed is designed

to describe the first possibility, but also describes the other two possibilities because the dominant displacements contributing to $D_\zeta(\tau)$ in (4.1.2) are from vertically long waves. In other words, the idealized passive profile used in this model resembles measured profiles whether small distortions due to vertically fine-scale internal waves are included or are not included; they do not make much difference. Drop spectra (wavenumber spectra derived from vertical profiles) measure variance at all frequencies; with a red frequency spectral dependence they are dominated by the wavenumber structure at the lowest frequency band, including zero frequency. How much of the variance in drop spectra is due to internal waves (in particular, in the range 0.1 cpm to 1.0 cpm, i.e., wavelengths comparable to internal wave displacements) is not known but the calculations in the preceding paragraph suggest only a small fraction is due to wave strain. Gregg (1976) observes a change to steeper slope at higher wavenumber at roughly 0.1 cpm in his temperature drop spectra. This change may reflect change in the internal wave spectrum $E(\beta,\omega)$ or may be due to static vertical variation or some combination of these. The temporal variation we observe in contour maps of temperature from MSA thermistors on either mast suggests that a combination of the two effects is likely. (These contour maps are discussed in Chapter 5 in connection with wave breaking.) Although a distinction between fine-scale internal waves and passive fine-structure is made neither in our models nor in the analysis of MSA data, the kinematic contribution of fine-structure to moored temperature measurements is identifiable. The analysis in this chapter is unchanged by use of a vertically advected field that has small (and/or slow) temporal variation.

4.3 Horizontal current fine-structure effects

The temptation to apply a model of passively advected fine-structure to horizontal current measurements is irresistable if not completely successful, as this section will show. Our hint is that the spectra of horizontal current and temperature are strikingly similar (see Figures 3.4a,b). If temperature fine-structure can be described as a passive field of some vertical wavenumber spectrum, it seems plausible that horizontal current fine-structure effects may be treated similarly. Two kinds of models come to mind. One is that horizontal current fine-structure exists independently in the water column; we imagine that some fluctuations one measures with a vertically dropping instrument arise from non-internal wave mechanisms (e.g., small scale mixing, intrusive motions, etc.). The other is that horizontal current fine-structure is directly caused by internal waves in a medium with fine-scale buoyancy frequency fluctuations, given a vertical current which varies over scales larger than the fine-structure, horizontal currents are induced with vertical scale comparable to the scale of $N(z)$ variations. The difference between these models is that the first is a purely passive current field that is advected vertically by internal waves, whereas the second is a passive field of density (temperature) advected by internal wave displacements which dynamically links vertical and horizontal current fluctuations. The same formalism used to describe temperature fine-structure will be used for horizontal current fine-structure for the first model. We shall see that modelling of dynamically-induced current fine-structure is difficult because of the complexity of the equations of motion.

The McKean (1974) model for temperature fine-structure was based on an approximation to the heat equation

$$T_t = -wT_z \tag{1}$$

where temperature is a passive vertical field. Time dependence in temperature measured at a given depth arises only through time dependence of w(z,t) which advects a passive (i.e., time-invariant with respect to itself) temperature profile. Integrating (1) under this constraint gives:

$$T(z,t) = -\int^{t} w \frac{dT}{dz} \tag{2}$$

From this formulation, the integral expression (4.1.2) relating the structure function of time lag to the structure function of the passive medium (a function of vertical lag) was established by McKean. We wish to calculate the structure function for horizontal current in a similar manner. In the first model mentioned in this section, horizontal current is treated as a passive field (a tracer) so formulation is exactly as with temperature. In the second model, a dynamical link between horizontal and vertical current is sought which can be expressed in the form of equation (4.1.2).

In the second model, an equation similar to (1) can be derived from (3.1.1a-e), but this rules out the existence of fine-structure in N, since $\overline{\rho_z}$ is time-invariant (a result pointed out to the author by T. Joyce of W.H.O.I.). By writing $\rho_z(z,t)$ in the equation for density

(3.1.1e) instead of $\overline{\rho_z}$, we can derive an equation relating shear to vertical motion through $N^2(z,t) = -(g/\rho_o)\rho_z(z,t)$:

$$u_{ttz} = (wN^2)_x + w_{ttx} \tag{3}$$

Fine-structure variation in N (i.e., N = N(z,t)) makes the Fourier transform of this equation cumbersome, since the product wN^2 will be a convolution. To cast (3) into a form similar to (1) so that the passive-advective McKean model may be used appears beyond reach.

The former model (horizontal current fine-structure as a passive vertical field) shall be pursued instead. The temperature fine-structure model assumed a given vertical wavenumber spectrum $P_T(k)$ for T(z), the undisturbed profile. Similarly, to find the horizontal current fine-structure contribution, the vertical wavenumber spectrum $P_U(k)$ can be specified. Vertical wavenumber spectra computed from profiling measurements indicate $P_u(k) \alpha k^{-p}$ where P is between 2 and 2.5 (Sanford (1975)). Since models for k^{-2} and $k^{-5/2}$ spectra were developed earlier for temperature fine-structure and neither produce the appropriate frequency structure for moored spectra, a model using $P_U(k) = A_U k^{-9/4}$ (as Sanford's spectra indicate) shall be developed here. The spectrum $P_U(k)$ is used in (4.1.2) to obtain the fine-structure structure function $D_{U_{fs}}(\tau,Y)$. The mean-gradient contribution to horizontal current is taken directly from the internal wave expressions (3.1.19).

As mentioned earlier, the fine-structure model developed earlier (3.1.19-3.1.38) may be easily altered to apply to a different wavenumber spectrum than $k^{-5/2}$. If $P_U(k) = A_U k^{-9/4}$, we find the structure function of the medium to be:

$$D_{U_m}(y) = \frac{A_U y^{5/4}}{\sin \frac{5\pi}{8}\,\Gamma(9/4)} \tag{4a}$$

$$= A'_U\, y^{5/4} \tag{4b}$$

Then the fine-structure structure function $D_{U_{fs}}(\tau,Y)$ is:

$$D_{U_{fs}}(\tau,Y) = A'_U \int_{-\infty}^{\infty} d\psi \left|\psi+Y\right|^{5/4} Q(\tau,Y;\psi) \tag{5}$$

which, using the Laplace probability distribution as before, is:

$$D_{U_{fs}}(\tau,Y) = \frac{A'_U}{2} \left(\sqrt{2D_\zeta(\tau,Y)}\right)^{5/4} \left(\Gamma(9/4)\left(e^{-x}+e^{x}\right)\right. \tag{6a}$$

$$\left. +e^{-x}\gamma(9/4,-x) - e^{x}\gamma(9/4,x)\right)$$

where x is as before. This reduces for Y = 0, to:

$$D_{U_{fs}}(\tau,0) = A'_U\Gamma(9/4)\left(\sqrt{2D_\zeta(\tau,Y)}\right)^{5/4} \tag{6b}$$

These expressions may be evaluated numerically using $D_\zeta(\tau,Y)$ based on the internal wave model developed earlier. Following previous derivations, the asymptotic forms for the fine-structure contribution

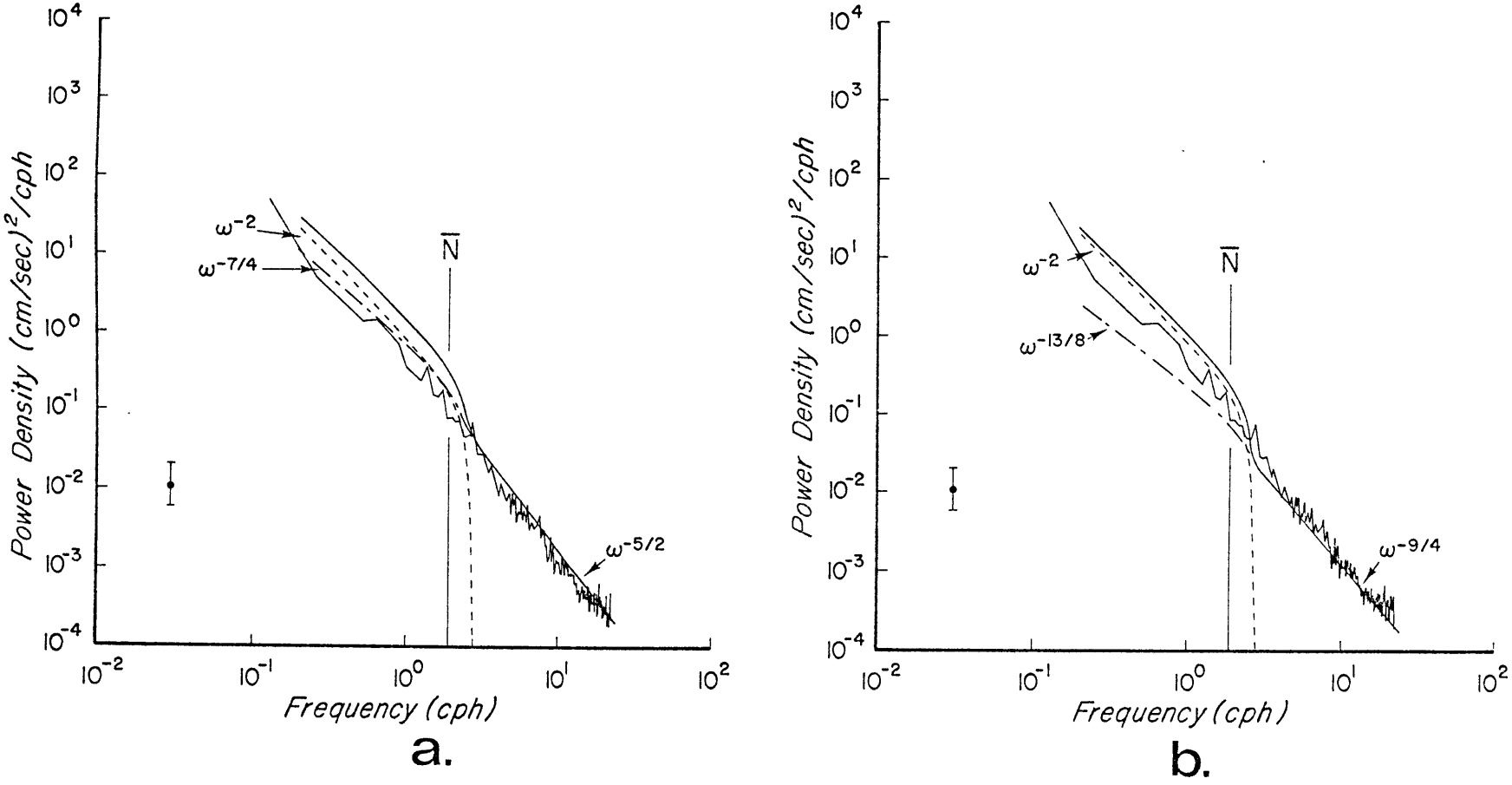


Figure 4.7. Model and observed horizontal current spectra. Model curves for mean-gradient (dashed) and fine-structure (dot-dashed) contributions to the spectrum are given as well as their sum (solid), using a $k^{-5/2}$ spectrum in (a) and a $k^{-9/4}$ spectrum in (b). Error estimates for 95% confidence appear at the left.

to the moored horizontal current spectrum and current-difference spectrum are (where N is the displacement field cutoff):

$$F_U(\omega) \cong \begin{cases} A_U' \Gamma(9/4) \left(\frac{2AN}{\pi}\right)^{5/8} \sin \frac{5\pi}{8} \Gamma(9/4) \omega^{-9/4} & \omega/N >> 1 \quad (7a) \\ A_U' \Gamma(9/4) 2^{5/4} A^{5/4} \sin \frac{5\pi}{16} \Gamma\left(\frac{13}{8}\right) \omega^{-13/8} & \omega/N << 1 \quad (7b) \end{cases}$$

$$F_{\Delta U}(\omega) \cong \begin{cases} A_U' \Gamma(9/4) \left(\frac{2N}{\pi}\right)^{5/8} (A_1^{5/8} + A_2^{5/8}) \sin \frac{5\pi}{8} \Gamma(9/4) \omega^{-9/4} & \omega/N >> 1 \quad (8a) \\ A_U' \Gamma(9/4) 2^{-3/8} A^{-3/8} Y^2 \cos\left(\frac{5\pi}{16}\right) \Gamma(5/8) \omega^{-5/8} & \omega/N << 1 \quad (8b) \end{cases}$$

The corresponding quantities for the $P_U(k) = A_U k^{-5/2}$ model are just those in equations (4.1.19) through (4.1.38) with A_U substituted for A_T.

Consider the model curves for horizontal current spectra in Figures 4.7a,b, corresponding to the $k^{-5/2}$ and $k^{-9/4}$ wavenumber spectrum models for horizontal current fine-structure. As before, dashed lines give the mean-gradient contribution and dot-dashed lines give the fine-structure contribution. The constant A_U' is 1×10^{-4} cm^2/sec^2/cm$^{3/2}$ in the -5/2 model and 2×10^{-4} cm^3/sec^2/cm$^{5/4}$ in the -9/4 model. The -9/4 model gives a marginally better fit than the -5/2 model, based upon slopes and levels above and below the turning point. Unfortunately, there are no suitable published drop spectra of horizontal current with which to compare spectral levels. Sanford (1975) shows drop spectra which fall roughly as $k^{-9/4}$ near the highest wavenumber he was able to resolve, about 5×10^{-2} cpm. If we extrapolate these results to the

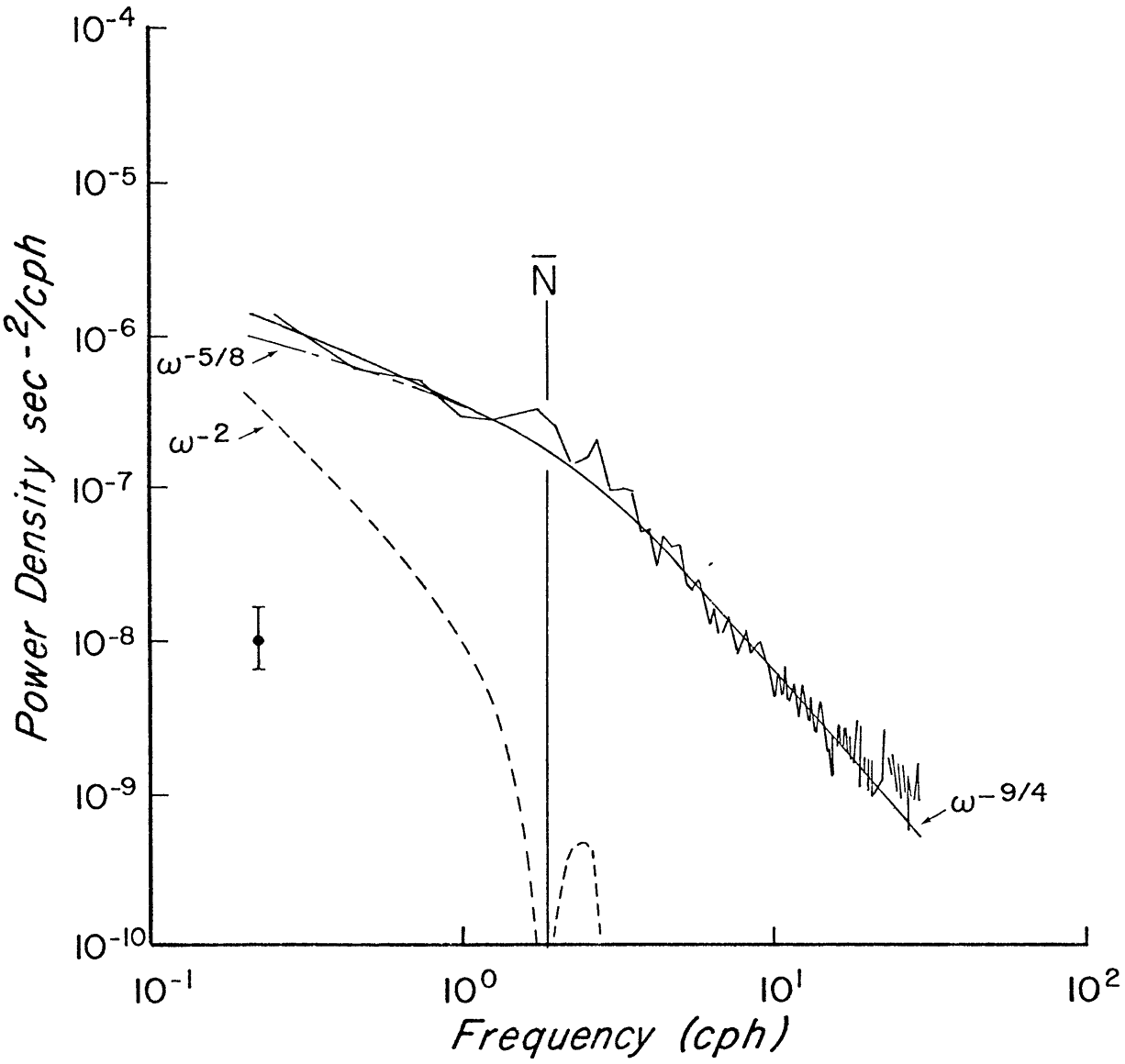


Figure 4.8. Model and observed horizontal current difference spectrum for a separation Y = 6.3 m. Mean-gradient (dashed curve) and fine-structure (dot-dashed curve) contributions as well as their sum (solid curve) are drawn for the $k^{-9/4}$ spectrum model using the same parameters as in Figure 4.7b. An error estimate for 95% confidence appear at the left.

range of interest we find the level of his spectrum corresponds to $A_T' = 1.5 \times 10^{-6} cm^2/sec^2/cm^{5/4}$, roughly two decades below the level inferred from the fit in Figure 4.7b. But this spectrum was computed from a profile from roughly 2000 m depth to 5200 m depth, where stratification is much weaker than in the main thermocline. Although Sanford indicates that fluctuations in the main thermocline are considereably more energetic, he has not published a spectrum based on thermocline profiles. The model level is internally consistent with fits to vertical current difference spectra as well, as will be shown next.

A spectrum of the first-difference approximation to vertical shear is given in Figure 4.8 along with a model curve (solid curve) composed of mean-gradient (dashed curve) and fine-structure (dot-dashed curve) contributions. The model curve fits remarkably well; it is the -9/4 model with $A_U' = 2 \times 10^{-4}$ $cm^2/sec^2/cm^{5/4}$, Y = 6.3 m and z = 100 m. Qualitatively, the spectrum is very similar to the first-difference spectrum of temperature; at very low frequencies the mean-gradient contribution is dominant, at high frequencies the spectrum drops as ω^{-p} where the undisturbed wavenumber spectrum is k^{-p}, and at intermediate frequencies the fine-structure contribution is flatter than above $\overline{N}$ or at low frequencies. Over most of the measured range, the finite-difference shear spectrum is attributable to fine-structure effects, a result whose implications will be discussed in Chapter 5.

A major shortcoming of our model at frequencies near $\overline{N}$ is illustrated in Figure 4.9, where horizontal current half-coherence frequency is plotted from two MSA data sets and from Webster (1972). Note that both the 2.8 m and 9.3 m vertical separations also include horizontal

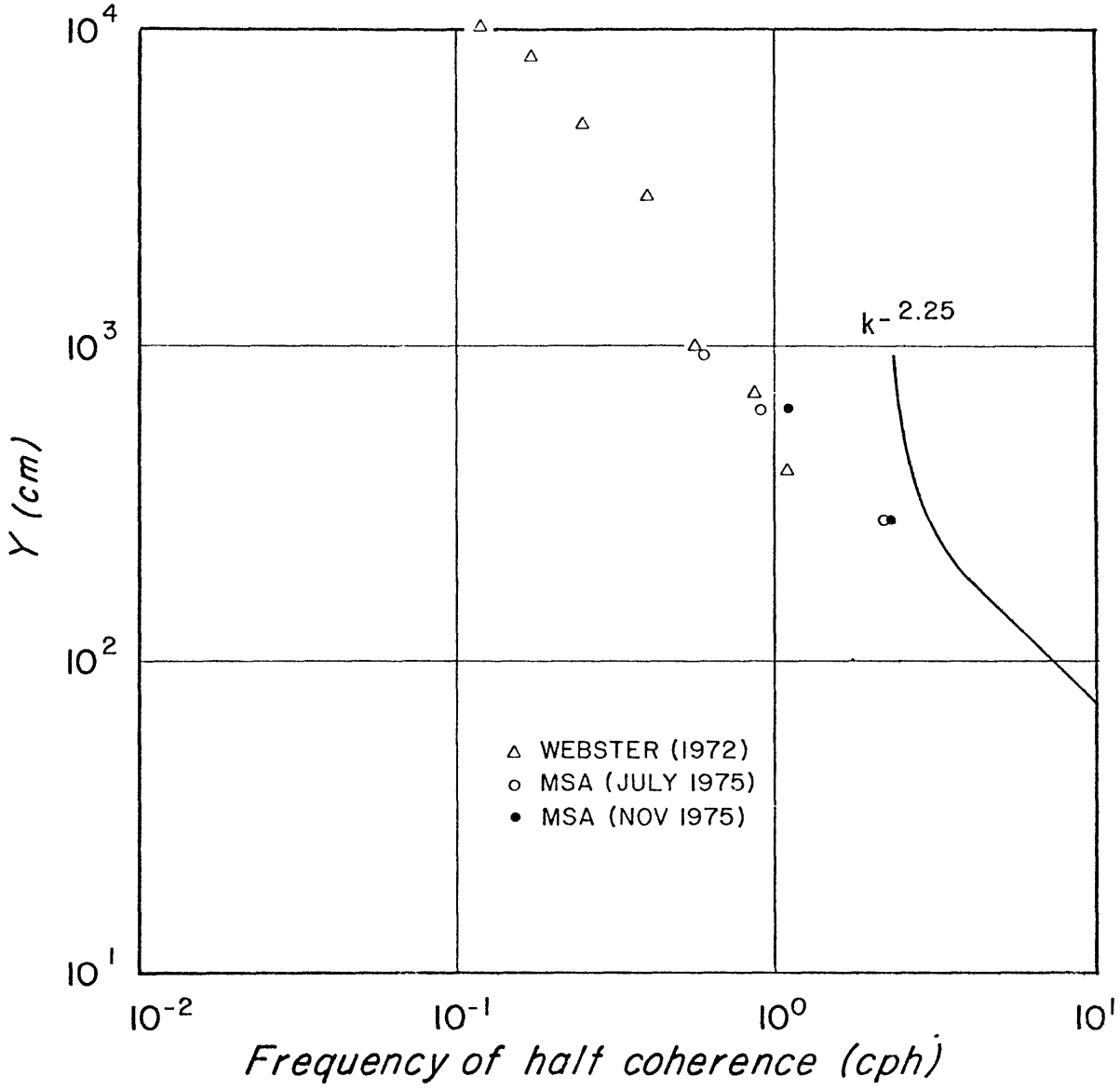


Figure 4.9. Horizontal current half-coherence frequency as a function of vertical separation Y. The curve is from the $k^{-9/4}$ spectrum model used in the curves of Figures 4.7b and 4.8.

separations of approximately 20 m. Since the fine-structure field is expected to extend horizontally much further than 20 m without substantial change, the horizontal separations are ignored in plotting these few data. The MSA observations fall close to those of Webster (1972). The model curve for $k^{-9/4}$ is given as well; it obviously deviates seriously from the measurements, but its deviation is in the frequency region about $\bar{N}$. Above the cutoff, model half-coherence frequency varies inversely with separation (as in the temperature fine-structure models), but we have no data from small separations with which to compare this behavior.

The simple model for horizontal current fine-structure seems to roughly describe the measured spectrum and first-difference spectra, but fails to describe coherence in a crucial frequency band (near $\bar{N}$). Nevertheless, the model of horizontal current as a passive fine-structure field advected by internal waves is successful in a crude way. Clearly, first-difference shear spectra would have the same form as horizontal current spectra in a model of internal waves without fine-structure. The model predicts that the first-difference approximation to shear is dominated by fine-structure effects in the frequency (separation) range considered here, a prediction verified by the measured horizontal current vertical difference spectra.

Chapter 5. Wave Breaking

Previous sections have dealt with fine-structure as a passive vertical field and this approach has been fruitful in describing spectral quantities. Surely, though, finestructure is not completely passive; it is probably produced and destroyed at least on time scales long compared to internal wave periods or even on time scales as short as the buoyancy period. What produces fine-structure and what causes it to change? As the introduction mentions, internal waves have long been a prime candidate as the cause of finestructure formation and modification. The hypothesis is that waves break, mixing water in some local region around the breaking. Subsequent gravitational slump of the mixed water into the background stratification changes the temperature and salinity profile. Molecular diffusion and other processes (e.g., interfacial wave breaking, double diffusive instability, etc.) may further modify a newly formed layer. Additionally, the new profile may be complicated by incomplete mixing by wave breaking in the first place. The intent here is not to delineate the process of fine-structure modification by breaking waves, for undoubtedly it changes from event to event. Rather, the intent is to show that internal waves do break, to discuss what mechanisms may cause them to break, and to suggest that the existence of fine-structure strongly influences breaking. These ideas have been discussed before, but what distinguishes the present discussion from earlier more speculative ones is that measurements have been made with the MSA to substantiate the ideas.

Measurements of temperature along the forward mast with current data from meters at the top and bottom of the mast suggest breaking. A

six hour portion of temperature records is contoured versus position on the forward mast from the second MSA experiment in Figure 5.1a. Contours are drawn every 0.02°C (roughly ten times the least count) based upon linear interpolation over 2-minute averages (i.e., 3 estimates) of temperature at each of seven thermistors on the mast. Time marks are at 10 minute intervals. Isotherms rising and falling at steep angles with respect to the horizontal (time) axis generally indicate vertical motion. (Horizontal gradients are taken as small and ignored in this rough interpretation.) Closely (widely) spaced isotherms in the vertical indicate relatively strong (weak) temperature gradients. Note the presence of relatively well mixed regions bounded by high gradient regions. One rather striking feature of this figure is that the vertical separation of two isotherms may undergo considerable change in a rather short time (e.g., the 15.92°C and 15.94°C isotherms between 42.40 and 44.40 hours). Occasionally, closed contours of temperature or contours that indicate warm water underlying colder water (e.g., at 39.07 hrs) appear. It is possible that these brief inversions indicate gravitational instability, but irregularities in the T-S relation (discussed in an earlier section) make this interpretation shaky. Without contemporaneous salinity measurements, density inversions cannot be inferred from temperature inversions. A. J. Williams III of W.H.O.I. measured several temperature inversions that were stable in density of up to about 5 m thickness using a free-falling microstructure probe near Bermuda in conjunction with the experiment of N. Hogg and T. Sanford referred to in earlier chapters (Williams 1976, private communication). Another temperature map in

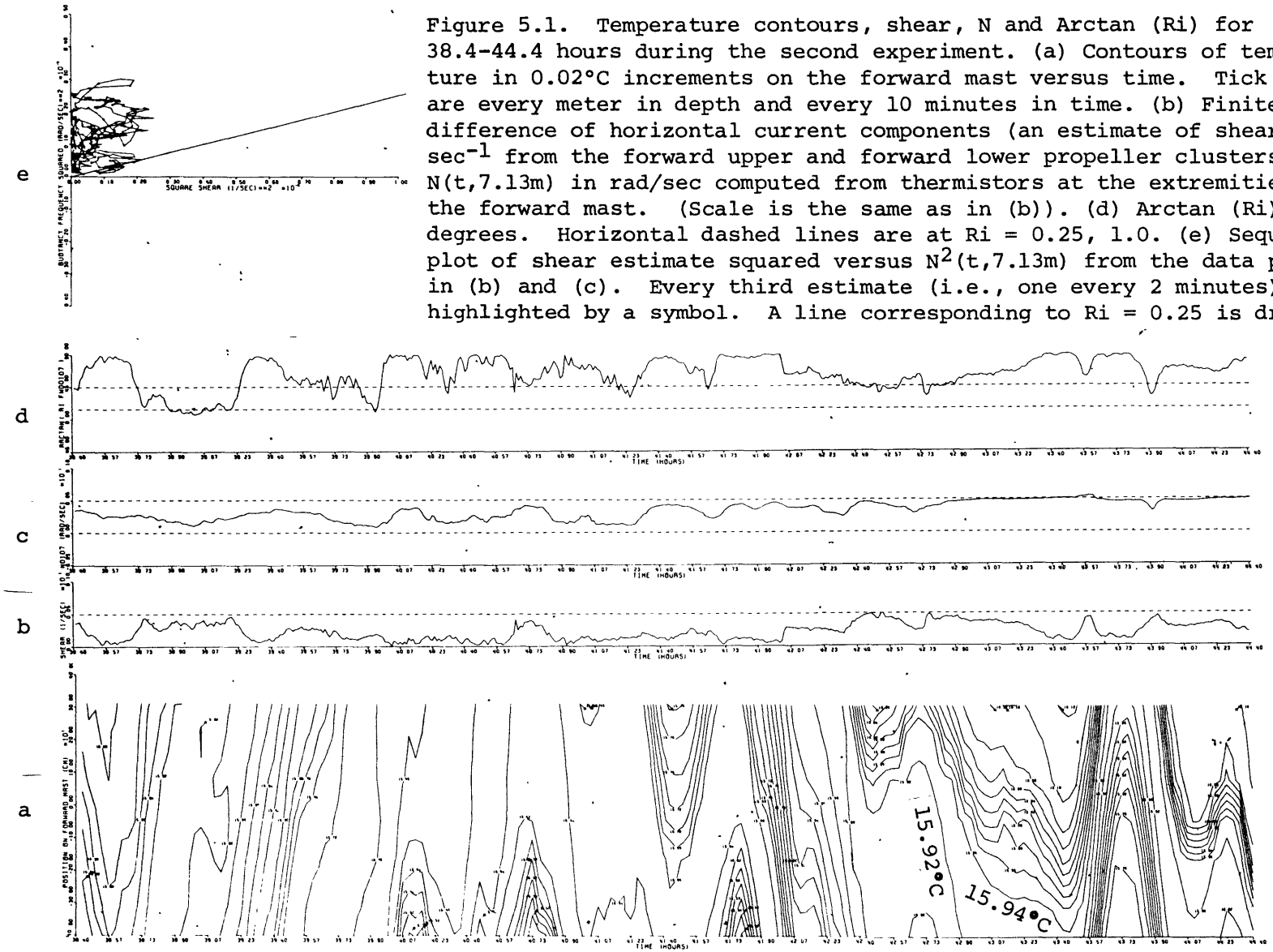


Figure 5.1. Temperature contours, shear, N and Arctan (Ri) for 38.4-44.4 hours during the second experiment. (a) Contours of temperature in 0.02°C increments on the forward mast versus time. Tick marks are every meter in depth and every 10 minutes in time. (b) Finite-difference of horizontal current components (an estimate of shear) in sec^{-1} from the forward upper and forward lower propeller clusters. (c) N(t,7.13m) in rad/sec computed from thermistors at the extremities of the forward mast. (Scale is the same as in (b)). (d) Arctan (Ri) in degrees. Horizontal dashed lines are at Ri = 0.25, 1.0. (e) Sequential plot of shear estimate squared versus N^2(t,7.13m) from the data plotted in (b) and (c). Every third estimate (i.e., one every 2 minutes) is highlighted by a symbol. A line corresponding to Ri = 0.25 is drawn.

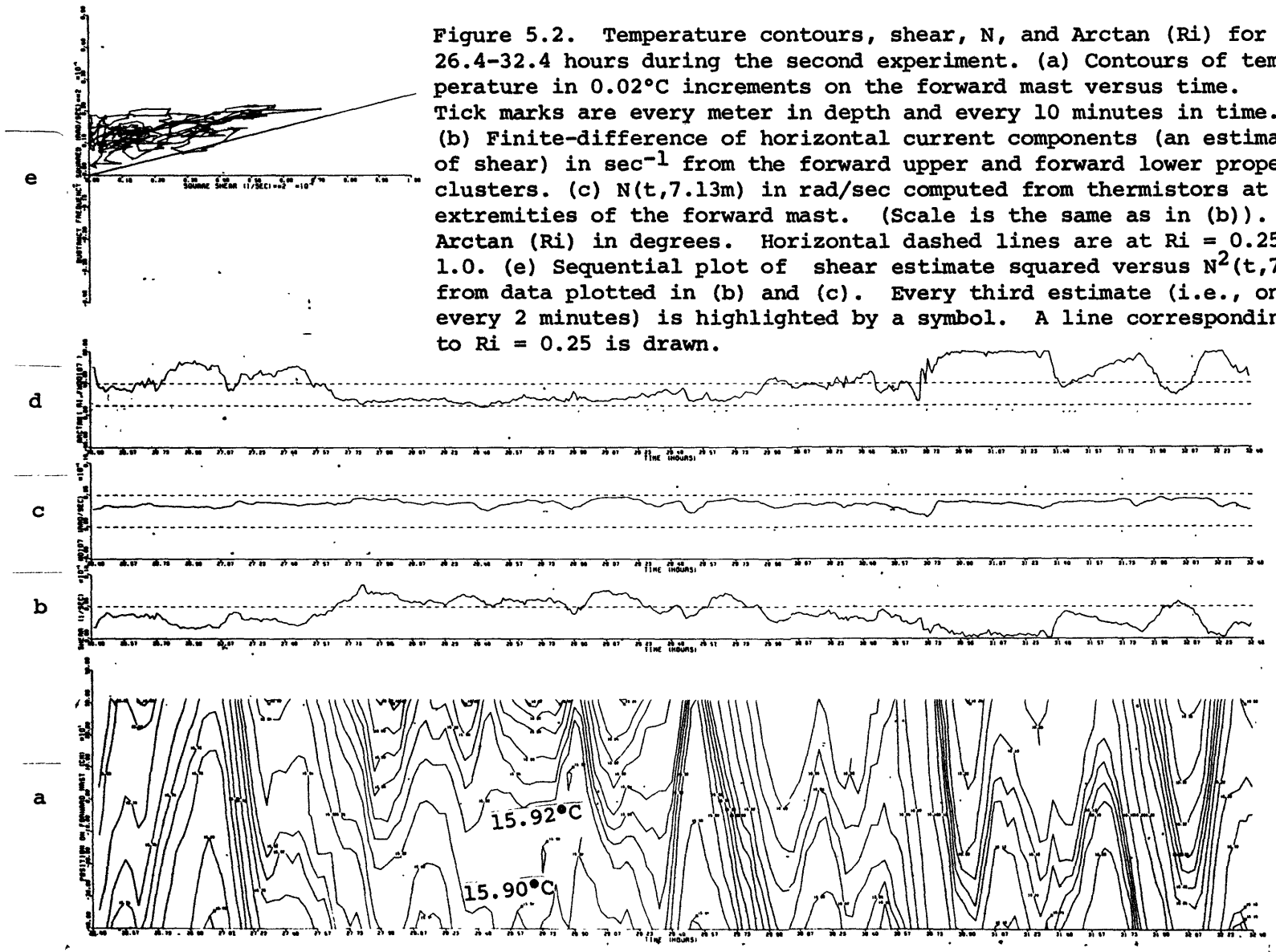


Figure 5.2. Temperature contours, shear, N, and Arctan (Ri) for 26.4-32.4 hours during the second experiment. (a) Contours of temperature in 0.02°C increments on the forward mast versus time. Tick marks are every meter in depth and every 10 minutes in time. (b) Finite-difference of horizontal current components (an estimate of shear) in sec^{-1} from the forward upper and forward lower propeller clusters. (c) N(t,7.13m) in rad/sec computed from thermistors at the extremities of the forward mast. (Scale is the same as in (b)). (d) Arctan (Ri) in degrees. Horizontal dashed lines are at Ri = 0.25, 1.0. (e) Sequential plot of shear estimate squared versus N^2(t,7.13m) from data plotted in (b) and (c). Every third estimate (i.e., one every 2 minutes) is highlighted by a symbol. A line corresponding to Ri = 0.25 is drawn.

depth versus time is given in Figure 5.2a for an earlier six hour segment. Note that low and high gradient regions are harder to delineate in this segment; one may choose to identify sheets and layers in Figure 5.1a, but the task is more difficult in Figure 5.2a. Note the substantial widening of the 15.90°C and 15.92°C isotherms from about 27.73 hours to 28.73 hours, the existence of closed contours at 28.73 and 28.90 hours, and the subsequent narrowing of the gap between them. This sequence may be indicative of mixing or it may be the passage of a salinity compensated temperature inversion (horizontal currents imply a horizontal scale of 200-400 m in the latter interpretation). These two figures clearly suggest temperature time-structure is a random phenomenon, thus confirming the need for its spectral description for the purposes of determining fine-structure effects on moored instruments.

If the sequence of isotherm separation changes described above is a mixing event, shear will be involved in the process. Whether shear causes mixing or is caused by it or both is difficult to discern, but it is hard to imagine breaking without accompanying shear on some scale. Records of shear estimated from the first difference of horizontal current components from the forward upper and lower current meters are shown in Figures 5.1b and 5.2b. Buoyancy frequency estimated over nearly same vertical separation (6.3 m for the current meters, 7.1 m for the thermistors) in the same units (sec^{-1}) and to the same scale as shear is given in Figures 5.1c and 5.2c. In addition, the angle ϕ whose tangent is $N^2/|u_z|^2$ is plotted in Figures 5.1d and 5.2d. The horizontal dashed lines in these plots correspond to $N^2/|u_z|^2 = 0.25$ and 1.0. Figures 5.1e and 5.2e are sequential displays of N^2

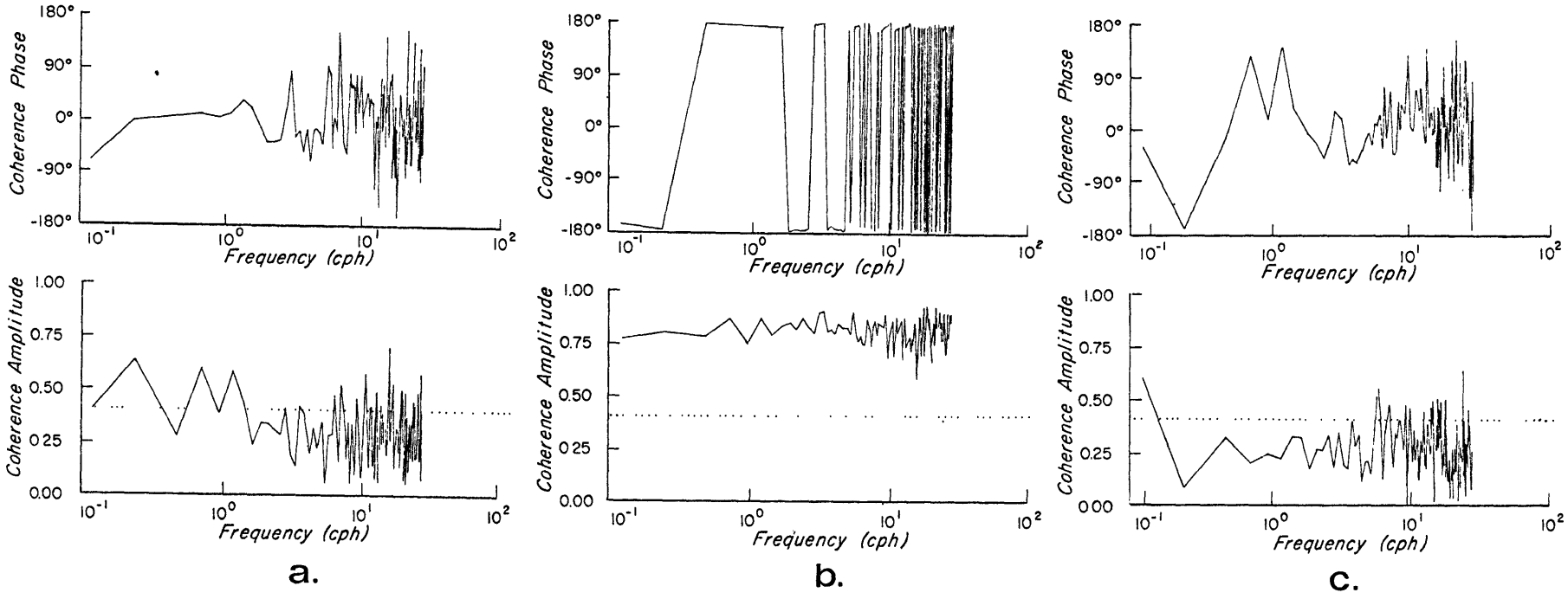


Figure 5.3. Coherence amplitude and phase of (a) N and Arctan (Ri), (b) shear and Arctan (Ri), and (c) N and shear. All are computed from a 3-day segment of the second experiment. Averages are over 18 adjacent frequencies; estimates of the level of significantly non-zero coherence with 95% confidence are drawn as dotted lines.

versus $|u_z|^2$ using data from the six hour segments plotted in the accompanying figures. Data points are 40 seconds apart and are connected by line segments in these figures with every third point highlighted by a symbol. The finite difference approximation to $N^2/|u_z|^2$ is, of course, a Richardson number Ri (see Turner (1973), p. 12). The arctangent of Ri has been chosen for display since Ri changes over a large range and may take on negative values ($N^2 < 0$). Along any line through the origin in the $N^2 - |u_z|^2$ plane (Figures 5.1e and 5.2e), ϕ and Ri are constants. In particular, the line corresponding to Ri = 0.25 has been drawn in these figures.

In both Figures 5.1 and 5.2, shear is relatively high (about $5 \times 10^{-3} sec^{-1}$ or more) when temperature inversions appear. More significantly, Ri $\simeq$ 1/4 during these events. Although the weakest stratification in Figure 5.2a is stronger than that in Figure 5.1a, shear in this six hour segment is generally higher as well, resulting in Ri < 1.0 for over two hours in this record (see Figure 5.2d), whereas Ri < 1.0 only half an hour in the later segment (see Figure 5.1d). The sequential plots in the $N^2 - |u_z|^2$ plane give the impression that fluctuations in Ri are largely due to fluctuations in shear, rather than fluctuations in buoyancy frequency. This impression is reinforced by comparison of the coherence plots of N and Ri with $|u_z|$ and Ri (Figures 5.3a and b). Buoyancy frequency and Ri are coherent at a low level (0.5 or so at low frequencies) whereas $|u_z|$ and Ri are highly coherent in this range (calculated coherences >0.75). As expected, fluctuations in $|u_z|$ and Ri are 180° out of phase. Fluctuations of N and $|u_z|$ are rather incoherent, as shown in Figure 5.3c.

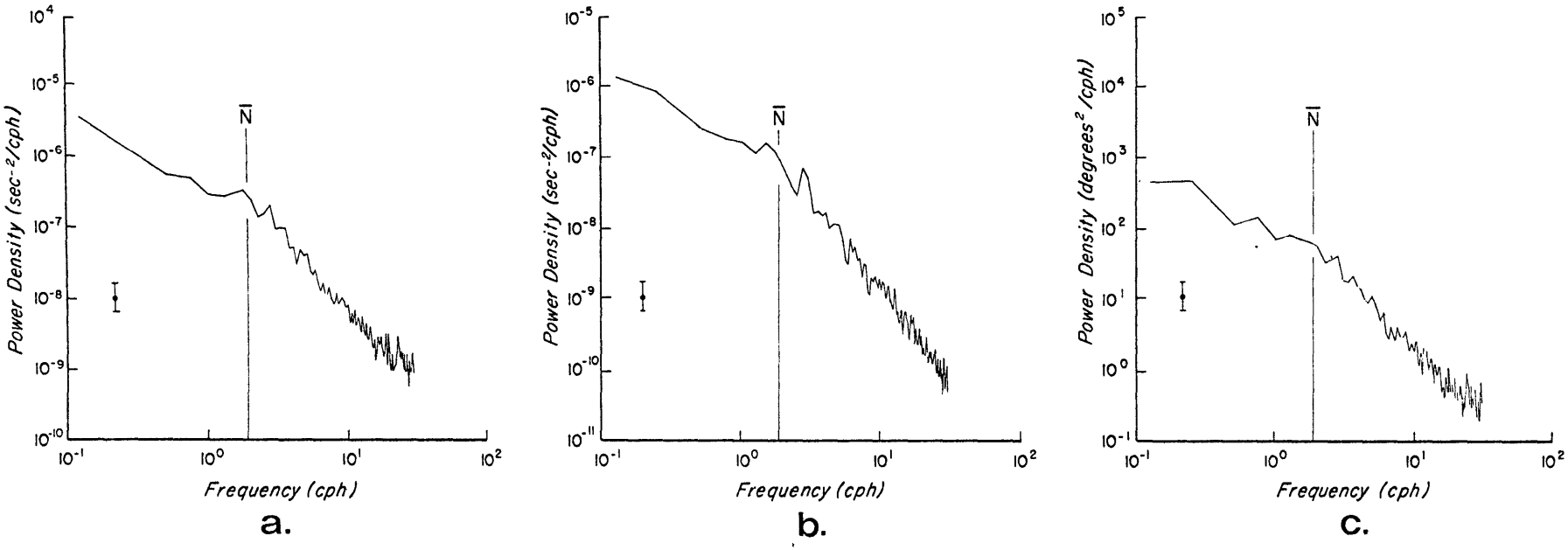


Figure 5.4. Spectra of (a) shear over 6.3 m, (b) N (7.13 m) and (c) Arctan (Ri) using the same records as in Figure 5.3. Error estimates for 95% confidence are at the left.

The variance in moored measurements of Ri is a fine-structure effect. This can be seen in Figures 5.4a,b, and c: spectra of first-difference shear, first-difference temperature converted to buoyancy frequency, and ϕ = arctan(Ri). The spectrum of shear was shown to be dominated by fine-structure contribution in the previous section. Earlier, temperature difference was also shown to be dominated by fine-structure effects, thus our estimate of N must be as well. The spectrum of the arctangent of the ratio $N^2/|u_z|^2$ may be thought of as the spectrum of fluctuations perpendicular to lines of constant Ri in the $N^2 - |u_z|^2$ plane. Energy density in fluctuations of ϕ (Figure 5.4c) varies roughly as ω^{-1} in the internal wave range. A variance preserving plot would show equal variance in any frequency band in this range. In other words, fluctuations of angle ϕ in the $N^2 - |u_z|^2$ plane are white in the internal wave range; there is no frequency preference of variance in ϕ in this range. This variance is due to fine-structure contributions to the moored measurements.

Finally, the existence of a cutoff at Ri = 0.25 is established in Figure 5.5. The line at Ri = 0.25 is not arbitrarily drawn; a histogram of ϕ for the 78 hours of data used to draw Figure 5.5 is given in Figure 5.6. The histogram shows an almost flat distribution down to $\phi \simeq 14°$; note arctan(0.25) = 14.1°. Only about 2.5% of the measurements are below Ri = 0.25, but an indeterminable fraction of these may be due to errors in calculating N because of irregularities in the T-S relation.

The existence of a limit in Ri measured over roughly 7 m and coincidence of high shear contributing to low Ri with temperature inversions suggest that these events are mixing events rather than 200-400 m

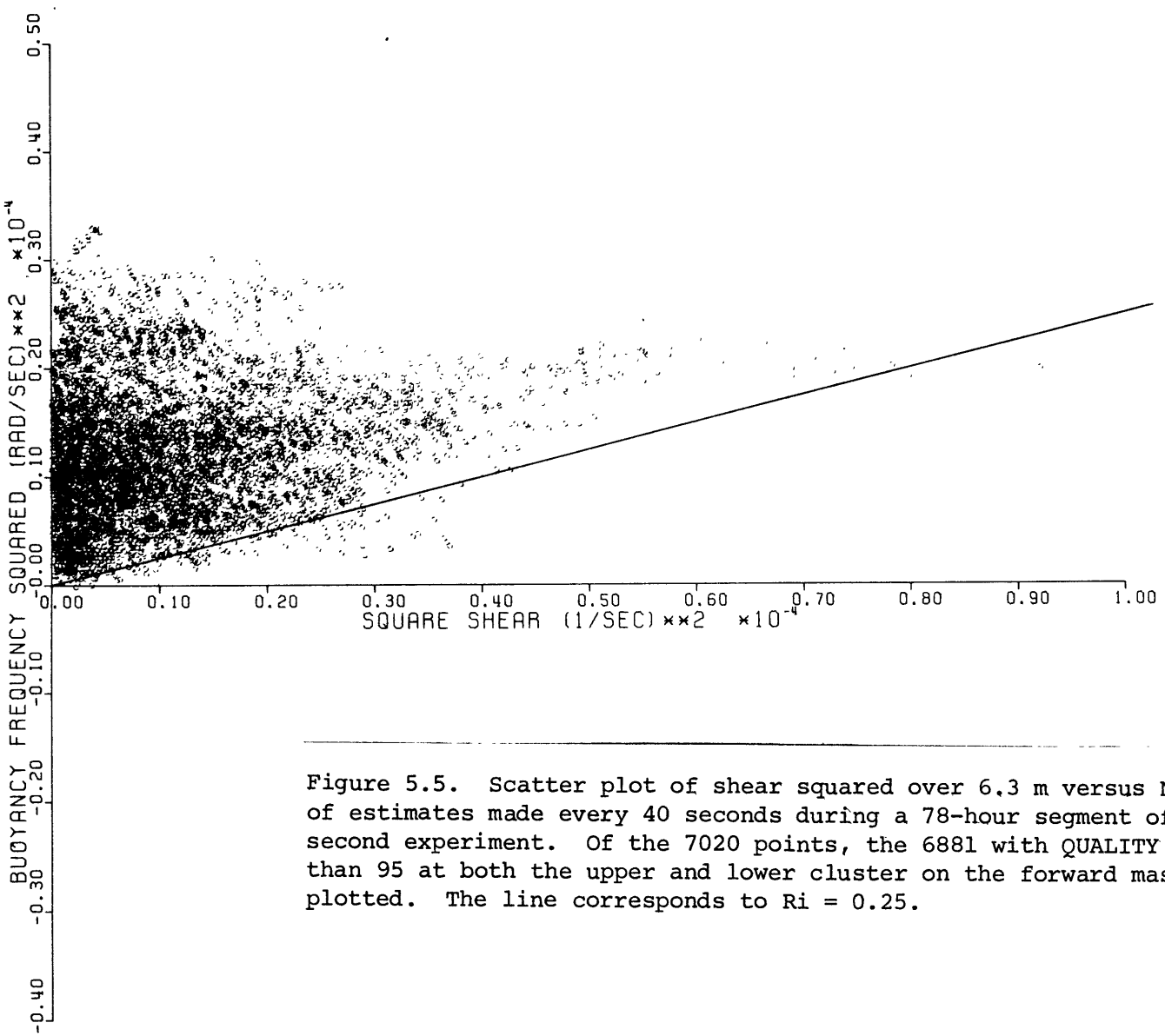


Figure 5.5. Scatter plot of shear squared over 6.3 m versus N^2(7.13m) of estimates made every 40 seconds during a 78-hour segment of the second experiment. Of the 7020 points, the 6881 with QUALITY higher than 95 at both the upper and lower cluster on the forward mast are plotted. The line corresponds to Ri = 0.25.

Figure 5.6 A histogram of Arctan (Ri) using the points plotted in Figure 5.5

Bin No.	Bound (Degrees)	Frequency	Percent Frequency	
0	-90			
1	-86	0	0.0	
2	-82	0	0.0	
3	-78	0	0.0	
4	-74	0	0.0	
5	-70	0	0.0	
6	-66	0	0.0	
7	-62	0	0.0	
8	-58	0	0.0	
9	-54	0	0.0	
10	-50	0	0.0	
11	-46	0	0.0	
12	-42	0	0.0	
13	-38	0	0.0	
14	-34	0	0.0	
15	-30	0	0.0	
16	-26	0	0.0	
17	-22	0	0.0	
18	-18	0	0.0	
19	-14	0	0.0	
20	-10	0	0.0	
21	-6	0	0.0	
22	-2	1	0.01	
23	2	2	0.03	
24	6	5	0.07	
25	10	30	0.44	
26	14	64	0.93	X
27	18	186	2.70	XXX
28	22	313	4.55	XXXXX
29	26	346	5.03	XXXXX
30	30	372	5.41	XXXXX
31	34	366	5.32	XXXXX
32	38	368	5.35	XXXXX
33	42	350	5.49	XXXXX
34	46	337	4.90	XXXXX
35	50	338	4.91	XXXXX
36	54	363	5.28	XXXXX
37	58	358	5.20	XXXXX
38	62	384	5.58	XXXXXX
39	66	354	5.14	XXXXX
40	70	375	5.45	XXXXX
41	74	346	5.03	XXXXX
42	78	344	5.00	XXXXX
43	82	416	6.05	XXXXXX
44	86	433	6.29	XXXXXX
45	90	430	6.25	XXXXXX

long parcels of water with anomalous T-S characteristics. Because mixing is intermittent and because shear and buoyancy frequency fluctuations, attributable to internal wave motions in a density profile with fine-structure have variance sufficient for Ri to reach the observed limit, wave breaking is suggested by the MSA measurements. A number of mechanisms have been proposed to explain wave breaking. Most often mentioned are the convective instability proposed by Orlanski and Bryan (1969) and the Kelvin-Helmholtz instability reviewed by Thorpe (1973). More recently McIntyre (1970) proposed a double diffusive angular momentum-density instability and McEwan and Robinson (1975) described what they call a parametric instability. The McIntyre instability is characterized by rolls whose axes are parallel to the direction of the applied shear and is able to occur at Richardson numbers as high as 100. Velocity perturbations consistent with this flow pattern are not found in the MSA data and motions show no signs of mixing (e.g., temperature inversions) for Richardson numbers greater than about 0.25. McEwan and Robinson describe their parametric instability as a precursor to breaking characterized by static instability, noting that fine-scale distortions appear well before isopycnic slopes become vertical in McEwan's (1973) experiments. They suggest that the deep ocean internal wave field provides the horizontal accelerations upon which unstable modes of half the wave frequency may grow. They believe that the ultimate mechanism for breaking to be shear or convective instabilities. Thus only Orlanski and Bryan's (1969) convective instability and the Kelvin-Helmholtz shear instability will be discussed further in connection with the MSA measurements.

Orlanski and Bryan (1969) demonstrated that internal waves are unstable (will undergo incipient breaking) whenever particle velocities locally exceed the phase velocity of the waves. The details of breaking beyond the initial stage were not considered, since the process is nonlinear (nonlinearity is the criterion for instability) and presumably rather complex. They performed a numerical experiment to demonstrate that waves would break according to their criterion. For a monochromatic field they showed that breaking would occur for Richardson numbers less than $N^2/(N^2-\omega^2)$. To test the mixing events found in the MSA data for convective instability, phase speeds must be evaluated. Use of coherence phases is inappropriate because of problems discussed earlier concerning time-averaged isotropy of the wave field. An "event analysis" was adopted instead: during a breaking event the time lag of a temperature feature's passage from forward to aft mast was estimated. Use of this rather subjective method indicated that phase velocities might be comparable to particle velocities during selected events, but to make a more quantitative estimate could be misleading. The mixing events may be due to convective instability, but the data neither confirm nor deny the possiblity convincingly.

The Kelvin-Helmholtz shear instability has been extensively studied. Thorpe (1973) reviews laboratory experiments, Miles and Howard (1964) compute growth rates from linear theory, Browning (1971) and others report observations in the atmosphere, and Woods (1968) reports observations in the seasonal thermocline. Direct observations have yet to be made in the deep ocean. Theoretical work and laboratory experiments have largely been limited to consideration of steady,

stratified shear flows. Unstable waves grow in these flows when the layer Richardson number is less than 0.25. The unstable waves grow into billows, the billows collapse causing turbulent mixing, and the turbulence gradually decays. The characteristic features of the instability are: 1) several regularly spaced billows growing simultaneously; 2) a "most unstable disturbance" wavelength 7.5 times the thickness of the shear layer; and 3) vertical motions roughly one third the magnitude of the characteristic horizontal current. Growth rates in Thorpe's experiments (Thorpe (1971, 1973)) verify those of the linear theory of Miles and Howard. The MSA data do not show a train of billows; the mixing events appear in solitude. Since no train of billows is seen, wavelength information is lacking. Typical vertical currents are roughly one-third horizontal current difference strengths. Computing growth rates according to Miles and Howard (1964) with generously estimated MSA flow strengths (shear = 10^{-2}sec^{-1}) yields time constants of exponential growth of an hour or more for Ri = 0.0, or roughly four times longer for Ri = 0.20. The MSA data cannot clearly be interpreted as showing Kelvin-Helmholtz shear instability events. Yet the instability may occur at a smaller vertical scale. Billows smaller than roughly 1.0 m would go undetected because of limited spatial and temporal resolution of the thermistor array. If billows were 1 m high, expected spacing would be 7.5 m; with 10 cm/sec currents, only two measurements of temperature would be made during passage of such a billow. Since a limit of Ri = 0.25 exists over roughly 7 m, inversions are occasionally seen, and shear fluctuations appear to overwhelmingly determine Ri fluctuations over this separation, it seems plausible to speculate that a shear

instability occurs on a smaller vertical scale smaller than 7 m, perhaps by as much as an order of magnitude.

Although the MSA measurements suggest wave breaking, none of the models discussed above unambiguously describes the mixing events. Both the Orlanski and Bryan convective instability and the Kelvin-Helmholtz shear instability are strong possibilities, but the data do not support one over the other as the mixing mechanism. Furthermore, the vertical mixing rate of wave breaking remains an elusive quantity.

Chapter 6. Conclusions

Our work has been directed toward understanding the distinction between internal waves and fine-structure in the deep ocean; the distinction is facilitated by the wavenumber shape of the internal wave spectrum. Internal waves have specific relations among flow variables; moored spectra of these variables depend intimately on both large and small scale features of stratification. The most energetic waves dynamically depend principally on large scale features, but the fine-scale features affect frequency spectra kinematically. The kinematic effects tend to dominate vertical first-difference spectra of temperature (density) and horizontal current and thus they also dominate internal wave produced variance in stratified shear stability (the Richardson number).

We developed a model of internal waves in Chapter 3 designed to describe measurements of waves at frequencies near the buoyancy frequency. Previous models, notably those of Garrett and Munk (1972a, 1975), ignored the possibility of waves trapped in the main thermocline. The proposed model of Chapter 3 sought the form of internal wave modes determined by the shape of the large scale buoyancy frequency profile. The wave functions are those expected in the smoothly varying buoyancy frequency profile of a fine-structure free main thermocline. These solutions would be of little help in describing moored measurements if vertically small scale waves were comparably energetic to vertically long ones, because short waves would both distort quasi-static features of fine-structure and be partially reflected by them. If this were the case, fine-structure would appear

to vary strongly on internal wave time scales, thus making distinction between features in stratification and waves very difficult. What simplifies the problem enormously is that low modes dominate the wavenumber spectrum. That our simple two turning-point internal wave model based on a smooth buoyancy frequency profile is a valid approximation is experimentally verified in the spectral comparisons of Chapter 3. Of the three flow variables measured, two (temperature and horizontal current) are affected by the presence of fine-structure. Vertical current is little affected as long as low modes contribute most heavily to the measured frequency spectra. Comparisons of model and observed spectra indicate that: 1) a modal description of waves trapped in the thermocline adequately accounts for the observed variance (thus no significant vertical propagation is inferred); 2) significant internal wave energy exists in evanescent waves, i.e., waves at frequencies a bit higher than the local buoyancy frequency; and 3) ratios of potential energy to horizontal kinetic energy remain nearly flat in the high frequency range, rather than rising significantly near N(z) as previous models predicted. These results follow from using an internal wave specturm that is strongly red (proportional to (wavenumber)$^{-2}$). Our observations are consistent with a time-averaged horizontally isotropic wave field. The model result that the first half-dozen or so modes determine the shape of frequency spectra is crucial to being able to distinguish between mean gradient internal waves and fine-structure.

Since only low modes contribute to the displacement field significantly, fluctuations of fine-structure at internal wave periods appear

small. Contribution to vertical wavenumber spectra of fine-structure from wave strain appears small, at most a few percent. This makes it possible to describe fine-structure as a passive vertical field even though fine-structure may in part be fine-scale internal waves. Garrett and Munk (1971), McKean (1974), and Joyce and Desaubies (1976) all made this approximation, but restricted themselves to sheet-layer models of this vertical field. Furthermore, none used internal wave model spectra that described the shape of the internal wave cut-off near N(z). Our model generalizes the description of the fine-structure as a field specified by its vertical wavenumber spectrum. Using the approach of McKean together with a more sophisticated internal wave model and a more general fine-structure model description, we were able to describe moored temperature spectra. Besides temperature spectra, model spectra of vertical temperature difference and vertical temperature coherence curves closely follow observations from the MSA. A clear distinction can be made in these models between the contribution to spectra from mean-gradient (large scale dynamical) effects and fine-structure (kinematical) effects at all frequencies in the wide range considered.

Because temperature fine-structure can be described as a passive field, a similar model (albeit crude) was tried for horizontal current fine-structure. Although horizontal current spectra predicted by such a model roughly follow the observed spectra, details of moored spectra of horizontal current near N(z) are not well described. However, moored spectra of vertical difference current components are well described and are dominated except at very low frequencies by the fine-structure contribution.

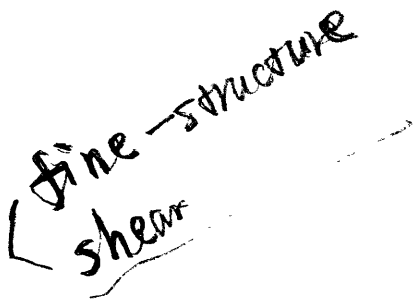
Thus moored spectra of both temperature and horizontal current contain contributions that are adequately described as kinematical results of long internal waves propagating in a medium with fine-scale variations of negligible importance to the waves.

These fine-structure contributions are significant to saturation of the wave field. Rather than small scale waves producing shear and static stability fluctuations sufficient to cause breaking, large scale waves apparently break through fine-structure contributions. That waves break is indicated from the data presented in Chapter 5; a Richardson number cutoff is strong experimental evidence of breaking and saturation of the wave spectrum. The cutoff at Ri = 0.25 (measured over 7m) is provocative. We are unable to describe the breaking process in terms of one of those postulated in the literature on stratified shear flows. We suspect breaking occurs on scales smaller than those resolvable by the MSA. Variance in Ri is produced by fine-structure effects; moreover, fluctuations of Ri are controlled mainly by fluctuations in shear. Fluctuations across lines of constant Ri in the $N^2 - |u_z|^2$ plane have equal variance in equal frequency bands in the internal wave range. The mean angle whose tangent is Ri corresponds to Ri = 1.35 and the distribution is broad enough that the cutoff angle is roughly 1.6 standard deviations below the mean. Thus breaking appears equally likely throughout the internal wave range.

Energy for modes trapped in the main thermocline may be provided by nonlinear interactions (Martin, Simmons, and Wunsch (1972)). Waves not trapped in the thermocline could be the source for the higher frequency trapped waves. Since waves dissipate through breaking, we

imagine a steady state process to maintain the internal wave spectrum at its nearly universal level.

Perhaps breaking through enhancement by fine-structure is the meaning of a saturation spectrum. Garrett and Munk (1972b) hypothesized such a scenario. This study has delineated some of the details of enhancement of shear and buoyancy frequency fluctuations by the existence of fine-structure and has demonstrated experimentally that breaking takes place. We imagine a scenario in which internal waves on an originally smooth density profile break, producing fine-structure. The presence of fine-structure (whether quasi-permanent or partially internal wave motion) kinematically enhances shear induced by vertically long internal waves, causing more breaking. Finally, fine-structure contribution to shear and N fluctuations dominates throughout the internal wave range and to higher frequencies, such that equal variance in arctan (R_i) occurs in equal frequency bands in the internal wave range. Then breaking is equally likely at any internal wave frequency. Is this saturation? To decide whether or not this scenario describes saturation of the internal wave field requires further careful observation.



Appendix. Estimation of Vertical Current from Temperature Measurements

The MSA measurements provide a unique opportunity to test the validity of conventional estimates of vertical current. Normally a simplified heat equation is used to estimate W; the equation describes a balance of time rate of change of temperature and vertical advection of temperature. It is:

$$T_t + WT_z = 0 \tag{1}$$

The neglect of horizontal advection and diffusion may be violated at small scales, where mixing may take place (see Chapter 5). The model used to calculate moored temperature spectra in Chapter 4 is based on this equation. In this section we will demonstrate that inadequate estimation of $T_z(t)$ at the same depth at which $T_t(t)$ is estimated will cause serious errors in W(t). Following modest mathematical description of the problem, several estimation schemes will be presented using MSA data.

By means of a very special illustrative model the inadequacies of estimating W(t) from a finite-difference approximation to $T_z(t)$ will be demonstrated. Imagine a constant vertical current W_o which advects a temperature field T(z). At a given level ($z = z_o$), temperature appears as a function of time T(t). Since the temperature gradient is not constant with depth, both T(t) and $T_z(t)$ will change together such that $-T_t(t)/T_z(t)$ will exactly equal W_o. In practice $T_z(t)$ is estimated as a difference over some vertical separation. A common simple scheme is to measure temperature at depths $z = z_o \pm \delta/2$

as a function of time, and divide their difference by δ. A convenient notation for this estimate is $\Delta_\delta T(t)$. If δ is very small compared to the scale of variations in $T(z)$, the estimate $W_T(t) \equiv -T_t(t)/\Delta_\delta T(t)$ will approach W_o since $\Delta_\delta T(t) \to T_z(t)$ in this limit. In the wave-number domain $\Delta_\delta T(t)$ corresponds to multiplication of $\hat{T}(k)$ (the Fourier transform of $T(z)$) by $2i \sin(k\delta/2)/\delta$. In the limit $\delta \to 0$, this factor approaches ik. Of course, multiplication of $\hat{T}(k)$ by ik corresponds to differentiation in the space domain. At all separations $\Delta_\delta T(t)$ is (in our simple model) $(W_o/\delta) \cdot (T((z+\delta/2)W_o) - T(z-\delta/2)/W_o))$. This is just $T(t)$ shifted by $\delta/2W_o$ followed by $-T(t)$ shifted by $-\delta/2W_o$, all divided by δ. In other words, the original waveform is separated out into two waveforms, one the negative of the other, both divided by δ If δ is sufficiently large and $T(z)$ has a large trend, then $\Delta_\delta T(t)$ approaches a constant, the mean gradient. At intermediate separations, the estimate of $W_T(t)$ is poor. In Fourier space, $k\delta$ is of order one so that $\sin(k\delta/2)$ has significant variation and δ is not so large as to make $2i \sin(k\delta/2)/\delta$ inconsequentially small.

Unless δ is very small, variance will appear in $W_T(t)$ even though the true vertical current W_o has none. When W_o is not a constant (as with internal wave motions), the situation is in general no better; variance in $W_T(t)$ will exceed that of $W(t)$. Temperature difference measurements over separations smaller than microstructure variation (i.e., over millimeters) are beyond the reach of present instrumentation. We are forced to estimate $T_z(t)$ over separations comparable or longer than the scales of variance in the vertical temperature profile.

Spectra of estimates of W_T made over various separations appear in Figure A.1. $T_t(t)$ is estimated from a measurement roughly midway

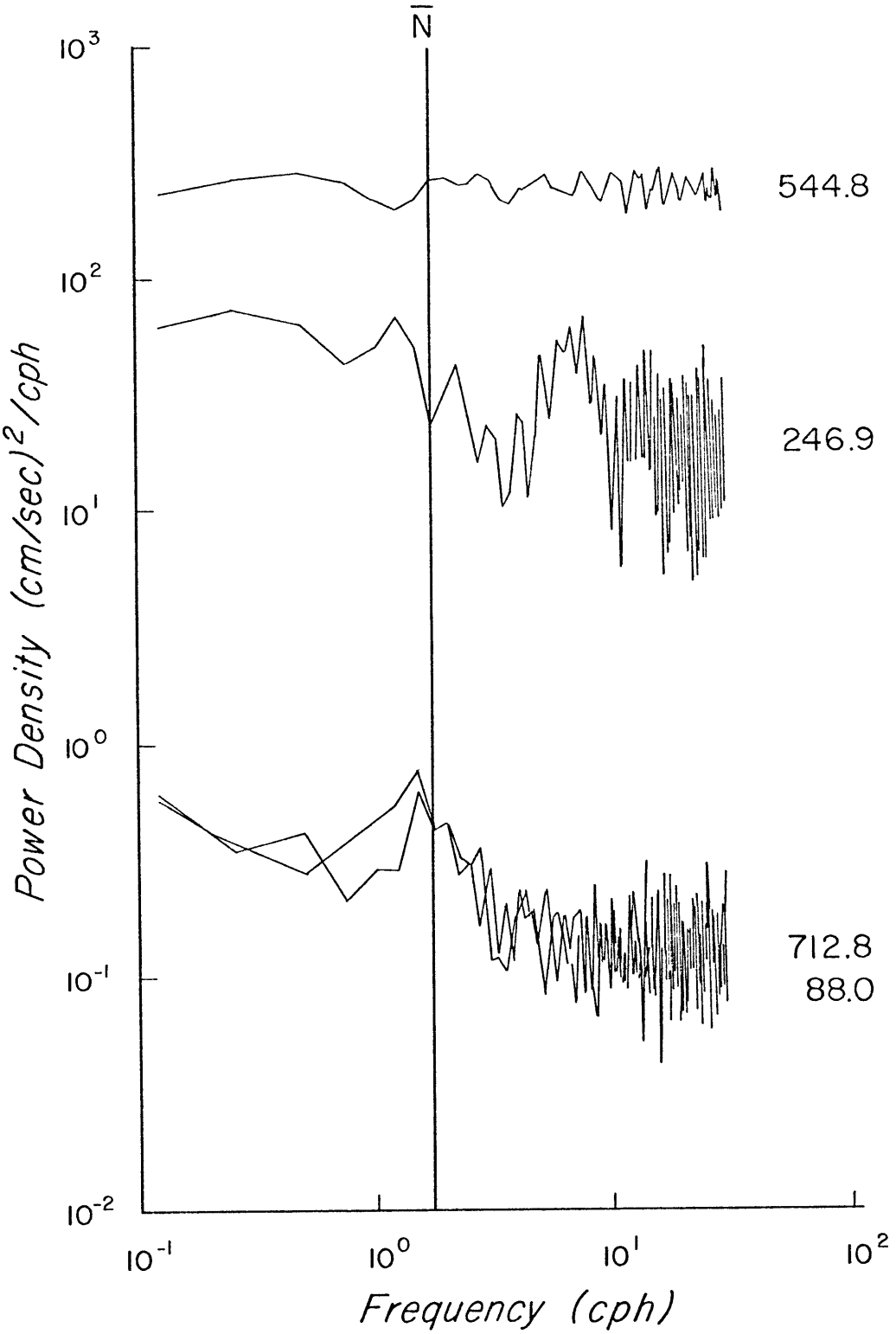


Figure A.1. Spectra of W_T estimated using finite difference approximations to T_Z over different vertical separations δ (in cm.). The spectra fail to show a cutoff at $\bar{N}$ and are more energetic than spectra of directly measured W.

between thermistors separated by δ, except for the 88 cm separation in which the upper end point thermistor was used for $T_t(t)$. The fine-structure of temperature, if interpreted as sheets and layers has a scale of about 1 m according to spectra made from vertical profiles (see Chapter 4). From the above suggestions, one expects that the best estimates of W(t) are formed at the greatest and the smallest separations δ. Indeed they are, although both estimates over 0.88 m and 7.13 m are at least a factor of two higher than the directly measured spectrum (see Figure 3.3) and neither show a cutoff at $\overline{N}$.

To compare estimates W_T with directly measured vertical current W, we take as a model

$$W(t) = a*W_T(t) + n(t) \qquad (2)$$

where n is noise, a is the factor relating W_T to W. From (2) it follows that

$$\hat{a}(\omega) = \mathrm{coh}(W,W_T)\,(P_{WW}/P_{W_TW_T})^{1/2}$$

where $P_{WW} = \langle W^*W \rangle$, $\hat{W}(\omega)$ is the Fourier transform of W, $\hat{W}^*(\omega)$ is the complex conjugate of $\hat{W}(\omega)$ and $\langle\cdot\rangle$ is an average over a band of frequencies. It is assumed that $P_{Wn} = 0$. The admittance $\hat{a}(\omega)$ is complex; if (1) were exact and the terms exactly measurable, $\hat{a}$ would have magnitude unity and phase zero. In practice the phase of $\hat{a}$ is approximately zero in the frequency range for which W and W_T are significantly coherent, but the magnitude of $\hat{a}$ is less than unity, indicating that W_T

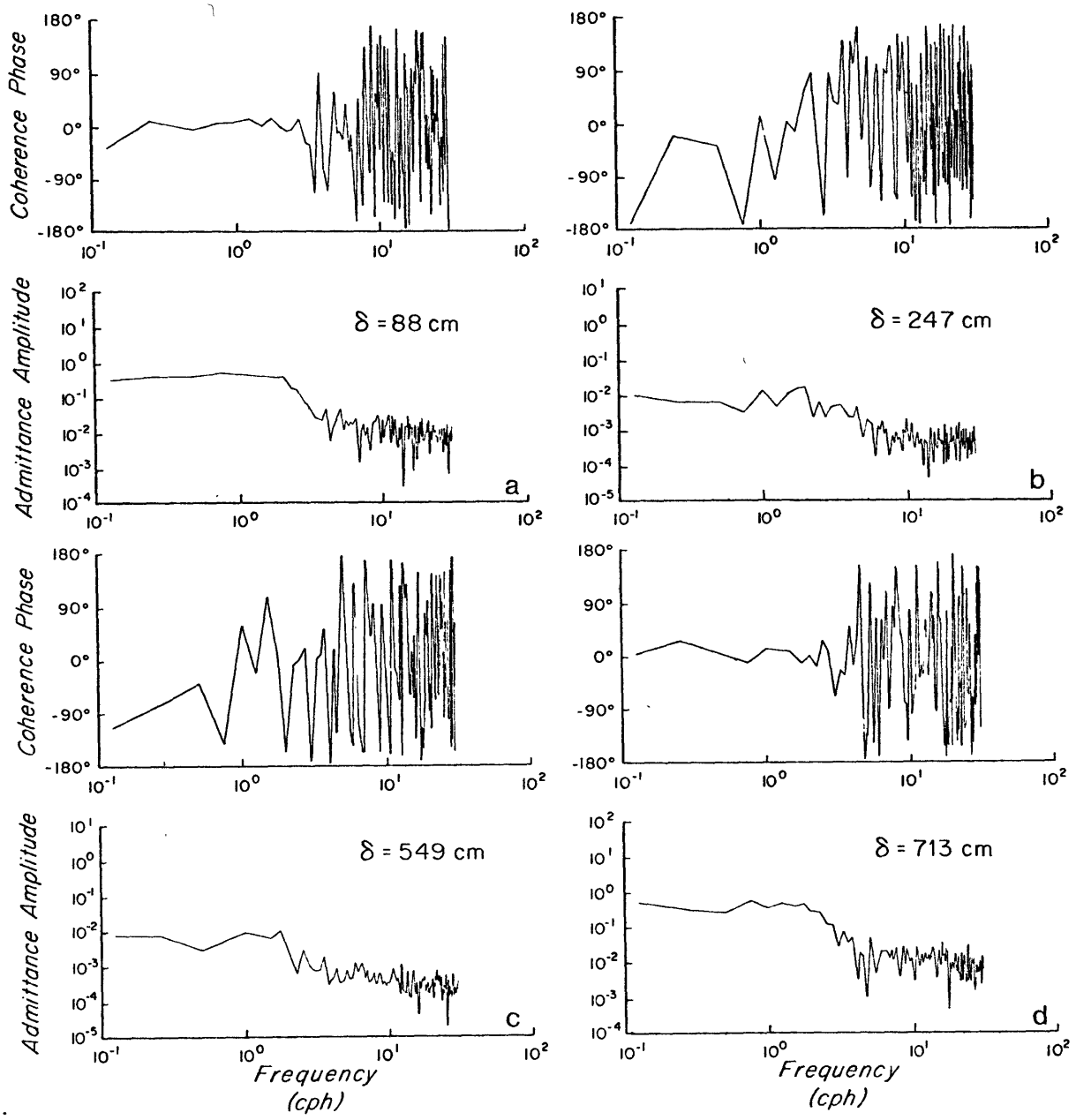


Figure A.2. Admittance amplitude and phase for the model $W = a*W_T + n$ where W_T is estimated using finite difference approximations to T_Z over different vertical separations δ. Stable phase is indicative of significantly non-zero coherence between W and W_T. Amplitudes are less than unity for all separations available; they are closest to one for the smallest (88 cm) and the largest (713 cm) separations.

consistently overestimates W (Figure A.2). Estimates of $\hat{a}$ over the largest separation and the smallest separation are closest to unity (about 0.5) in the coherent range.

Another estimate W_T can be constructed using $T_z \equiv$ constant. That is, variation in $W_T(t)$ is inferred exclusively from $T_t(t)$. A spectrum of $T_t(t)$ appears in Figure A.3a. It shows a modest cutoff above $\overline{N}$, but only vaguely resembles spectra of directly measured W (Figure 3.3). The admittance function $\hat{a}(\omega)$ from the model

$$T_t(t) = a(t)*W(t) + \hat{n}$$

appears in Figure A.3b. A horizontal line indicates the level of the admittance function if T_z were a constant. (The constant was estimated from the temperature difference over 7.13 m averaged over 78 hours.) The calculated $\hat{a}(\omega)$ has magnitude generally above the model level but differs from it by at most a factor of two in the coherent range (indicated by a phase of ±180°).

These calculations indicate that temperature inferred vertical current roughly approximates directly measured vertical current. The best estimate with the MSA data uses a model with $T_z \equiv$ constant. This estimate avoids introduction of spurious variance in $W_T(t)$ due to approximation of $T_z(t)$ by finite differencing. But $T_z(t)$ in (1) does vary for a general profile and approximating it as constant also introduces spurious variance in $W_T(t)$, although apparently not as seriously as with instantaneous evaluation of the temperature gradient. Approximation of $T_z(t)$ by more sophisticated numerical schemes (polynomial

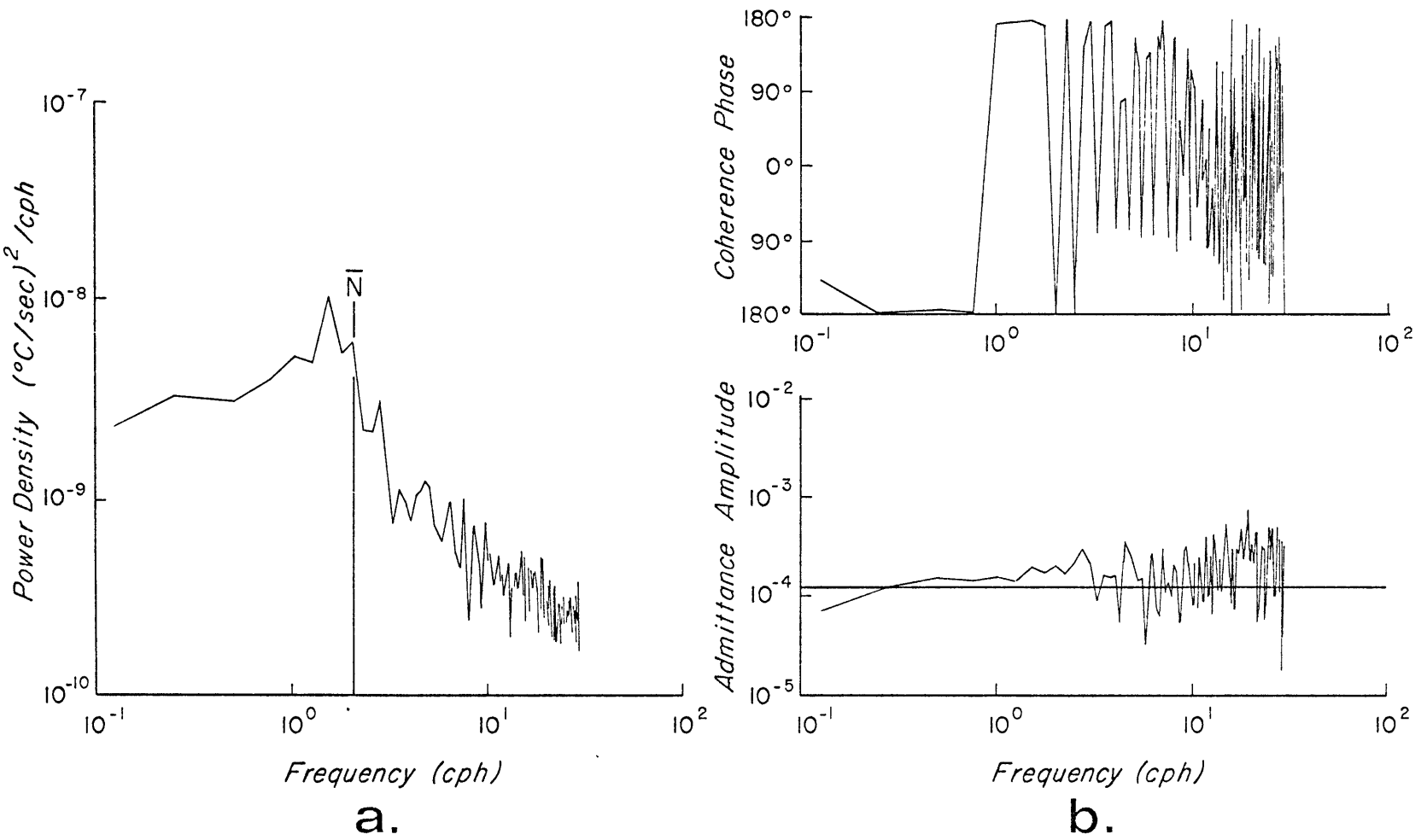


Figure A.3. (a) Spectrum of T_Z and (b) admittance of T_t with W for the model $T_t = a*W + n$. If the model were valid with constant $T_Z = 12.35 \times 10^{-3}$ °C/m, the calculated amplitude curve would fall on the horizontal line in (b).

interpolation of various kinds) does not appear likely to solve the problem when T(z) varies on fine or microscales. Cubic spline interpolation on the relatively coarse grid of thermistors was attempted with the MSA data, but results were even noisier than those using simple finite differencing. Improvement of temperature inference of vertical current may come through improvement of instrumentation so that T_z can be measured over smaller scales, but the model (1) is likely to be inadequate at small scales due to contributions from the other advective terms and dissipation in the heat equation.

References

Abramowitz, M. and I. A. Stegun (1964). Handbook of Mathematical Functions. National Bureau of Standards, Applied Mathematics Series 55, Washington, D. C.

Bell, T. H. (1973). On the scattering of internal waves by deep ocean fine-structure. J. of Phys. Oceanogr., vol. 3, no. 2, 239-241.

Briscoe, M. G. (1975). Preliminary results from the trimoored Internal Wave Experiment (IWEX). J. Geophys. Res., vol. 80, no. 27, 3872-3884.

Briscoe, M. G. (1976). Gaussianity of internal waves. Submitted to J. Geophys. Res.

Browning, K. A. (1971). Structure of the atmosphere in the vicinity of large-amplitude Kelvin-Helmholtz billows. Quart. J. R. Met. Soc. vol. 97, 283-299.

Cacchione, D. and C. Wunsch (1974). Experimental study of internal waves over a slope. J. Fluid Mech., vol. 66, part 2, 223-239.

Cairns, J. L. and G. O. Williams (1976). Internal wave observations from a midwater float, 2. J. Geophys. Res., vol. 81, no. 12, 1943-1950.

Cooper, J. W. and H. Stommel (1968). Regularly spaced steps in the main thermocline near Bermuda. J. Geophys. Res., vol. 73, 5849-5854.

Desaubies, Y. J. F. (1973). Internal waves near the turning point. Geophys. Fluid Dyn., vol. 5, 143-154.

Fofonoff, N. P. (1969). Spectral characteristics of internal waves in the ocean. Deep-Sea Res., supplement to vol. 16, 59-71.

Garrett, C. (1973). The effect of internal wave strain on vertical spectra of fine-structure. J. Phys. Oceanogr., vol. 3, 83-85.

Garrett, C. and W. Munk (1971). Internal wave spectra in the presence of fine-structure. J. Phys. Oceanogr., vol. 1, 196-202.

Garrett, C. and W. Munk (1972a). Space-time scales of internal waves. Geophys. Fluid Dyn., vol. 2, 225-264.

Garrett, C. and W. Munk (1972b). Oceanic mixing by breaking internal waves. Deep-Sea Res., vol. 19, 823-832.

Garrett, C. and W. Munk (1975). Space-time scales of internal waves: a progress report. J. Geophys. Res., vol. 80, no. 3, 291-297.

References (Contd.)

Goodman, N. R. (1957). On the joint estimation of the spectra, co-spectrum and quadrature spectrum of a two-dimensional stationary Gaussian process. Research paper no. 10 Engineering Statistics Laboratory, Research Division, College of Engineering, New York University. Also Technical report no. 8 of the David Taylor Model Basin.

Gradshteyn, I. S. and I. M. Ryzhik (1965). Table of integrals, series, and Products. Academic Press, New York.

Gregg, M. C. (1976). A comparison of finestructure spectra from the main thermocline. Submitted to J. Phys. Oceanogr.

Gregg, M. C. and C. S. Cox (1972). The vertical microstructure of temperature and salinity. Deep-Sea Res., vol. 19, 355-376.

Gröbner, W. and N. Hofreiter (1966). Integraltafel, v. 2, Springer-Verlag, New York.

Hayes, S. P., T. M. Joyce, and R. C. Millard, Jr. (1975). Measurements of vertical fine structure in the Sargasso Sea. J. Geophys. Res., vol. 80, no. 3, 314-319.

Hogg, N. G. (1972). Steady flow past an island with applications to Bermuda. Geophys. Fluid Dyn., vol. 4, 55-81.

Jenkins, G. M. and D. G. Watts (1969). Spectral analysis and its applications, Holden-Day, San Francisco.

Joyce, T. M. and Y. J. F. Desaubies (1976). Discrimination between internal waves and fine structure. Submitted to J. Phys. Oceanogr.

Lazier, J. R. N. (1973). Temporal changes in some fresh water temperature structures. J. Phys. Oceanogr., vol. 3, 226-229.

Martin, S., W. Simmons, and C. Wunsch (1972). The excitation of resonant triads by single internal waves. J. Fluid Mech., vol. 53, part 1, 17-44.

McEwan, A. D. (1973). Interactions between internal gravity waves and their traumatic effect on a continuous stratification. Boundary-Layer Met., vol. 5, 159-175.

McEwan, A. D. and R. M. Robinson (1975). Parametric instability of internal gravity waves. J. Fluid Mech., vol. 67, part 4, 667-687.

McGorman, R. E. and L. A. Mysak (1973). Internal waves in a randomly stratified fluid. Geophys. Fluid Dyn., vol. 4, 243-266.

McIntyre, M. E. (1970). Diffusive destabilization of the baroclinic circular vortex. Geophys. Fluid Dyn., vol. 1, 19-57.

References (Contd.)

McKean, R. S. (1974). Interpretation of internal wave measurements in the presence of fine-structure. J. Phys. Oceanogr., vol. 4, 200-213.

Miles, J. W. and L. N. Howard (1964). Note on a heterogeneous shear flow. J. Fluid Mech., vol. 20, part 2, 331-336.

Mysak, L. A. and M. S. Howe (1976). A kinetic theory for internal waves in a randomly stratified fluid. Dyn. Atmospheres and Oceans, vol. 1, 3-31.

Nayfeh, A. H. (1973). Perturbation Methods. Wiley and Sons, New York.

Osborn, T. R. and C. S. Cox (1972). Oceanic fine structure. Geophys. Fluid Dyn., vol. 3, 321-345.

Orlanski, I. and K. Bryan (1969). Formation of the Thermocline step structure by large-amplitude internal gravity waves. J. Geophys. Res., vol. 74, no. 28, 6975-6983.

Panicker, N. N. and D. W. Schmidt (1975). Prediction and Measurement of the stability of the IWEX tripod mooring. Woods Hole Oceanographic Institution Technical Report 75-46.

Phillips, O. M. (1966). The dynamics of the upper ocean. Cambridge University Press,Cambridge, England.

Phillips, O. M. (1971). On spectra measured in an undulating layered medium. J. Phys. Oceanogr., vol. 1, no. 1, 1-62.

Pochapsky, T. E. (1972). Internal waves and turbulence in the deep ocean. J. of Phys. Oceanogr., vol. 2, 96-103.

Sanford, T. B. (1975). Observations of the vertical structure of internal waves. J. Geophys Res., vol. 80, no. 27, 3861-3871.

Shillingford, J. T. (1976). The Microscale Sensing Array. C. S. Draper Laboratory report (in preparation).

Shillingford, J. T. and J. Dahlen (1976). Development and ocean deployment of the Microscale Sensing Array. (in preparation).

Smith, R. (1975). Second-order turning point problems in oceanography. Deep-Sea Res., vol. 22, 837-852.

Stommel, H. and K. N. Federov (1968). Small scale structure in temperature and salinity near Timor and Mindanao. Tellus, vol. 19, 306-325.

Tait, R. I. and M. R. Howe (1968). Some observations of thermo-haline stratification in the deep ocean. Deep-Sea Res., vol. 15, 275-280.

References (Contd.)

Thorpe, S. A. (1970). Experiments on the instability of stratified shear flows: miscible fluids. J. Fluid Mech., vol. 46, part 2, 299-310.

Thorpe, S. A. (1973). Turbulence in stably stratified fluids: a review of laboratory experiments. Boundary-Layer Met., vol. 5, 95-119.

Turner, J. S. (1973). Buoyancy effects in fluids. Cambridge University Press, Cambridge, England.

Voorhis, A. (1968). Measurements of vertical motion and the partition of energy in the New England slope water. Deep-Sea Res., vol. 15, 599-608.

Webster, T. F. (1972). Estimates of the coherence of ocean currents over vertical distances. Deep-Sea Res., vol. 19, 35-44.

Woods, J. D. (1968). Wave-induced shear instability in the summer thermocline. J. Fluid Mech., vol. 32, part 4, 791-800.

Wunsch, C. (1972). Temperature microstructure on the Bermuda slope with application to the mean flow. Tellus, vol. 24, no. 4, 350-367.

Wunsch, C. (1975). Deep ocean internal waves: What do we really know? J. Geophys. Res., vol. 80, no. 3, 339-343.

Wunsch, C. and J. Dahlen (1970). Preliminary results of internal wave measurements in the main thermocline at Bermuda. J. Geophys. Res., vol. 75, no. 30, 5899-5908.

Wunsch, C. and J. Dahlen (1974). A moored temperature and pressure recorder. Deep-Sea Res., vol. 21, 145-154.

Biographical Note

The author was born on October 5, 1950 in San Francisco, California. He grew up in Hillsborough, California, attending North Hillsborough School, Crocker School, and Burlingame High School. He earned an A.B. Magna Cum Laude from Harvard University in the field of Engineering and Applied Physics in June, 1972. He held summer fellowships at Woods Hole Oceanographic Institution and the National Center for Atmospheric Research in Boulder, Colorado, before entering graduate school in oceanography. Eventually he will return to the west coast to live.